AD_____

Award Number: W81XWH-04-1-0551

TITLE: Investigation of Metastatic Breast Tumor Heterogeneity and Progression Using Dual Optical/SPECT Imaging

PRINCIPAL INVESTIGATOR: Peter P. Antich, Ph.D.

CONTRACTING ORGANIZATION: University of Texas
Dallas, TX 75390-9105

REPORT DATE: May 2008

TYPE OF REPORT: Final Addendum

PREPARED FOR: U.S. Army Medical Research and Materiel Command
Fort Detrick, Maryland 21702-5012

DISTRIBUTION STATEMENT: Approved for Public Release;
Distribution Unlimited

The views, opinions and/or findings contained in this report are those of the author(s) and should not be construed as an official Department of the Army position, policy or decision unless so designated by other documentation.

REPORT DOCUMENTATION PAGE

Form Approved
OMB No. 0704-0188

Public reporting burden for this collection of information is estimated to average 1 hour per response, including the time for reviewing instructions, searching existing data sources, gathering and maintaining the data needed, and completing and reviewing this collection of information. Send comments regarding this burden estimate or any other aspect of this collection of information, including suggestions for reducing this burden to Department of Defense, Washington Headquarters Services, Directorate for Information Operations and Reports (0704-0188), 1215 Jefferson Davis Highway, Suite 1204, Arlington, VA 22202-4302. Respondents should be aware that notwithstanding any other provision of law, no person shall be subject to any penalty for failing to comply with a collection of information if it does not display a currently valid OMB control number. **PLEASE DO NOT RETURN YOUR FORM TO THE ABOVE ADDRESS.**

1. REPORT DATE *(DD-MM-YYYY)*	**2. REPORT TYPE**	**3. DATES COVERED** *(From - To)*
01-05-2008	Final Addendum	1 MAY 2007 - 30 APR 2008

4. TITLE AND SUBTITLE

Investigation of Metastatic Breast Tumor Heterogeneity and Progression Using Dual Optical/SPECT Imaging

5a. CONTRACT NUMBER

5b. GRANT NUMBER
W81XWH-04-1-0551

5c. PROGRAM ELEMENT NUMBER

6. AUTHOR(S)
Peter P. Antich, Ph.D.

E-Mail: Peter.Antich@UTSouthwestern.edu

5d. PROJECT NUMBER

5e. TASK NUMBER

5f. WORK UNIT NUMBER

7. PERFORMING ORGANIZATION NAME(S) AND ADDRESS(ES)

University of Texas
Dallas, TX 75390-9105

8. PERFORMING ORGANIZATION REPORT NUMBER

9. SPONSORING / MONITORING AGENCY NAME(S) AND ADDRESS(ES)
U.S. Army Medical Research and Materiel Command
Fort Detrick, Maryland 21702-5012

10. SPONSOR/MONITOR'S ACRONYM(S)

11. SPONSOR/MONITOR'S REPORT NUMBER(S)

12. DISTRIBUTION / AVAILABILITY STATEMENT
Approved for Public Release; Distribution Unlimited

13. SUPPLEMENTARY NOTES

14. ABSTRACT
The goal of our project was to develop methods to image the processes that occur during tumor growth and metastatic spread or regression including the fate of minimal residual disease. The key to this was through the development of a dual modality imaging system capable of performing both optical and SPECT imaging in mice. To do so it is necessary to test the limits of sensitivity of newly developed techniques: our technical goal is to develop integrated light emission and single photon emission tomography. We have made substantial progress in our techniques for the detection of metastases. We have demonstrated our capability to detect millimeter or sub-millimeter metastases in mice by light emission. To this end we have used Light Emission Tomography (LET), a technique based on bioluminescence of cancer cells transfected with luciferase, to detect metastases in the lung, bones and head. We have begun assessment of perfusion using fluorescence imaging. In addition, our technological focus is on the simultaneous use of Single-photon Emission Computed Tomography (SPECT), and to this end we have developed a new form of micro-SPECT based on cooled, electron-multiplied Charge-Coupled Devices (EMCCDs).

15. SUBJECT TERMS
SPECT, Optical Bioluminescence Imaging, Metastatic Development, Tumor Heterogeneity

16. SECURITY CLASSIFICATION OF:			**17. LIMITATION OF ABSTRACT**	**18. NUMBER OF PAGES**	**19a. NAME OF RESPONSIBLE PERSON**
a. REPORT	**b. ABSTRACT**	**c. THIS PAGE**			USAMRMC
U	U	U	UU	65	**19b. TELEPHONE NUMBER** *(include area code)*

Table of Contents

Introduction…….... 4

Body……5

Key Research Accomplishments……19

Reportable Outcomes……20

Conclusions……20

Appendices……20

INTRODUCTION

We have made substantial progress in our techniques for the detection of metastases. We have demonstrated our capability to detect millimeter or sub-millimeter metastases in mice by light emission. To this end we have used Light Emission Tomography (LET), a technique based on bioluminescence of cancer cells transfected with the luciferase gene, to detect metastases in the lung, bones and head. We have begun assessment of perfusion using fluorescence imaging. To accomplish the transition from the laboratory to the clinic, our technological focus is on the simultaneous use of Single-photon Emission Computed Tomography (SPECT). By imaging appropriate molecular sensors using SPECT, we hope to demonstrate coregistration of the SPECT with the LET signal and thus demonstrate the relationship between the Nuclear Medicine and the tumor-cell-specific signal. To this end we have developed a new form of gamma camera based on cooled, electron-multiplied Charge-Coupled Devices (EMCCDs) with which we are performing ongoing optimization. We have also collaborated on the assessment of a new, promising SPECT imaging agent, clioquinol or Iodinated hydroxyquinoline. By tagging this molecule with I-123, we will obtain SPECT images and we will use bioluminescence imaging to test if clioquinol imaging detects areas where tumor cells proliferate and establish metastases and to identify the relative times at which the images first appear.

BODY

Light Emission Tomography.

Extensive efforts were made to create and optimize computer algorithms for locating bioluminescent light sources using surface light intensity. A preliminary algorithm for point source emitters was published in Medical Physics and has been shown to quite robust, despite a lack of mathematical rigor. The LET reconstruction algorithm is summarized in the following figure:

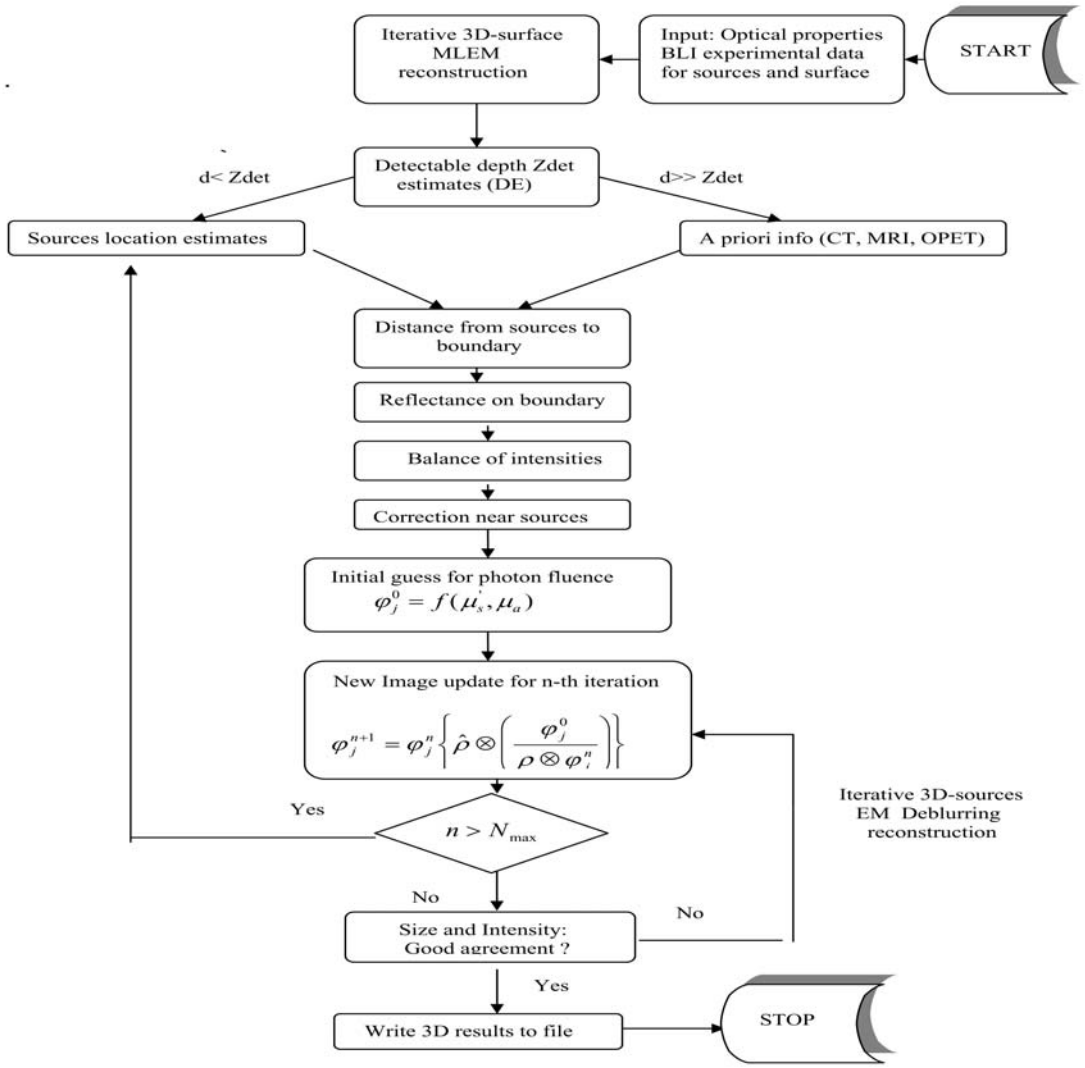

Because bioluminescence can often be quite intense, the emitted light on the surface can also illuminate the animal bed and cameras on the opposing side of the gantry. In addition, the white light image for surface topography must also be separated into foreground and background components. This presents the need to first remove this unphysical signal from the raw BLI images. Considerable effort has been completed in automating this process. An example of this improvement is shown in the following figure:

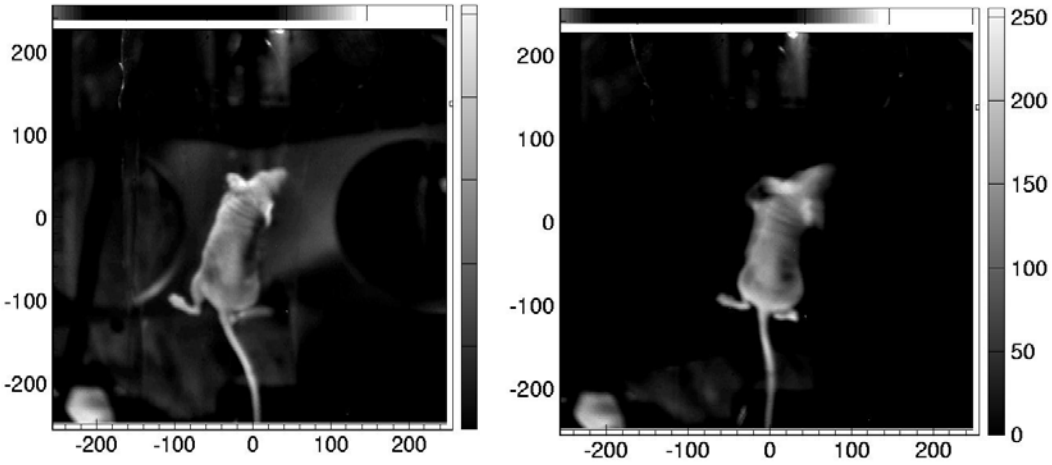

Left panel. Image obtained using both bioluminescence and external illumination. Note light signals outside the animal's body: these are absent in the right-hand panel after pre-processing.

We have tested tumors at various sites within the body to determine the circumstances under which we could reliably detect metastases. We developed means to calibrate light intensity in terms of photons/unit area/sec and to evaluate the light intensity emitted by the different cell lines used in our studies. We were able to detect in vitro with the same instrument extended distributions with 500 cells and foci estimated at 10-30 cells when the cells had sufficient emission intensities. We then undertook imaging studies of metastases. To investigate a biological model of breast cancer metastasis to the lung, 10^6 MDA MB 231-Luc cells were injected into the tail vein of a nude mouse. We performed sequential images of the animal both by LET and by MRI. Metastases were unambiguously identified 22 days post-injection as three separate nodules in the two lungs; and the two larger foci in the left lung were confirmed by MRI on day 46.

The figure shows four 1mm-thick tomographic slices, 2 for LET and 2 for MRI.
LET shows three metastases on days 22 and 43, two in the left and one in the right lung.
Using a 4.5 T small animal magnet, MRI confirms the two metastases in the left lung on day 46. In the LET images the maximum intensity of light emission increases by a factor of 3-3.5 between days 22 and 32.

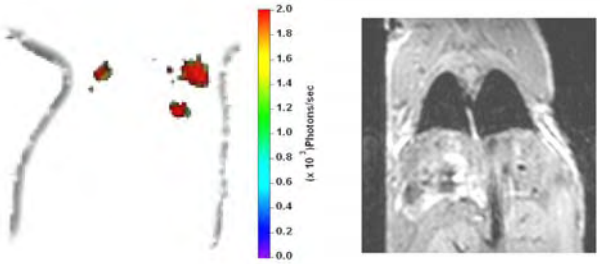

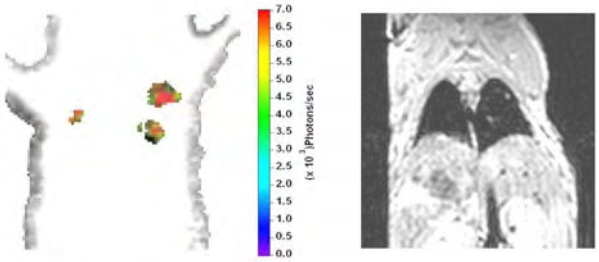

We then investigated whether or not the device could image small tumors in the cranial cavity. $8x10^3$ tumor cells were injected at two sites, within the cranial cavity of a nude mouse and in the flank, $5x10^3$ in the head of a second mouse and tumors were allowed to develop freely. The tumors grew at a slow rate and displayed similar light intensity at early times, diverging only slightly in their growth pattern. Thus, brain metastases are also detectable.

Day 0 Injected cells 8,000 Injected cells 5,000

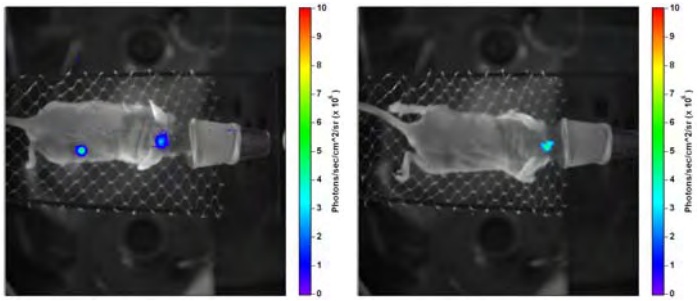

DAY 11

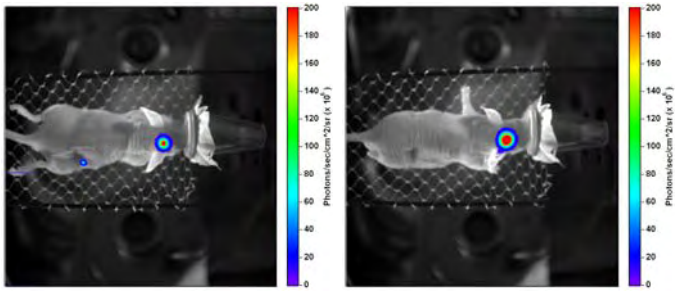

As the tumors developed between day 0 and 11, the light intensity increased 20-fold.

By way of comparison, an MRI image at 4.75 T shows the central location of the tumor in the T1 contrast image at day 10.

MDA-MB231 in brain on day10 of (8000 cells; with flank tumor)

T1-weighted

T2-weighted

T1 contrast

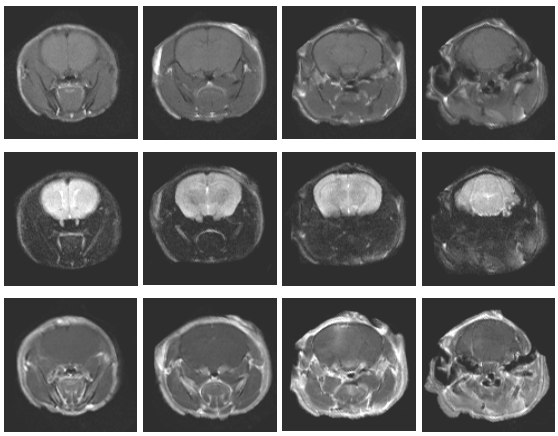

To study smaller foci and number of cells it is necessary to adopt higher magnification optics. This would require the acquisition of new optics and we are investigating avenues to do so.

LET LIMITATIONS IN THE RECONSTRUCTION OF SMALL TUMORS *IN VIVO*

All tomographic imaging modalities have limitations in terms of the required minimum signal intensities, signal to noise ratio, and the number of projections necessary to obtain good quality images. In the case of LET, when the bioluminescent signal is very low due to either small tumor volume (incipient metastases), and/or low light production efficiency of the cell line, several angular directions could yield images with no detectable signal due to intervening tissue with high absorption properties. Thus, it is important to determine the limits of LET regarding the smallest signal that produces accurate volumetric images in a realistic experimental setup, in an organ position at significant depth such as the pancreas.

Two cell lines characterized by different light emission properties were chosen to test the limits of detectability. Stably luciferase transfected MIA-LUC cell line produced 172±13 photons/s/cell, while Panc1-LUC cell line gave 62±8 photons/s/cell *in vitro*. Two BALBc/nu/nu mice were implanted in the pancreas with $2x10^3$ cells in 50 μl volume using one cell line for each animal. After SQ injection of 450 mg/kg D-luciferin the mice were imaged using 300 s exposure time with 4 cameras in 5 discrete positions for a total of 20 angular directions. We attempted tomographic reconstruction using 0.5 mm cubic voxels for each case.

LET was successful in the case of the more efficient MIA-LUC cells that produced detectable signal in 8 of the angular directions, but failed in the case of the Panc1-LUC cells where only 3 adjacent angular directions exhibited useful light emission. Since the S/N ratio in the MIA-LUC reconstruction was approx 2.5, and Panc1-LUC cells emit 2.8 times less light and were implanted using the same volume of solution, the negative result was expected for this cell line. The imaging protocol was repeated four and six days later and LET reconstruction was successful in both animals. On day 5 the MIA-LUC image showed significantly higher signal when compared to the image obtained on day 1. Thirteen angular directions presented S/N ratio larger than 1.5 in the MIA-LUC image compared to 8 angular directions in the Panc1-LUC image. The photon flux for the Panc1-LUC image on day 5 was smaller than in the case of the MIA-LUC cells imaged on day 1, and the S/N ratio was 1.5 close to the limit of practical detectability. Thus, the corresponding photon flux of $2.2x10^5$ photons/s was considered to be the lowest practical limit for concentrated light sources positioned deep inside an animal the size of a mouse. Both cell lines were imaged successfully on day 7. A graphical representation of the experimental results is shown below. The data point for Panc1-LUC cells under the imaging threshold was estimated from *in vitro* measurements on cell suspension of identical concentration and volume. The LET algorithm was able to produce accurate tomographic reconstructions when at least eight of the 20 angular directions present bioluminescent signal above the noise level

Using the average light emission efficiency of each cell line and the minimum photon flux that can be accurately reconstructed a lower limit of the number of cells that can be successfully imaged can be calculated. Accordingly, the minimum number of cells that LET is capable of imaging tomographically at depth would be about 1250 for the MIA-LUC line, while the Panc1-LUC cell line would require more than 3500 cells. The A549-LUC cells used in the lung metastasis model would require only approx. 1150 cells. It should be mentioned that this is the worst case scenario when the light emitting tumors are very small and positioned at depth, close to tissues that exhibit large light adsorption properties in particular the liver. If the tumors are in a peripheral position such as SQ or in the limbs the performance would be greatly enhanced.

Compared with planar bioluminescent imaging LET has the advantage that it acquires the light emission from 20 angular directions that effectively covers the entire surface of the

animal. Thus, LET can detect any bioluminescent signal that emits sufficient light to escape the animal body regardless of the direction. In our practical experience planar imaging can often miss small tumors positioned in unexpected locations, such as metastases, that are only visible from a small solid angle. This is especially true when a larger tumor is present and constitutes the primary target of the investigation. In the case of the Panc1-LUC cell line imaged in day 1 the tumor was successfully detected even though the volumetric reconstruction failed. Planar imaging would have had only a 15% chance of detecting the tumor with no *a priori* information regarding location, since the signal was present in only 3 angular directions from the total of 20.

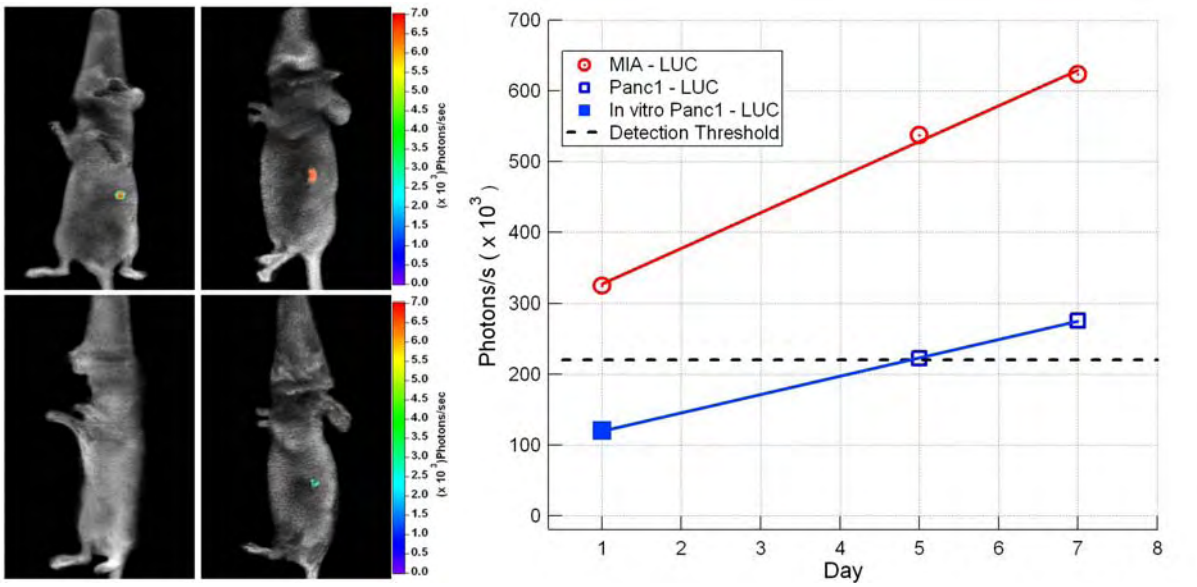

a **b**

(a) *Images of 2x10^3 Mia-LUC (right column) and Panc1-LUC cells (left) implanted in the pancreas of two BALBc/nu/nu mice at day 1 (lower row) and 5 (upper row) after implantation and* ***(b)*** *total light emission vs time. The minimum threshold for accurate tomographic reconstruction is shown by the dashed line. The first data point for the Panc1-LUC cells was obtained in vitro before implantation.*

Quantifying Tumor Volume

Since assessing the tumor size is important in cancer studies, a comparison of the ability of planar BLI and LET to quantify the size of tumors *in vivo* was performed. PC3-LUC cells injected in the flank of nude mice (BALBc/nu/nu) were imaged in the LET system using 5 s exposure time from 20 angular directions (4 cameras x 5 positions). The 0° angular view was used as a representative planar image and the total light emission was calculated and compared with the volume calculated from caliper measurements of the tumors . Volumetric images of the tumors were reconstructed using the LET algorithm and 0.5 mm cubic voxels. Each tumor volume was estimated using the volume of the voxels exhibiting bioluminescence intensity above the background and compared with the volume obtained from caliper measurements as shown below. For small tumors the planar BLI yields good correlation with the caliper measurements (Fig. 6a), but when the larger tumors are considered the

correlation becomes weaker (R^2 = 0.93 versus R^2 = 0.86). Underestimation of the volume of large tumors by planar BLI has also been reported by others [27]. The volume calculated using the volumetric LET algorithm exhibits better correlation with the caliper measurements (R^2 = 0.988) and there is no degradation of the linearity for large tumors. Moreover, the linear regression has a zero intercept and a slope close to unity (0.925) indicating equivalence of the two measurements.

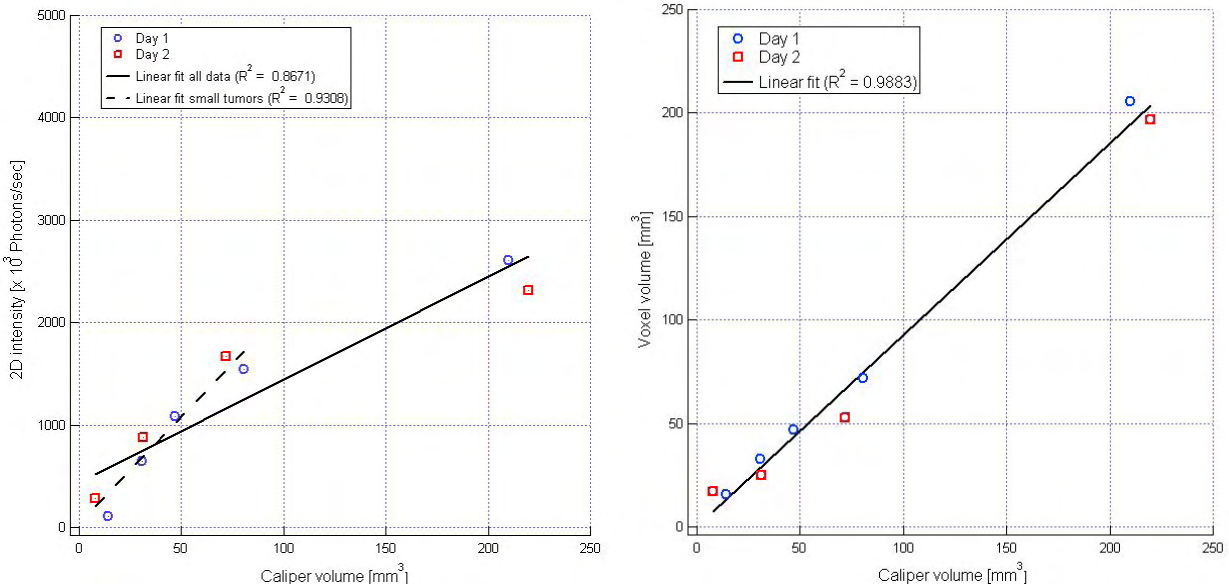

Correlation of (left panel) the planar bioluminescence and (right panel) LET reconstructed volume with caliper measurements.

Small Animal SPECT

Our project proposed to test multimodality imaging, joining LET and SPECT (Single Photon Emission Tomography). To this end we have developed a camera equipped with electron multiplying CCDs. The CCDs are coupled to scintillating crystals after passing through a collimator and detect the interactions of gamma rays with the crystal. Integrating these signals over time produces images that could potentially be used for SPECT reconstruction.

Our initial hypothesis was that the same CCD camera could be optimized for both bioluminescence and gamma ray imaging. One key conclusion of this research endeavor is that the null hypothesis is most probable. It is clear that bioluminescence imaging can always be optimized efficiently by maximizing the sensitivity of the ultimate optical detector. This is however not true for CCD-based gamma cameras. For lens-coupled CCD-based cameras, the limiting efficiency is the optical coupling. While the gamma conversion via scintillation and state-of-the-art CCD cameras have quantum efficiencies on the order of 0.9, the lens coupling efficiency is on the order of 0.001. This efficiency is also degraded by a factor that is proportional to the ratio of the FOV on the scintillating crystal to the CCD sensor area. Due to this conservation of etendue, increasing demagnification by a factor of 2 will reduce optical efficiency by a factor of 4. As we have shown, and others have also reported in the literature, it is feasible to have sufficient optical coupling to resolve individual scintillation events in photon counting mode if one uses a 1:1 optical coupling. Unfortunately, most CCD sensor has dimensions on the order of 10 mm, which is not a sufficient FOV for mouse imaging. Two possible solutions present themselves to maintain photon counting mode: use larger CCD sensors, or increase optical coupling efficiency.

If photon counting is abandoned, then the use of energy integration in ccdSPECT is complicated by two factors. First, the integration of the stochastic scintillation light leads to deceased signal to noise compared to photon counting. Fortunately for scintillators such as CsI(Tl) this effect is only on the order of 10%. Second, there is a four-fold resolution penalty for energy-integrating CCD gamma cameras. As we previously demonstrated, the intrinsic resolution of our CCD gamma camera is slightly less than 400 micrometers. On the other hand, others have reported that resolutions below 100 micrometers are possible with CCD-based gamma cameras in photon counting mode.

To investigate possible integration of photon counting into our dual modality imaging system, we have developed a low cost camera based on the cheapest electron-multiplication CCD on the market (the Texas Instruments TC253). In addition, we have also evaluated more costly commercial systems (Princeton Instruments/Acton PhotonMax 512B and the Andor Luca). Additional sensitivity was accomplished by reducing the field-of-view of the camera. Because the optical transport of scintillation light is related to the field-of-view by a quadratic, reducing the FOV by a factor of 4-5 leads to 16-25 times more photons reaching the CCD.

The Texas Instruments TC253 is a VGA-format Impactron sensor with electron multiplication gain up to 1000. The sensor is cooled with a 3 stage Peltier system. Although rated at -10 C, we have successfully operated the TC253 at -42 C. The interface to the sensor consists of analog line drivers controlled digitally by a commercial field programmable gate array (FPGA – National Instruments PCI-4312). Software for clocking the CCD was developed in house using National Instruments LabVIEW. Extensive testing in dark reveals that the TC253 is

sensitive to single electrons. Unfortunately, an unspecified characteristic of this chip is a relatively large spurious charge (2-4 electrons per pixel). Because this charge is also multiplied by the multiplication registers, it effectively blinds the camera to the faintest flashes of light. We do however envision that the TC253 camera will make an effective integration camera, and efforts are underway to completely eliminate all dark current through more cooling. A 2nd generation TI Impactron chip (TC247) is available with lower spurious transfer charge and would essentially be a drop-in replacement for the TC253, although at 6 times the cost. This sensor has been evaluated in a commercial camera as described below.

The Princeton Instruments/Acton PhotonMax 512B is a top-of-line back illuminated emCCD camera. This camera incorporated the e2v CCD 97 sensor. Using this camera, we have successfully implemented photon counting at 30 frames per second with both cobalt-57 and iodine-125. Surprisingly, photon counting was possible for >100 keV gammas without electron multiplication, using the traditional readout port of the sensor (7 electron read noise). We have also evaluated the Andor Luca, a budget emCCD camera based on the TI TC247 front illuminated interline sensor. The camera has potential for photon counting, although data collection speed was reduced due to the computer interface (USB versus CameraLink).

The original plan was to utilize back-illuminated charge coupled-devices (CCDs) with quantum efficiencies approaching 95% to capture optical photons generated by gamma-ray interactions with a scintillator. In initial studies though, it was discovered that significantly long integration times (on the order of 15 minutes) were required to form quality projections using parallel hole and pinhole collimators. Even with 4 cameras, this would produce unreasonable imaging times if 16 projections were needed for statistical image reconstruction algorithms. The use of backprojection methods, where at a minimum 60 projections are needed, was completely out of the question.

Electron-multiplying CCDs (EMCCDs) are a new class of sensors that include a novel amplifying serial register. In effect, the read noise of a classical CCD can be removed, and single optical photon detection is possible. That said, it should be noted that one cannot distinguish between a pixel with 1 photo-electron and one with 2 photo-electrons.

Nevertheless, experiments with a commercial, back-illuminated EMCCD (Princeton Instruments/Acton PhotonMax 512B) indicated that this technology may be better-suited for a lens-coupled CCD-based gamma camera.

At this time, back-illuminated EMCCD sensors are too expensive to consider a multi-camera system. However, it was noted that Texas Instruments (Japan) produced a low-cost, front illuminated EMCCD: the TC253. A prototype camera was subsequently built using this sensor. Clocking and readout were controlled using a National Instruments Field Programmable Gate Array (FPGA) board. When characterizing the camera, an undocumented 2-4 electron spurious transfer charge was discovered which effectively limits the noise floor. This discovery was confirmed through personal communications with Jerry Hynecek, Ph.D., the inventor of EMCCD technology (Impactron) and who resides in the local area. The prototype TC253 could be cooled to -40 C, allowing must longer integrations than anticipated by the manufacturer.

The noise problems in the TI EMCCD sensor line was fixed in subsequent generations. With this in mind, 4 Andor Luca EMCCD cameras were purchased to form the gamma imaging component of the dual modality system. The Andor Luca is the lowest-cost EMCCD camera on the market, and uses the Texas Instruments TC-247 sensor.
One limitation is that the camera is fixed a -20 C cooling, so integrations over 10 seconds have fixed-pattern problems from hot pixels. Fortunately, this can be corrected in software. The ultimate limitation in integration time is when these hot pixels reach well capacity and begin to bloom.

Despite Andor's marketing claim, only a single Andor Luca can be accessed at a time by a computer with a USB 2.0 bus. Communications with the manufacturer indicate that this will most likely not be fixed in the future, so a work-around was devised. The Division of Advanced Radiological Sciences has a high-performance computing (HPC) cluster running Rocks 4.2 clustering software. This cluster includes 4 compute nodes, which are essentially normal PCs that are automatically administered by a front-end node. If power is lost, the compute nodes are automatically updated without any user supervision.

A similar approach was taken to create a data acquisition system for the 4 Andor Luca cameras. An image was created for the compute node that consists of an operating system (Microsoft Windows XP Professional), National Instruments LabVIEW, the Andor Luca drivers, and a custom LabVIEW program. Using a special boot CDROM, the compute nodes can be converted to data acquisition nodes through an automatic software installation. When data acquisition is complete, the compute nodes can be rebooted, and they will reinstall HPC software.

The custom LabVIEW program on each node contains routines that talk to the Andor Luca camera. After an image is acquired, the image data is published to the front-end node using the National Instruments DataSocket Server mechanism. Using semaphores created in the DataSocket Server, an master application running on the front-end node can control and direct the 4 Andor Luca cameras to simultaneously acquire integration images.

For future work, the data acquisition software will be updated to allow high frame-rate data transfer for photon counting applications. The private Gigabit network that facilitates communications between the compute nodes and the front-end has sufficient bandwidth for transferring video-like data. The DataSocket Server mechanism, however, is a high-level abstraction with significant overhead. A low-level transfer mechanism will be needed to perform list-mode SPECT in real time.

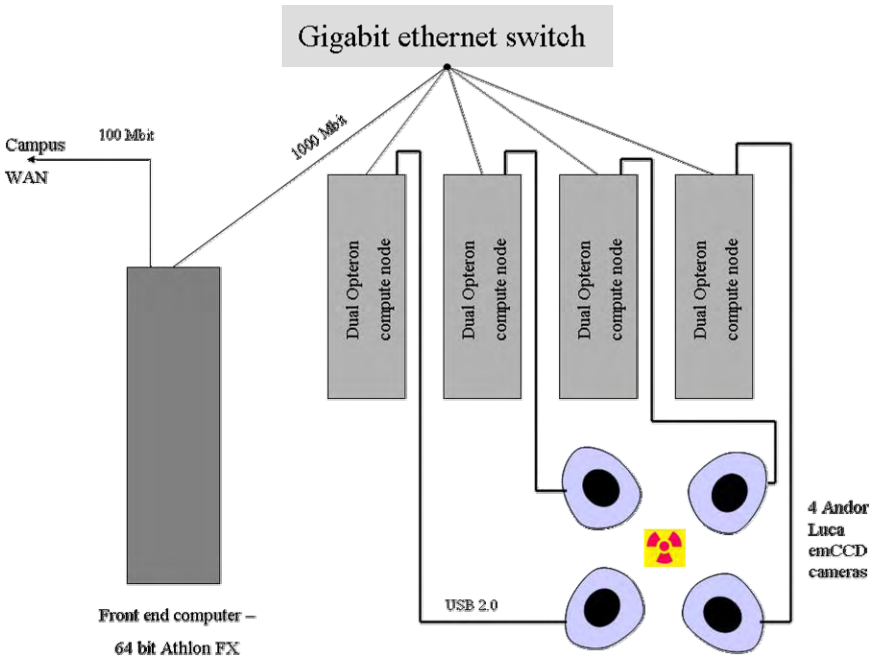

Current architecture for saSPECT component.

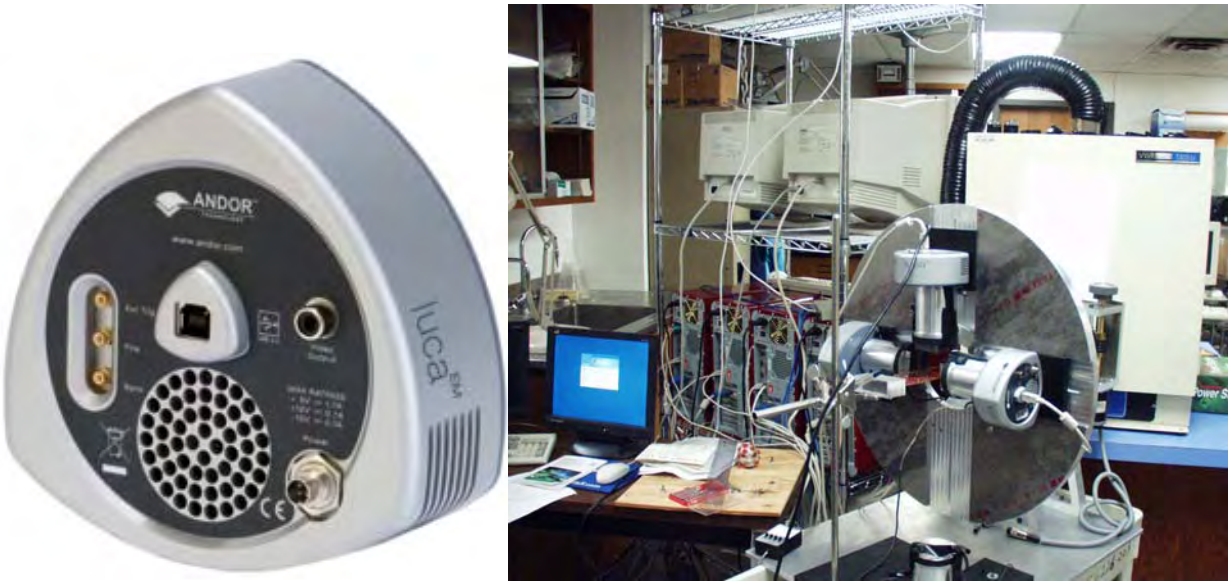

Andor Luca emCCD camera (left) and gantry with 3 mounted cameras (right). Note red cluster in background controlling cameras.

For a system with 10-20 CCD-based gamma cameras, which could be designed for very fast imaging of the breast and axilla, it is evident that the cost per camera must be below $5000. This obviously rules out the most expensive emCCD offerings. Fortunately, recent research by others has shown that truly inexpensive CCD cameras (<$500) can be utilized in lens-coupled CCD-based gamma cameras, provided that sufficient optical amplification is available. This Bazooka SPECT concept (Miller, Barrett, et al) utilizes micro-channel plate-based image intensifiers in the optical chain to facilitate photon counting mode. We are

actively investigating an alternative technology (gas electron multiplication – GEM) to improve the optical coupling in our multicamera system.

We have tested the ability of the highest-sensitivity CCD camera currently available to detect not only an integrated signal but also single-gamma-ray interactions. The appended movie (CD) shows the detection of multiple, single photon events, as the source is moved away from the crystal (single photon events disappear) or near it (multiple events).

We note that if the LET camera is used to detect the skin of the animal and the SPECT camera is used simultaneously, the perception of the distribution is significantly improved. In the figure below, the MDDP distribution identifies the skeleton. This is also true of X-ray imaging, where CT and PET or SPECT can be used together.

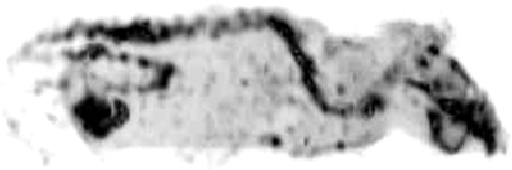

DUAL MODALITY IMAGE RECONSTRUCTION

One can consider the following parallel image reconstruction chains for LET and small animal SPECT. In the naïve approach, there is no communication between these 2 chains.

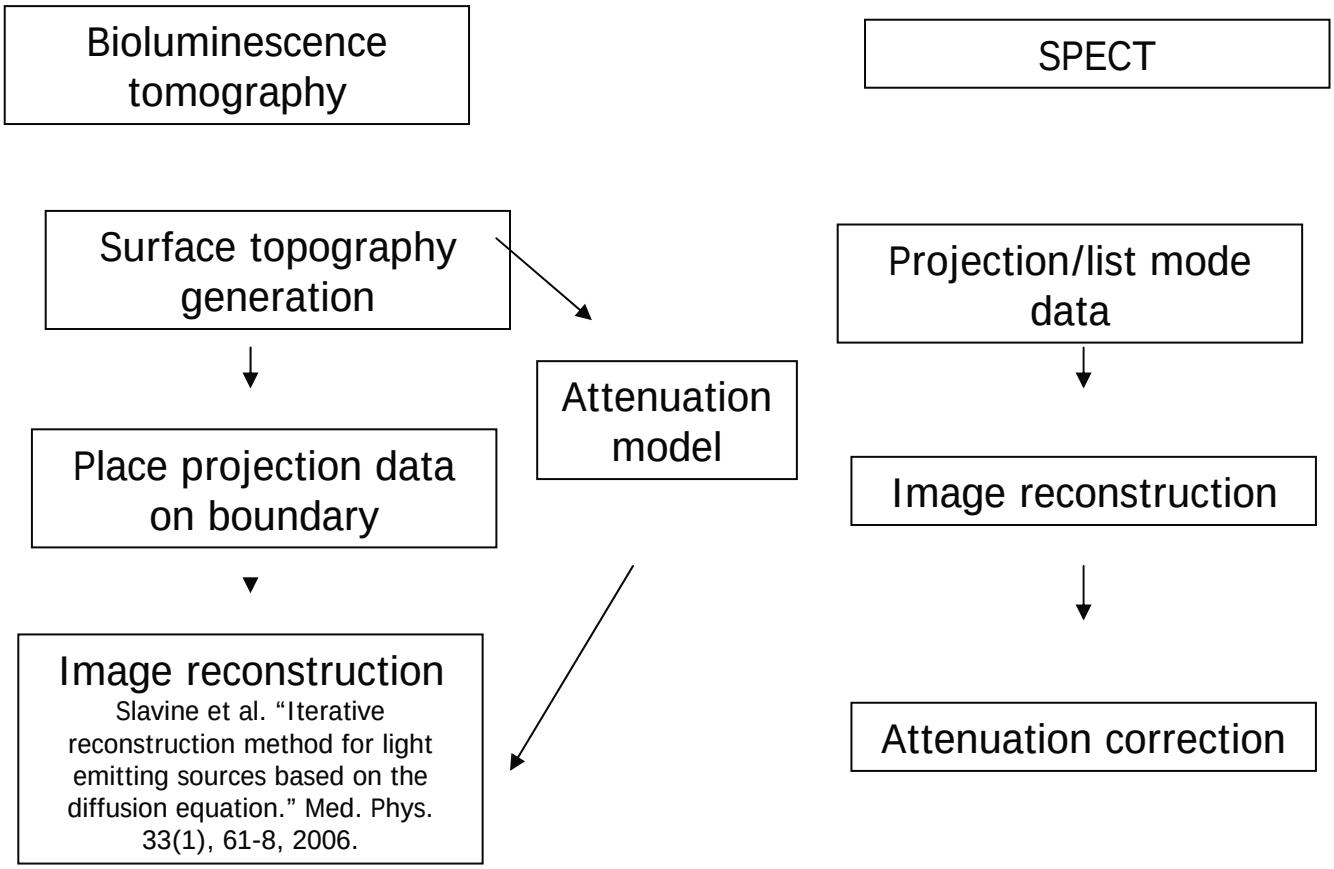

One key step in the optical image reconstruction is the surface topography reconstruction and the formation of attenuation models. We were inspired to ask if this surface topography could likewise be used to generate scatter-correction models for the nuclear medicine component, as shown in the following figure:

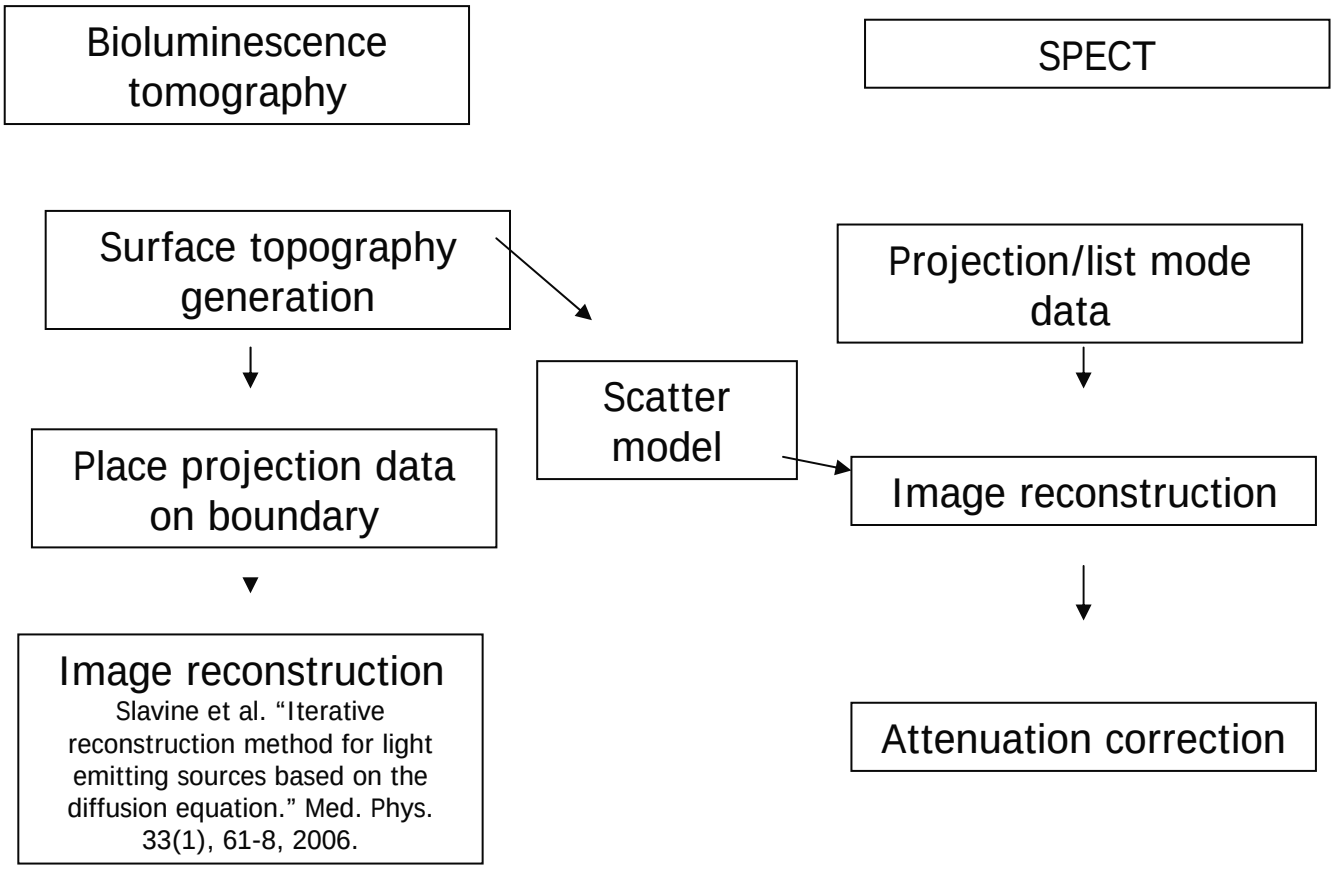

This model would be especially appropriate for imaging with iodine-125, where ½ of the detected photons have been scattered once. We have developed Monte Carlo methods using MCNPX (LANL) where the optical surface topography is used to generate a homogeneous object for scatter map generation. The voxelized version of the mouse is optimized for MCNPX using the Ohtsuki algorithm in 2D. Further optimizations are potentially possible in 3D, but no higher dimension algorithms could be found in the literature.

FLUORESCENCE IMAGING.

We note that in addition we can merge bioluminescence with fluorescence imaging. If a dextran tagged with Alexa Flours is injected in a mouse illuminated in white light, the autofluorescence presents a background signal 14 times lower than the signal produced by the fluor. In the whole body image the prominent light source is the heart as the polymer remains in the vasculature

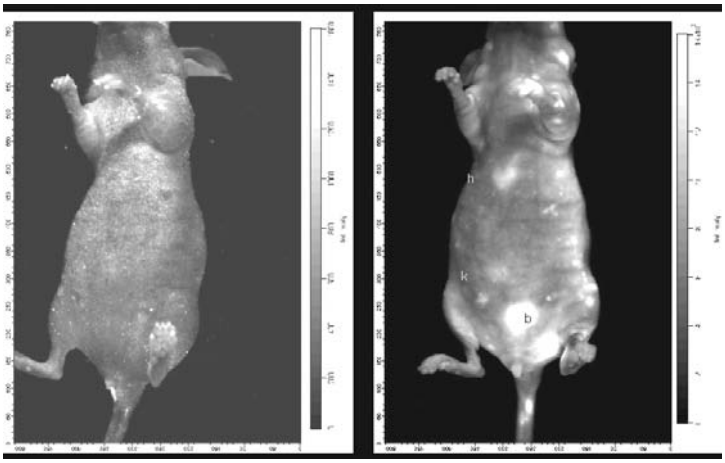

The left-hand side image shows the pre-injection mouse, the one at right was acquired 3 min PI. Heart, kidney and bladder are the highest intensity sources (note that the kidney is seen through the mouse body in this ventral view).
If the same agent is injected in a mouse in which an MDA-MB231 breast cancer tumor grows in the mammary fat pad, a whole body image shows anatomic details as well as the tumor; a higher magnification image reveals the viable tumor against a darker halo around the tumor, produced by absorption of the light used to induce fluorescence by blood vessels and by a dense population of extravasated red blood cells.

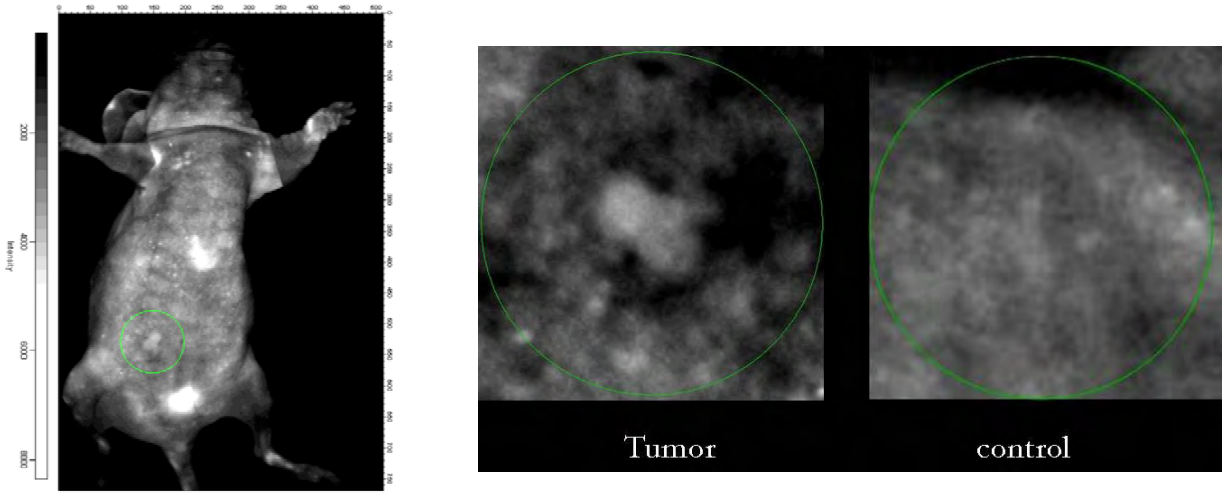

Images in fluorescence of a tumor-bearing mouse and higher magnification view of perfusion of tumor compared to contralateral mammary.

SPECT IMAGING AGENTS

Returning to SPECT, we have participated with our colleagues in evaluating a new imaging agent, Clioquinol. This agent targets areas with high transition metal concentrations. While it was originally developed to image plaque in Alzheimer's disease it is also effective in breast cancer. Thus we show below that the agent stains quite effectively a lymph node metastasis of breast cancer

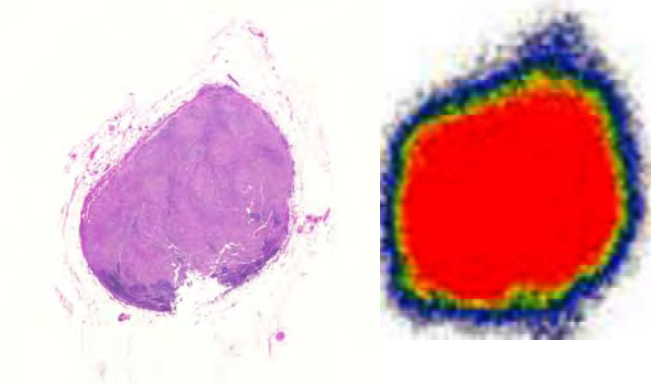

The figure shows the radioactivity distribution of ^{125}I-CQ in a tissue slice of lymph node together with a standard tumor stain in an adjacent slice. Intense uptake is shown in red, less intense in blue.

We also injected CQ into nude mice and obtained screen images without collimation

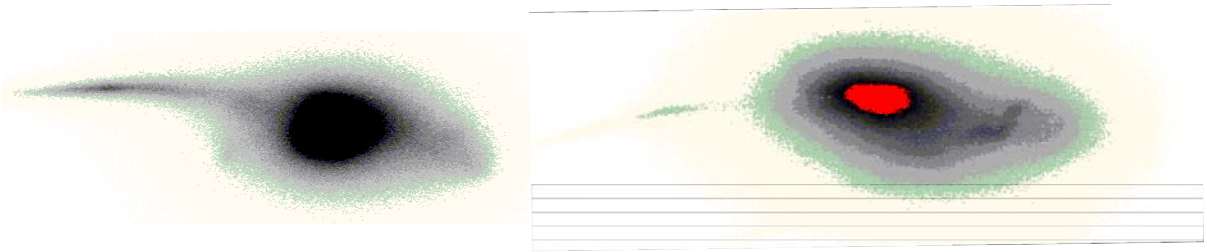

Storage phosphor screen images of BALB/c nude mice injected with ^{125}I-CQ: tumor-bearing mouse at right (MDA-435 Human BrCa) vs control at left. The control mouse shows a diffuse distribution but the tumor-bearing mouse shows accumulation in the flank.

KEY RESEARCH ACCOMPLISHMENTS

1) Completion of software for Light Emission Tomography (LET). Our reconstruction approach consists of two steps: light surface reconstruction to determine the geometry of turbid media boundaries and then source reconstruction inside the tissue by using a deblurring EM algorithm based on the diffusion equations. The method accounts for scattering.
2) Device: most tests are accomplished using a four-camera device. We have improved the noise performance of our CCD cameras with better cooling and with improved optics.
3) Techniques for the detection of metastases. We have used LET with the 4-headed device to detect metastases in the lung and head. We have demonstrated our ability to detect millimeter or sub-millimeter metastases in mice by light emission.
4) We have begun assessment of perfusion using fluorescence imaging. This is performed using the same device developed for LET.

5) we have continued development of a camera for micro-SPECT based on cooled, electron-multiplied Charge-Coupled Devices (EMCCDs) with which we are performing ongoing imaging experiments. We have developed software for image reconstruction with multiple pinholes.
6) We have also collaborated on the assessment of a new, promising SPECT imaging agent, clioquinol or Iodinated hydroxyquinoline.

REPORTABLE OUTCOMES

The methodology of Light Emission Tomography has been summarized in a recent publication: NV Slavine, MA Lewis, E Richer and PP Antich, Iterative reconstruction method for Light Emitting Sources based on the Diffusion Equation, Medical Physics 33 (61-68) 2006.

The application of LET to phantoms and to mice is reported in:
E Richer, NV Slavine, MA. Lewis, T Soesbe, S Seliounine, X Li, E Tsyganov, VD Kodibagkar, JW. Shay*, G.C. Gellert*, Z. G-D*, VJ. Bhagwandin*, RP. Mason, PP. Antich Light Emission Tomography: Visualizing Small Animal Biology in three dimensions. Prepared for submission, preprint enclosed.

Progress in multi-pinhole SPECT system software has been presented at the Second Biannual Workshop on Small-Animal SPECT imaging in Tucson, Arizona by NV Slavine (power point presentation).

Progress in Scatter Correction for Low-Energy Small Animal SPECT using Optical Surface Topography in a Dual Modality Imaging System has been presented at the Second Biannual Workshop on Small-Animal SPECT imaging in Tucson, Arizona by MA Lewis (power point presentation).

Development of the emCCD-based gamma camera was reported in a peer-reviewed publication in the IEEE Transactions on Nuclear Science by TC Soesbe.

CONCLUSION

In conclusion, while the integration of the two modalities needs to be perfected to achieve maximum imaging usefulness, we have made progress towards establishing an imaging method and agents capable of translation to the clinic.

APPENDICES

1. NV Slavine, MA Lewis, E Richer and PP Antich, Iterative reconstruction method for Light Emitting Sources based on the Diffusion Equation, Medical Physics 33 (61-68) 2006

2. Soesbe TC, Lewis MA, Richer E, Slavine NV, Antich PP: Development and Evaluation of an EMCCD based Gamma Camera for Preclinical SPECT Imaging. *IEEE Transactions on Nuclear Science* 54(5), 1516-1524, 2007.

3. Lewis MA*, Slavine NV, Soesbe T, Richer E, Antich PP: Scatter Correction for Low-Energy Small Animal SPECT using Optical Surface Topography in a Dual Modality Imaging System. 2nd Biannual Workshop on Small-Animal SPECT Imaging, 8-10 March 2006, Tucson, Arizona (oral presentation).

4. Slavine NV, Soesbe T, Lewis MA, Richer E, Antich PP. Construction, calibration and evaluation of a tissue phantom with reproducible optical properties for investigations in light emission tomography. IEEE Dallas Engineering in Medicine and Biology Workshop.

Iterative reconstruction method for light emitting sources based on the diffusion equation

Nikolai V. Slavine,[a] Matthew A. Lewis,[b] Edmond Richer,[c] and Peter P. Antich[d]
Advanced Radiological Sciences, Department of Radiology, University of Texas Southwestern Medical Center, 5323 Harry Hines Boulevard, Dallas, Texas 75390-9058

(Received 14 June 2005; revised 13 October 2005; accepted for publication 17 October 2005; published 20 December 2005)

Bioluminescent imaging (BLI) of luciferase-expressing cells in live small animals is a powerful technique for investigating tumor growth, metastasis, and specific biological molecular events. Three-dimensional imaging would greatly enhance applications in biomedicine since light emitting cell populations could be unambiguously associated with specific organs or tissues. Any imaging approach must account for the main optical properties of biological tissue because light emission from a distribution of sources at depth is strongly attenuated due to optical absorption and scattering in tissue. Our image reconstruction method for interior sources is based on the deblurring expectation maximization method and takes into account both of these effects. To determine the boundary of the object we use the standard iterative algorithm—maximum likelihood reconstruction method with an external source of diffuse light. Depth-dependent corrections were included in the reconstruction procedure to obtain a quantitative measure of light intensity by using the diffusion equation for light transport in semi-infinite turbid media with extrapolated boundary conditions. © *2006 American Association of Physicists in Medicine*. [DOI: 10.1118/1.2138007]

Key words: bioluminescence imaging, diffusion equation, boundary condition, deblurring EM method, 3D-reconstruction

I. INTRODUCTION

A. Overview

Small animal imaging using bioluminescence sources (as with the Renilla or firefly luciferase reporter systems) has attracted much attention in recent years.[1–4] Cells transfected with light emitting probes can also be used to detect gene expression *in vivo*.[5–7] *In vivo* imaging of bioluminescence sources in animals offers a unique opportunity for noninvasive studies of cellular or molecular events to better understand the effects of human disease in animal models.[8,9] For efficient detection of bioluminescent probes in living animals, it is necessary to use high sensitivity low-noise detectors, such as cooled charged-coupled devices (CCDs) while advanced algorithms may be needed for image reconstruction. Several techniques have been developed in order to determine the location of an object in strongly scattering media using visible or near-infrared light.[10–13]

The solution uniqueness for bioluminescent imaging (BLI) reconstruction can be strengthened by incorporation of *a priori* information on the animal anatomy and optical properties.[14–17] This is a significant problem for any BLI reconstruction algorithm, and effective algorithms for distributed BLI sources are still an active area of research.

B. Reconstruction methods

Reconstruction algorithms must take into account the main optical properties of biological tissue: light absorption, scattering, and reflection at major interfaces. In this case, a model describing light transport in turbid media is critical for any reconstruction technique.[18] Widely used methods are the diffusion approach and Monte Carlo (MC) simulations,[19,20] both based on the radiative transfer equation (RTE).[10,14,21–23] The RTE is a Boltzmann-type nonlinear transport equation for the photon intensity. This equation is often impossible to solve analytically, and is usually simplified by a diffusion approximation[14,21] that describes the diffuse part of the radiative intensity. A disadvantage of this approach is the inaccuracy in predicting the light distribution near light sources and boundaries. The MC simulation, based on the RTE, is a computational method, which models the individual photon interactions in turbid media. This method is an accurate and powerful way to study photon transport in tissue requiring no simplifications, but needing extensive computational resources. This diffusion approach has been shown to be in good agreement with MC simulations and experiments.[1,19,24,25]

Three-dimensional- (3D-) source reconstruction is the primary goal of light emission tomography (LET), and this problem is formulated as an inverse problem based on the diffusion approximation.[14,26–28] Good results for 3D-optical reconstruction have also been obtained by using the finite element method (FEM).[29–32] We have recently completed preliminary tests of a bioluminescent LET system with multiple rotating, high sensitivity CCD cameras[33,34] to obtain 3D reconstructed images. Tests with different phantoms verify the utility of the approach and the accuracy of the 3D-source reconstruction algorithm.

In Ref. 31 two sources with $\sim$10 mm separation were reconstructed using a FEM algorithm. We present reconstruction results for two sources with the same separation using our new algorithm. The problem we are addressing

here is that of relating image to source intensity. For this purpose, using the diffusion approximation and balancing the internal and external intensities on the boundary of the media, we determine an initial order approximation for the photon fluence, and subsequently apply the iterative deblurring EM method[35,36] to obtain a final reconstruction result.

C. Light diffusion in tissue

To estimate the position and intensity of bioluminescence source one can describe photon propagation through tissue by the diffusion approximation:

$$\frac{1}{c_n}\frac{\partial\varphi(r,t)}{\partial t} = -D\nabla^2\varphi(r,t) - \mu_a\varphi(r,t) + S(r,t), \tag{1}$$

where $\varphi(r,t)$ is the isotropic fluence rate, D and μ_a are the diffusion and absorption coefficients, respectively, $S(r,t)$ is the internal light source distribution, and $r(x,y,z)$ is the distance away from the source in time t. For steady-state diffusion, according to the dipole source model[24,25] with extrapolated boundary, the photon fluence rate at the physical boundary can be expressed as a sum of contributions from the positive internal source $\varphi(r_s)$ and its negative image source above the tissue $\varphi(r_i)$:

$$\varphi(r) = \varphi(r_s) - \varphi(r_i) = S_0 e^{-\mu_{\text{eff}} r_s}\frac{(4\pi D)^{-1}}{r_s} - S_0 e^{-\mu_{\text{eff}} r_i}\frac{(4\pi D)^{-1}}{r_i}, \tag{2}$$

where $r_s=(z_s^2+r^2)^{1/2}$ and $r_i=(z_i^2+r^2)^{1/2}$ is the distance from the source and its image to point on the boundary, $\mu_{\text{eff}}=(\mu_a/D)^{1/2}$ is an effective attenuation coefficient. The surface radiance on the physical boundary is

$$L(r) = \frac{1}{4\pi}\varphi(r) + \frac{3}{4\pi}[\varphi(r_s)\Delta_s + \varphi(r_i)\Delta_i],$$

$$\Delta_\alpha = \frac{z_\alpha}{r_\alpha^2}(1 + r_\alpha\mu_{\text{eff}})D \quad \text{for } \alpha = s,i. \tag{3}$$

The reflectance of photons at the tissue-air interface that will reduce the fluence rate out of the tissue:

$$R(r) = R(r_s) - R(r_i) = \varphi(r_i)\Lambda_s - \varphi(r_i)\Lambda_i,$$

$$\Lambda_\alpha = \frac{z_\alpha}{r_\alpha^2}(1 + r_\alpha\mu_{\text{eff}}) \quad \text{for } \alpha = s,i. \tag{4}$$

Solutions for spherical surface or solid sources for homogeneous medium were presented previously[37] and those authors consider this approach useful for good qualitative estimates of signal level and positions of light sources for BLI.

D. Phantoms and light sources

We fabricated the phantoms and light sources following procedures from published articles.[38–40] The heterogeneous mouse shaped phantom (with dimensions that approximate the size of a typical mouse) was fabricated from clear polymer resin with TiO_2 powder as scattering material ($\mu_s'=9\ \text{cm}^{-1}$) and Pro JeT 900 NP ink as absorption medium ($\mu_a=0.3\ \text{cm}^{-1}$).[40] In addition, formalin fixed mouse organs—heart, kidneys, and liver—were placed close to the anatomical position inside the mouse phantom. A 3 mm-diam spherical light source (peak emission about 580 nm) was placed between heart and liver. The cylindrical shaped phantom, 5 cm long and 3 cm diameter, has a circular aluminum base through which an 18 gauge hypodermic needle was inserted. There are five different radial positions for the needle ranging from the center to just below the surface, with step size of 2.54 mm. The light is emitted from the tapered end of the optical fiber 1 mm in size which was threaded through the needle;[41] the peak wavelength of the light source tuned at 580 nm matches that of the firefly luciferase[39] *in vivo* spectrum, which extends to 680 nm; the source is isotropic and reproducible within the phantom. Single and multiple light sources are possible. The phantom can be rotated through 2π degrees for imaging with a single CCD camera; the phantom material is a solidified mixture of distilled water, agarose (Sigma A0169), and Intralipid. By changing the concentration of Intralipid from 0.25% to 2% the value of μ_s' can be varied from 2.5 to 15 cm^{-1} without any significant change to the μ_a.[38] These reduced scattering coefficients match those of typical mouse tissues.

II. IMAGE RECONSTRUCTION METHOD

Our reconstruction approach consists of two main steps: 3D-surface reconstruction used to determine the geometry of boundary—used to infer the distances from source to each point of the boundary—followed by estimation of source position and intensity inside the tissue by using deblurring EM algorithm based on diffusion equations (2)–(4).

A. 3D-surface reconstruction

The surface reconstruction is based on the ML method.[42] In this algorithm a sequence of image estimates is generated for the kth iteration:[43]

$$n_j^{k+1} = \frac{n_j^k}{\sum_{i=1}^{I} a_{ij}}\sum_{i=1}^{I}\frac{m_i}{q_i^k}$$

where

$$q_i^k = \sum_{j=1}^{J} a_{ij} n_j^k, \tag{5}$$

where n_j^{k+1} and n_j^k are image intensity values in the new and current estimate for the voxel j (the interior of the body is subdivided into voxels). The measured data m_i for each angular position of CCD collected along lines i which connect a voxel on the object's surface to the CCD, gave values proportional to the light intensity detected by the pixel; q_i^k is the expected count in line i for the current estimate n^k, and a_{ij} is the probability that a light quantum emitted at voxel j will be detected in the line i. Figure 1 shows examples of ML surface reconstruction for the cylindrical phantom with two

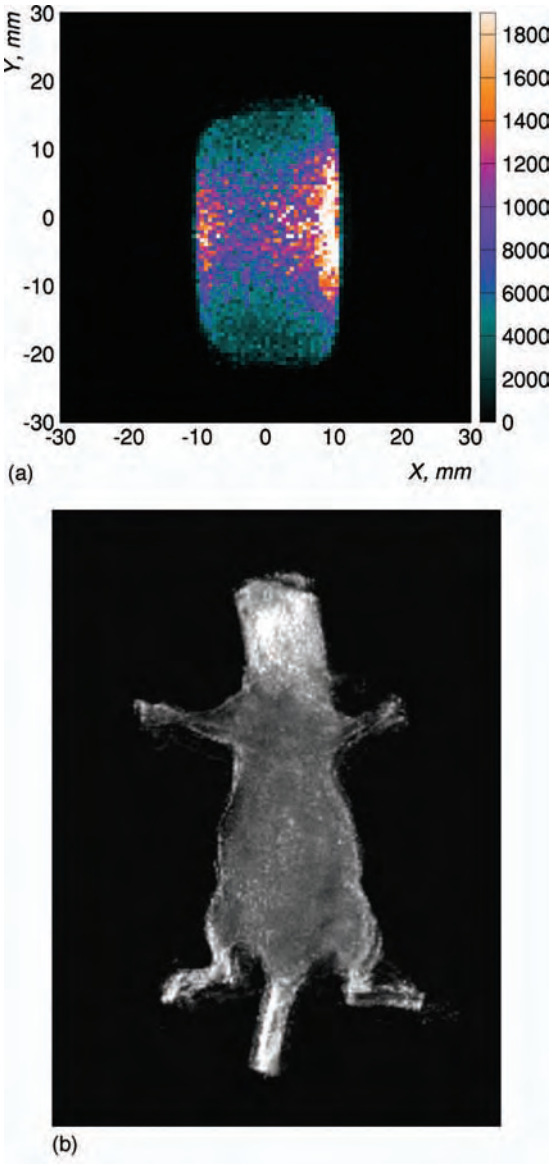

FIG. 1. 3D-surface reconstruction by ML method for phantom with two interior sources (a) and for living nude mouse from reflected light (b).

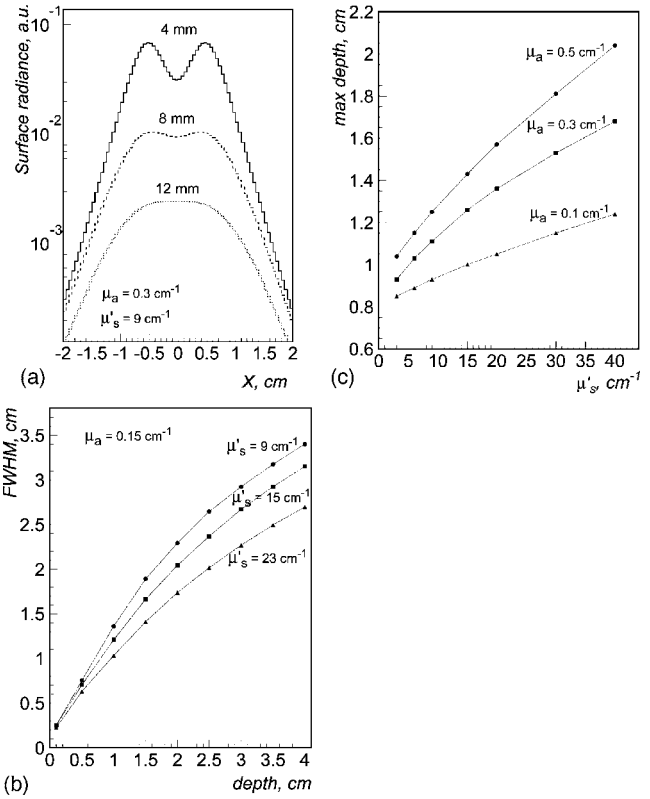

FIG. 2. Surface radiance peaks vs depth for two sources separated by 10 mm (a), FWHM as a function of source depth calculated for different reduced scattering coefficients (b), and maximum depth at which the two sources can be distinguished as separate peaks. The intensity curves are normalized to one at 1 mm depth.

interior light sources and for an externally illuminated living nude mouse. The second image demonstrates our ability to follow surfaces of varying curvature.

This approach permits not only a good estimation for irregular boundaries, but reconstructs location and intensity with a good resolution of any light sources emitted in air (in this case we can neglect correction for light diffusion). Note that in BLI experiments we in reality can use only a small part of the object surface due to limited light propagation in tissue. In this case we do not necessarily need to reconstruct the surface of the full mouse body or phantom. A more difficult problem is that of obtaining information about complex surface of heterogeneous objects (organs) inside the body or phantom.

B. 3D-source reconstruction inside the tissue

The diffusion approximation is very useful for estimating the surface photon intensity and light spot size depth-dependence for BLI experiments,[1,37] especially in the case of *in vivo* small animal studies.[1] Figure 2(a) shows surface radiance for two light sources separated by 10 mm embedded at different depths. Note that for these specific optical properties and source separation at the depth of 12 mm the two intensity peaks coalesce. The light spot size [Full width at half maximum (FWHM)] at the phantoms surface is shown in Fig. 2(b) as a function of depth for different values of μ_s' corresponding to different concentration of Intralipid. For the same value of the absorption coefficient, higher scattering coefficients give lower photon intensity levels but a better spatial resolution [see Eq. (3) and Ref. 1]. Figure 2(c) shows as a function of μ_s' and μ_a the maximum depth at which the two sources can be distinguished as separate peaks in the surface radiance. For typical optical properties of small animal tissues the maximum imaging depth is $\sim$1–1.5 cm. This depth is considered sufficient for imaging small animals such as mice and rats. Further advances are possible by examining the wavelength dependence of the emitted spectrum.

The reconstruction algorithm consists of the following steps.

Step 1. In order to estimate the source location we back-project our experimental data into the volume discretized

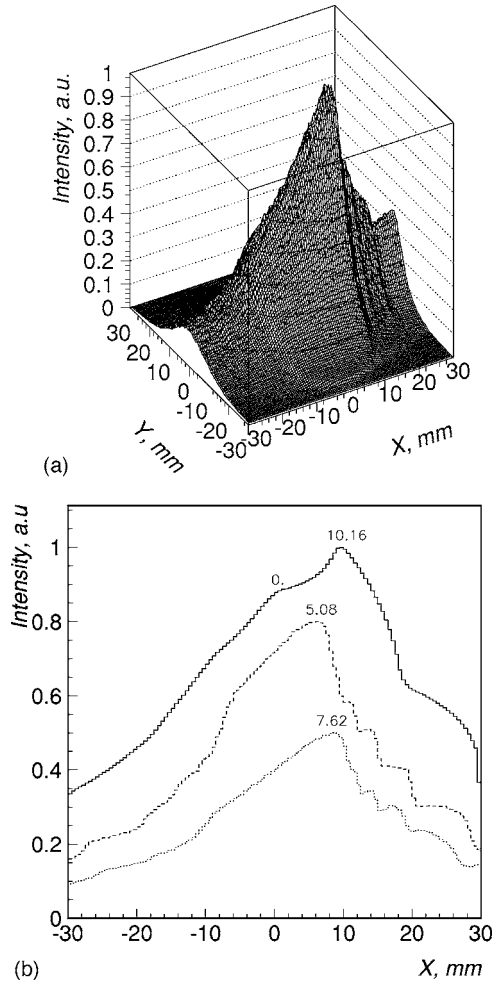

FIG. 3. 2D histogram showing maximum intensity for Intralipid phantom with a single source located at 7.62 mm from the center of system coordinate by X axis (a); slices of maximum intensities for phantoms with sources positioned at various X coordinates (b). Voxel size 0.5 mm.

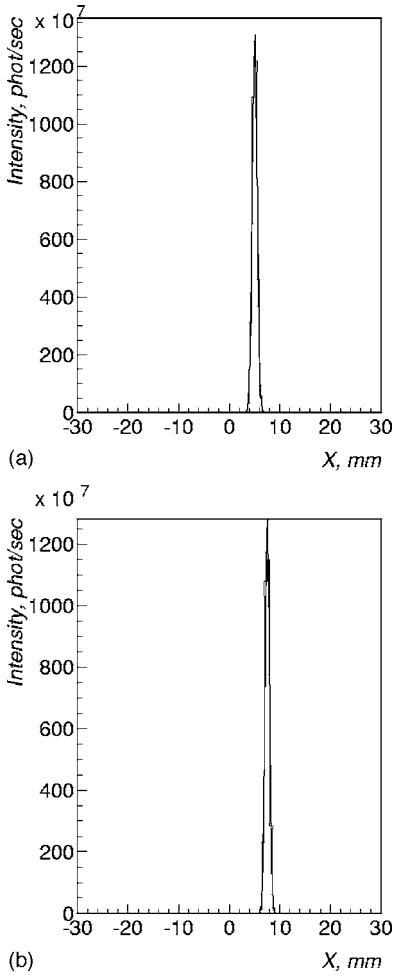

FIG. 4. 3D-reconstructed images of 1% Intralipid-filed medium phantoms displaced 5.08 mm (a), 7.62 mm (b) from the center of system coordinate by X axis.

into $N_x \times N_y \times N_z$ voxels. Two-dimensional (2D) histograms are then generated for each of the N_z depth planes and the X, Y position of relevant intensity peaks is determined [Fig. 3(a)]. Combining the results from all depth planes we obtain estimations for X, Y, and Z coordinates of all light sources in the reconstructed volume [Fig. 3(b)]. If the position of the light source exceeds the maximum detectable depth for *all imaging directions* [Fig. 2(a) for 12 mm depth], we need to use a more sophisticated method to obtain source coordinates estimates (FEM, MC, or Ref. 50), or use *a priori* information obtained from another imaging system (for example, CT, MRI, or OPET[44]) to estimate the heterogeneous optical properties of the intervening tissues.

Step 2. After estimation of source position we can take into account reflection on boundary[45–47] (4), calculate intensity values for each voxel j, and subtract this reflection contribution. We obtain the transmitted part of intensity from the CCD data. The diffusion equation is used to determine the balance intensities for internal sources N_s for the surface element in a single voxel.

Step 3. Next for each voxel j we can determine a "zeroth" order approximation φ_j^0 (i.e., initial guess as an input image, which contains all diffuse light information) using the solution for photon fluence:

$$\varphi_j^0 = (\rho \otimes \varphi + \hat{n})_j \cong \frac{1}{\sum_{i=1}^{I} x_{ij} p_i^t} \sum_{i=1}^{I} x_{ij} p_i^0 \sum_{s=1}^{s=N_s} S_o' \times \exp(-\mu_{\text{eff}} r_{js})/r_{js}, \quad (6)$$

where ρ is a point-spread function, φ is a real value of photon fluence, $\hat{n}$ is a noise term, and x_{ij} is the path length of line i through voxel j, p_i^t and p_i^0 are intensities in CCDs from source in media and in air. Here we have utilized the basis function from the semi-infinite geometry as a first approximation to the diffuse photon propagator.

Step 4. After correcting all voxels we apply the deblurring EM algorithm[36] for final 3D-image reconstruction by using approximation (6)

TABLE I. Source positions and FWHM for *X*, *Y*, and *Z* profiles for the air and Intralipid phantoms reconstruction.

	Air				Intralipid			
		FWHM				FWHM		
X position in phantom, (mm)	*X* position	*X*	*Y*	*Z*	*X* position	*X*	*Y*	*Z*
Single source phantoms								
0.0	−0.08	0.89	0.91	0.90	0.098	1.15	1.18	1.16
2.54	2.58	0.91	0.93	0.92	2.64	1.18	1.21	1.20
5.08	5.03	0.86	0.89	0.88	5.06	1.19	1.22	1.20
7.62	7.60	0.89	0.92	0.91	7.52	1.04	1.09	1.08
10.16	10.01	0.91	0.93	0.92	9.98	1.20	1.24	1.19
Dual source phantom								
0.0	0.07	1.05	1.09	1.06	−0.25	1.32	1.38	1.33
10.16	10.03	1.05	1.08	1.08	10.27	1.17	1.22	1.18

$$\varphi_j^{n+1} = \varphi_j^n \left\{ \hat{\rho} \otimes \left(\frac{\varphi_j^0}{\rho \otimes \varphi_j^n} \right) \right\}, \tag{7}$$

where $\otimes$ denotes convolution procedure based on the discrete fast Fourier transform (FFT).[48] Parameters ρ and $\hat{\rho}$ are the deblurring kernels (for example, Gaussian functions) and can be changed with number of iterations n.

III. RESULTS

In our imaging system multiple high sensitivity CCD cameras simultaneously record views from different angles and a computer controlled rotation mechanism allows imaging at intermediate angular positions, as required for surface and interior sources 3D reconstructions. The CCDs data for each of the twenty (18° angle step) positions were combined for all rotation angles and used for reconstruction procedure.

A. Single source phantom

The field of view of $60 \times 60 \times 60$ mm was subdivided into voxels of 0.5 mm^3 in size. The deblurring kernel parameters ρ and $\hat{\rho}$ were equal and started at 6 mm (first few iterations) and reduced to 1.2 mm during the 310 iterations. Figure 4 shows the example of *X* profiles (*Y* and *Z* positions of sources were in the center of system coordinate) for the deblurring EM reconstructed sources at 5.08 and 7.62 mm [compare with Fig. 3(b)]. Each profile is fitted with a Gaussian function, and the FWHM of the distribution is taken as the reconstructed source size (see Table I for results for all source positions).

It can be seen that the reconstructed source sizes are in excellent agreement with the actual size. The total light intensity in air (not shown here) and Intralipid differed by less then 5%. For example, for phantom with source displaced by 10.16 mm in air the emitted light intensity was 1.44×10^{10} photon/s vs 1.37×10^{10} photons/s in Intralipid.

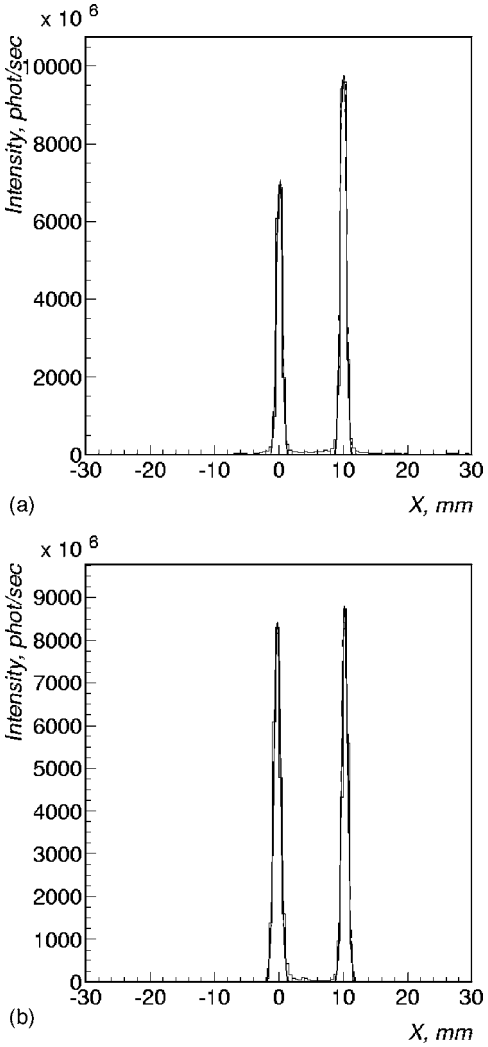

FIG. 5. 3D reconstruction for dual source phantom with separation 10.16 mm: (a) in air and (b) in 1% Intralipid phantom.

B. Dual source phantom

The field of view for this phantom was same as for single sources: $60 \times 60 \times 60$ mm with voxel size 0.5 mm^3. The deblurring kernel parameters ρ and $\hat{\rho}$ were equal and varied from 9 mm (few first iterations) to 1.2 mm during the 150 iterations. Figure 5 shows the *X* profiles for the EM deblurring reconstructed dual point source with 10.16 mm separations in air and in Intralipid [compare with Fig. 3(b)]. The values of FWHM obtained from the Gaussian fit are taken as reconstructed source sizes and are in a good agreement with physical dimensions (see Table I). The two optical sources in air were not identical.

The total light intensity in air and Intralipid differed by less than 8%—intensity in air 9.6×10^9 photon/s vs 8.8×10^9 photons/s in Intralipid.

C. Volume size quantification

Quantifying the tumor size is important in cancer research[4,49] as it permits an estimate of cell numbers. PC3-

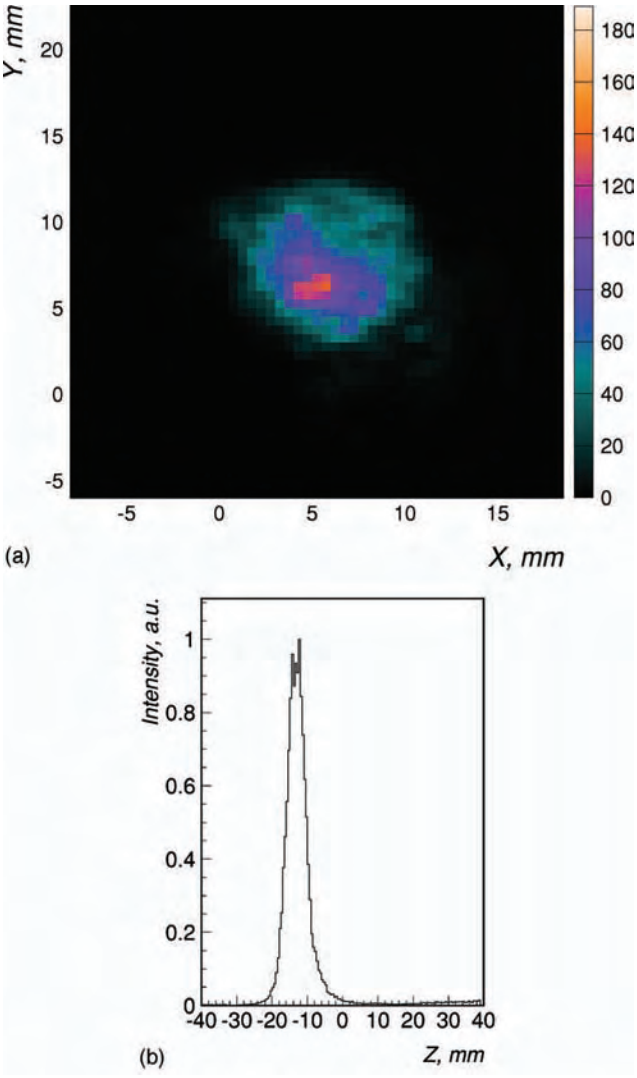

FIG. 6. *XY* and *Z* profiles for BLI tumor size experiments after 5 ML iterations.

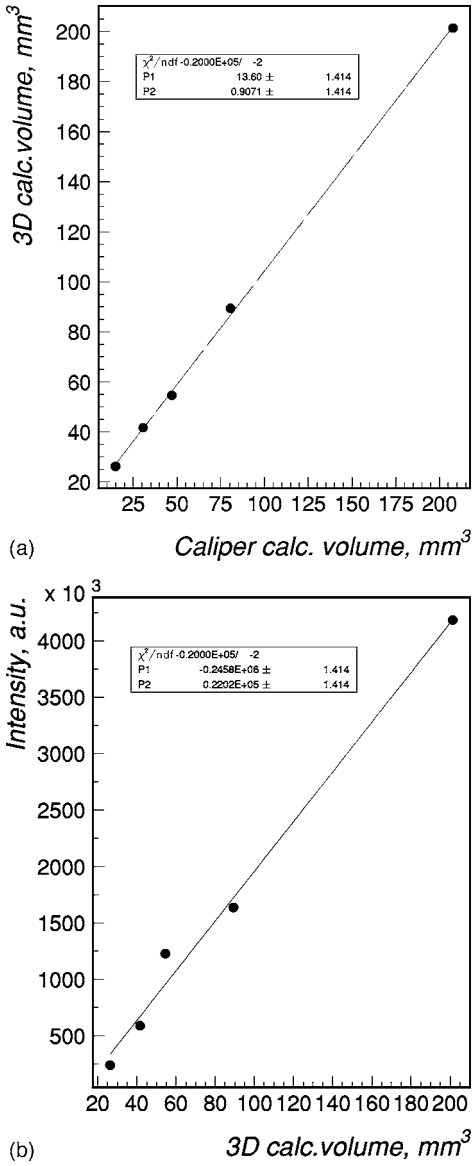

FIG. 7. Correlation of the caliper measurements of tumor size (a) and peak of Intensity (b) with 3D-volume reconstruction.

LUC cells injected in the flank of live nude mice were imaged in the LET system[33] using 5 s exposure time from 20 angular directions for each measurement.

Tumor sizes were determined after reconstruction by ML algorithm (see the example in Fig. 6) using 0.5 mm cubic voxels and five iterations for each calculation. The values of FWHM for *X*, *Y*, and *Z* directions obtained from the Gaussian fit were used to determine tumor sizes. Figure 7(a) shows a good agreement with the caliper measurements in the same tumors and is very close to the line with zero intercept and a slope of 1.

The correlation between the peak intensity of light emitted by a tumor and its volume obtained from ML reconstruction is plotted in Fig. 7(b). Because we used the same conditions for all tumor measurements and same parameters for surface reconstruction we expect that tumor intensity will be correctly indicative of tumor volume.

D. Mouse shaped phantom

In order to demonstrate the source reconstruction in the context of both a complex surface geometry and heterogeneous media we used a phantom that approximates the shape and dimensions of a typical mouse. A superposition of images (source and shape) in Fig. 8 shows that both position and source size were correctly determined by the 3D algorithm. The number of iterations for surface reconstruction was 5, and 100 for source reconstruction. Position of the center after reconstruction $X=1.67$ mm, $Y=5.76$ mm, and $Z=0.51$ mm while FWHM was 3.45, 3.64, and 3.52 mm, respectively.

Here we demonstrate source position reconstruction only: we took into account solution for spherical source[37] and light intensity correction for different optical properties of mouse organs at known location and sizes (*a priori* information). In the reconstruction of *in vivo* experiments, the complex calculations for determining intensities and positions would be greatly facilitated by the necessary information about mouse

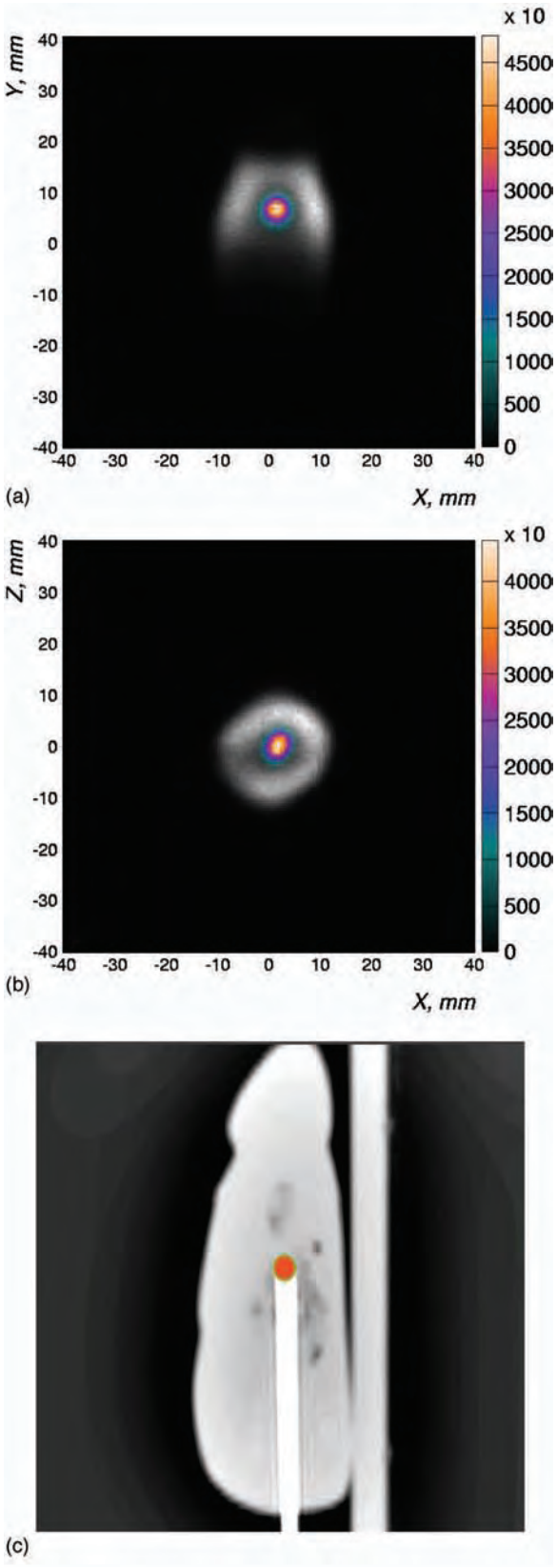

FIG. 8. Coronal (a) and transaxial (b) images of mouse shaped heterogeneous phantom. The center of source was located in position $X=2$ mm, $Y=5$ mm, and $Z=0$ mm. Voxel size=0.5 mm. Black and white image represents boundary of surface estimates and color portion represents image after EM deblurring. (c) Co-registered CT (imaged with GE CT/I, 3D rendering using VolView 2.0, Kitware, Inc), and reconstructed light source.

anatomy and the corresponding heterogeneous optical properties.

IV. CONCLUSIONS

Our phantom and BLI experiments have provided quantitative data showing the tomographic capabilities of the imaging system[33,34] and reconstruction algorithms for appropriate depths. The reconstruction approach is applicable to complex geometries, can be used with any suitable photon propagation model, and is amenable to fast imaging calculations (depending on number of voxels, iterations and amount of experimental data from CCDs). The number of iterations (image updates) in source reconstruction procedure was chosen to get a good agreement between source size resolution and light intensity. The average processing time per image update for ML reconstruction was about 350 ms (Pentium 4) and for deblurring EM procedure was a few seconds (time dependent upon FFT algorithm).

The imaging procedure and reconstruction software were verified using single and dual source phantoms. The source dimensions and separation are in a good agreement with expected values. We find some degree of competition between the source sizes and intensity because optimizing the reconstruction parameters for source intensity may have counter effects on source size. Solution of this problem is based on comparing the spectrum measured in the imaging experiment with that emitted by sources in air and will be outlined in future work.

Image reconstruction can be difficult or even impossible (for heterogeneous media especially) if information is missing due to incomplete data acquisition or sources with limited photon propagation. Our group plans to overcome excessive attenuation with improved technology. However it may be possible to use neural network method with input-dependent weights[50] combined with EM algorithm for missing data[51] or Monte Carlo methods to get useful tool for BLI reconstruction. We are actively investigating alternative algorithms for solving the main problem of BLI—how to reconstruct real distributed sources inside living mouse tissue with high resolution. Information from different small animal imaging modalities[5,44,52] may be useful in providing the additional *a priori* anatomic information.

In conclusion, this study provides further evidence validating the use of bioluminescence to investigate tumor growth (see Fig. 7),[34,49] especially for small tumors or tumors that are less readily accessible to measurement by calipers.[4]

ACKNOWLEDGMENTS

We are grateful to Dr. R. Mason, Dr. R. McColl, Dr. R. Parkey, Dr. V. Kadibagkar, and Dr. E. Tsyganov for their advice and collaboration and our students T. Soesbe and Xiufeng Li for valuable help with BLI and phantom experiments.

[a]nikolai.slavine@UTSouthwestern.edu
[b]matthew.lewis@UTSouthwestern.edu
[c]edmond.richer@UTSouthwestern.edu

[d]peter.antich@UTSouthwestern.edu

[1]B. W. Rice, M. D. Cable, and M. B. Nelson, "In vivo imaging of light-emitting probes," J. Biomed. Opt. **6**, 432–440 (2001).
[2]C. H. Contag and M. N. Bachmann, "Advances in bioluminescence imaging of gene expression," Annu. Rev. Biomed. Eng. **4**, 235–260 (2002).
[3]T. F. Massound and S. S. Gambhir, "Molecular imaging in living subjects: Seeing fundamental biological processes in a new light," Genes Dev. **17**, 545–580 (2003).
[4]Z. Paroo, R. A. Bollinger, D. A. Braasch, E. Richer, D. R. Corey, P. P. Antich, and R. P. Mason, "Validating bioluminescence imaging as a high-throughput, quantitative modality for assessing tumor burden," Molecular Imaging **3**, 1–8 (2004).
[5]R. Blasberg, "In vivo molecular-genetic imaging: Multi-modality nuclear and optical combinations," Nucl. Med. Biol. **30**, 879–888 (2003).
[6]S. R. Cherry, "In vivo molecular and genomic imaging: New challenges for imaging physics," Phys. Med. Biol. **49**, R13–R48 (2004).
[7]V. Ntziachristos, J. Ripoll, L. Wang, and R. Weissleder, "Looking and Listening to light: The evolution of whole-body photonic imaging," Nat. Biotechnol. **23**, 313–320 (2005).
[8]H. R. Herschman, "Molecular imaging: Looking at problems, seeing solutions," Science **302**, 605–608 (2003).
[9]J. Marx, "Building better mouse models for studying cancer," Science **299**, 1972–1975 (2003).
[10]A. D. Klose and A. H. Hielsscher, "Fluorescence tomography with simulated data based on the equation of radiative transfer," Opt. Lett. **28**, 1019–1021 (2003).
[11]V. Ntziachristos, C. Tung, C. Bremer, and R. Weissleder, "Fluorescence molecular tomography resolves protease activity in vivo," Nat. Med. **8**, 757–760 (2002).
[12]A. H. Hielscher, "Model-based iterative image reconstruction for photon migration tomography," Proc. SPIE **3**, 106–117 (1997).
[13]H. Dehghani, B. A. Brooksby, B. W. Pogue, and K. D. Paulsen, "Effects of refractive index on near-infrared tomography of the breast," Appl. Opt. **44**, 1870–1878 (2005).
[14]G. Wang, Y. Li, and M. Jiang, "Uniqueness theorems in bioluminescence tomography," Med. Phys. **31**, 2289–2299 (2004).
[15]G. Wang, E. A. Hoffman, G. McLennan, L. Wang, M. Suter, and J. Meinel, "Development of the first bioluminescent CT scanner," Radiology **229**, 566 (2003).
[16]W. Cong, D. Kumar, Y. Liu, A. Cong, and G. Wang, "A practical method to determine the light source distribution in bioluminescent imaging," Proc. SPIE **5535**, 679–686 (2004).
[17]M. Schweiger and S. R. Arridge, "Optical tomographic reconstruction in a complex head model using a priori region boundary information," Phys. Med. Biol. **44**, 2703–2721 (1999).
[18]S. R. Arridge and J. C. Hebden, "Optical imaging in medicine. II. Modeling and reconstruction," Phys. Med. Biol. **42**, 841–853 (1997).
[19]S. T. Flock, M. S. Patterson, B. C. Wilson, and D. R. Wyman, "Monte Carlo modeling of light propagation in highly scattering tissues. I. Model predictions and comparison with diffusion theory," IEEE Trans. Biol. Eng. **36**, 1162–1168 (1989).
[20]L. Wang, S. L. Jacques, and L. Zheng, "MCML—Monte Carlo modeling of light transport in multi-layered tissues," Comput. Methods Programs Biomed. **47**, 131–146 (1995).
[21]A. Ishimaru, *Wave Propagation and Scattering in Random Media* (IEEE, Oxford, 1977).
[22]S. Shandrasekhar, *Radiative Transfer* (Dover, New York, 1960).
[23]V. Venugopalan and B. J. Tromberg, "Radiative transport in diffusion approximation: An extension for highly absorbing media and small source-detector separations," Phys. Rev. E **58**, 2395–2407 (1998).
[24]M. S. Patterson, B. Chance, and B. C. Wilson, "Time resolved reflection and tranmittance for the non-invasive measurement of tissue optical properties," Appl. Opt. **28**, 2331–2336 (1989).
[25]A. H. Hielscher, S. L. Jacquest, L. Wang, and F. K. Tittel, "The influence of boundary conditions on the accuracy of diffusion theory in time-resolved reflectance spectroscopy of biological tissue," Phys. Med. Biol. **40**, 1957–1975 (1995).
[26]T. J. Connolly and D. J. Wall, "On an inverse problem, with boundary measurements, for the steady state diffusion equation," Inverse Probl. **4**, 995–1012 (1988).
[27]S. R. Arridge, "Optical tomography in medical imaging," Inverse Probl. **15**, R41–R93 (1999).
[28]V. A. Merkel and J. C. Schotland, "Inverse scattering for the diffusion equation with general boundary conditions," Phys. Rev. E **64**, 035601(R) (2001).
[29]M. Schweiger, S. R. Arridge, M. Hiraoka, and D. T. Delpy, "The finite element method for the propagation of light in scattering media: Boundary and source conditions," Med. Phys. **22**, 1779–1792 (1995).
[30]S. R. Arridge, M. Dehghani, M. Schweiger, and E. Okada, "The finite element method for the propagation of light in scattering media: A direct method for domains with nonscatering regions," Med. Phys. **27**, 252–264 (2000).
[31]X. Gu, Q. Zhang, L. Larcom, and H. Jiang, "Three-dimensional bioluminescence tomography with model-based reconstruction," Opt. Express **12**, 3996–4000 (2004).
[32]M. A. Lewis, N. Slavine, E. Richer, and P. Antich, "On the minimally-resolvable separation of few point sources in turbid media," Opt. Lett. (submitted).
[33]E. Richer, N. Slavine, M. Lewis, G. Gellert, Z. Dikmen, V. Bhagwandin, J. Shay, R. P. Mason, and P. Antich, "Three dimensional light emission tomography using multiple rotating CCD cameras," The Third Annual Meeting of the Society for Molecular Imaging, St. Louis, MO, 2004, p. 216, submitted to Nature Methods.
[34]Z. G. Dikmen, G. Gellert, P. Dogan, R. Mason, P. Antich, E. Richer, W. E. Wright, and J. W. Shay, "A new diagnostic system in cancer research: Bioluminescent imaging," Turk. J. Med. Sci. **35**, 65–70 (2005).
[35]Y. L. You and M. Kaveh, "A regularization approach to join blur identification and image restoration," IEEE Trans. Image Process. **5**, 416–427 (1996).
[36]M. Jiang, G. Wang, M. W. Skinner, and J. T. Rubinstein, "Blind deblurring of spiral CT images," IEEE Trans. Med. Imaging **22**, 837–845 (2003).
[37]W. Cong, L. V. Wang, and Ge Wang, "Formulation of photon diffusion from spherical bioluminescent sources in an infinite homogeneous medium," BioMed. Eng. OnLine **3**, 1–6 (2004), http://www.biomedical-engeneering-online.com
[38]R. Cubeddu, A. Pifferi, P. Taroni, A. Torricelli, and G. Valentini, "A solid tissue phantom for photon migration studies," Phys. Med. Biol. **42**, 1971–1979 (1997).
[39]R. L. Larossa, *Bioluminescence Methods and Protocols* (Methods in Molecular Biology) (Humana, 1998).
[40]M. Firbank and D. T. Delpy, "An improved design for a stable and reproducible phantom material for use in near-infrared spectroscopy and imaging," Phys. Med. Biol. **40**, 955–961 (1995).
[41]T. C. Soesbe, N. V. Slavine, E. Richer, and P. P. Antich, "A solid tissue phantom for tomographic bioluminescence imaging studies," Radiology Department of the University of Texas Medical Center, Dallas, 17 December (2004), pp. 1–13 (unpublished).
[42]R. T. Whitaker and J. Gregor, "A maximum likelihood surface estimator for dense range data," IEEE Trans. Pattern Anal. Mach. Intell. **24**, 1372–1387 (2002).
[43]L. A. Shepp and V. Vardi, "Maximum likelihood reconstruction for emission tomography," IEEE Trans. Med. Imaging **1**, 113–122 (1982).
[44]D. L. Prout, R. W. Silverman, and A. Chatziioannou, "Detector Concept for OPET—A combined PET and optical imaging system," IEEE Trans. Nucl. Sci. **51**, 752–756 (2004).
[45]A. Kienle and M. S. Patterson, "Improved solutions of the steady-state and the time-resolved diffusion equations for reflectance from semi-infinite turbid medium," J. Opt. Soc. Am. A **14**, 246–254 (1997).
[46]W. Lihong, "Rapid modeling of diffusion reflectance of light in turbid media," J. Opt. Soc. Am. A **15**, 936–944 (1998).
[47]G. W. Faris, "Diffusion equation boundary conditions for the interface between turbid media: comment," J. Opt. Soc. Am. A **19**, 519–520 (2002).
[48]C. S. Burrus and T. W. Parks, *Discrete Fourier Transform, Fast Fourier Transform and Convolution Algorithms* (Wiley, New York, 1984).
[49]S. H. Thorne and C. H. Contag, "Using in vivo bioluminescence imaging to shed light on cancer biology," Proc. IEEE **93**, 750–762 (2005).
[50]Neural Networks, EE048941, "EM Algorithms," Technion, 2001.
[51]G. J. McLachlan and T. Krishnan, *The EM Algorithm and Extensions* (Wiley, New York, 1997).
[52]J. M. Park and S. S. Gambhir, "Multimodality radionuclide, fluorescence, and boluminescence small animal imaging," Proc. IEEE **93**, 771–783 (2005).

Development and Evaluation of an EMCCD Based Gamma Camera for Preclinical SPECT Imaging

Todd C. Soesbe, *Student Member, IEEE*, Matthew A. Lewis, *Member, IEEE*, Edmond Richer, Nikolai V. Slavine, and Peter P. Antich, *Senior Member, IEEE*

***Abstract*—The electron-multiplying charge-coupled device (EMCCD) offers improved quantum efficiencies (40 to 95%) over a broader range of wavelengths (400 to 900 nm) and a higher intrinsic resolution (<100 μm using photon counting) when compared to photomultiplier tubes. The electron gain achieved in the multiplication register of an EMCCD effectively reduces the readout noise to less than 1 electron/pixel, making them sensitive to single photoelectrons. Our prototype camera uses the Texas Instruments Impactron™ EMCCD model TC253SPD-B0 (7.4 μm square pixels) which is cooled under vacuum to $-50°$C using a four stage Peltier and liquid heat exchanger. Shuttered lens-coupling is used to image the optical light from a 3 mm thick monolithic CsI(Tl) crystal. Precise clocking for the EMCCD is provided by a National Instruments FPGA controller (PCI-7811R) and LabVIEW FPGA module (version 8.0). A custom built electronics box contains the clock driver circuitry and 16-bit video board for digital conversion of the video signal. Our optical coupling method differs from other EMCCD SPECT systems by using lenses rather than fiber optic bundles for transfer. TC253 characterization tests measured a maximum gain just over $1000\times$, dark current rate of 0.14 e/p/s, read noise of 18.2 e/p, and spurious charge generation of 4 e/p. A light integration intrinsic resolution of 110 μm FWHM was measured. Light integration images of a line phantom using a single pinhole collimator were used for SPECT reconstruction. We found the relative high spurious charge generation and low quantum efficiency of the TC253 made it incapable of photon counting for low energy sources using lens coupling.**

***Index Terms*—SPECT, preclinical, small animal, EMCCD, gamma camera, pinhole collimator, high-resolution, high-sensitivity.**

I. Introduction

OVER the past decade the demand for high-resolution preclinical (small animal) SPECT imaging has greatly increased. This increase is due to the development of new radiolabeled antibodies, receptor ligands, and other radiopharmaceuticals for both imaging and therapy [1]. The availability of genetically modified mice and *in vivo* molecular imaging for studying gene expression and regulation in human disease has also increased the demand for high-resolution SPECT [2]–[5]. One drawback of previous small animal radiopharmaceutical imaging methods, such as autoradiography, was that several animals had to be sacrificed in order to achieve significant statistics since each animal could only be measured once [5]. With the development of high-resolution preclinical SPECT, an animal can be measured several times throughout a study, thereby allowing each animal to act as its own control. This leads to fewer animals needed per study, which helps to reduce the overall cost of the experiment.

The small field of view needed to image animals such as mice and rats ($\approx$10 cm $\times$ 10 cm) allows for the use of pinhole collimation to achieve sub-millimeter resolution ($<$1 mm FWHM). Yet the pinhole diameter required for this resolution severely limits the sensitivity of the device. Several methods for increasing the sensitivity of preclinical SPECT systems are currently being pursued. These methods include using multiple single pinhole detectors [6]–[10], multiplexing several pinholes onto a single detector with either minimal [11], [12] or extensive [13], [14] image overlap on the crystal surface, and even using coded apertures commonly found in gamma-ray astronomy [15], [16]. Existing clinical SPECT systems can be modified with pinhole collimators to achieve adequate resolutions for small animal imaging [6], [13], [17], [18], but compact dedicated preclinical SPECT systems can offer higher resolutions and are small enough to fit on a desktop [7].

Another method to improve sensitivity is to use a charge-coupled device (CCD) for the gamma camera photodetector. The application of CCDs to preclinical SPECT imaging has been previously shown by our group [19]. This research has been greatly accelerated by the recent availability of the electron-multiplying CCD (EMCCD) which was first technically described in 1992 [20] and made commercially available in 2001 [21], [22]. EMCCDs combine the positive aspects of photomultiplier tubes (high-gain leading to a high signal-to-noise ratio, photon counting, and energy discrimination) with the positive aspects of CCDs (high quantum efficiencies over a broad spectral range, high intrinsic resolution, and small form factor) making them well suited for preclinical SPECT applications.

Our goal is the development and evaluation of an EMCCD based small animal SPECT device for murine model studies of human disease. Previous applications of EMCCDs to preclinical SPECT imaging mainly use fiber optic bundles to transfer the light from a micro-columnar CsI(Tl) crystal to the imaging area of the EMCCD [27]–[29], [44]. This requires the bundle to be placed very close to, if not touching, the EMCCD surface which creates mechanical, cooling, and vacuum complications. Our method differs by using monolithic CsI(Tl) crystal and lens coupling for light transfer. With lens coupling, physical contact with the EMCCD is eliminated, although the transfer efficiency is lower compared to fiber coupling. Our approach also differs by using the very low cost Texas Instruments TC253 EMCCD

Manuscript received October 5, 2006; revised April 25, 2007. This work was supported by the DOD BCRP Idea under Award Grant W81-XWH-0410551.

T. C. Soesbe is with the Radiological Sciences Graduate Program at The University of Texas Southwestern Medical Center at Dallas, Dallas, TX 75390 USA (e-mail: todd.soesbe@gmail.com).

M. A. Lewis, E. Richer, N. V. Slavine, and P. P. Antich are with the Division of Advanced Radiological Sciences at The University of Texas Southwestern Medical Center at Dallas, Dallas, TX 75390 USA.

Digital Object Identifier 10.1109/TNS.2007.906408

0018-9499/$25.00 © 2007 IEEE

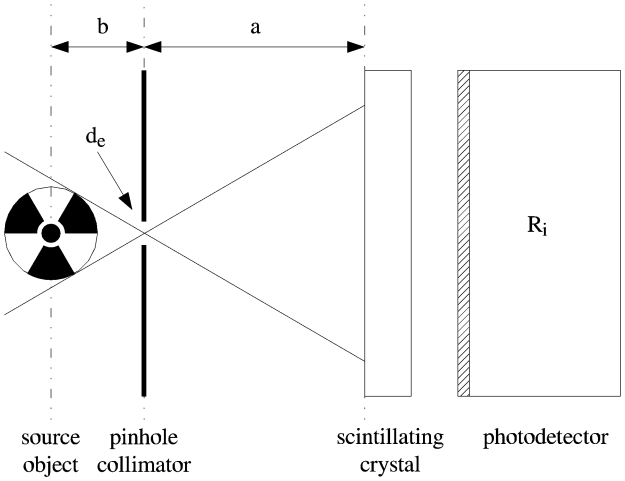

Fig. 1. Schematic showing the geometry of a gamma camera with a single pinhole collimator. When b/a is less than 1, a magnified image of the source object is projected onto the crystal surface.

in our custom designed camera. This paper describes the construction of the camera and electronics, EMCCD noise characterization, gamma camera intrinsic resolution, and SPECT reconstruction based on light integration and lens coupling.

II. Materials and Methods

A. Spatial Resolution

Pinhole collimators provide the best combination of sensitivity and resolution for small subjects that are positioned a short distance from the aperture.
Hal O. Anger, 1967

As seen in the above quote, the advantages of using pinhole collimators to image small source objects that are placed close to the aperture have been known for some 40 years [23]. In fact, the very first gamma camera used pinhole collimation to image the uptake of ^{131}I (364 keV gamma rays) in the human thyroid gland [24]. The setup for a single pinhole gamma camera is shown in Fig. 1 where d_e is the effective diameter of the pinhole aperture, b is the distance from the source to the pinhole, a is the distance from the pinhole to the scintillating crystal, and R_i is the intrinsic spatial resolution of the photodetector and scintillation crystal. The total resolution of the system is given by:

$$R_t = \sqrt{\left(d_e\left(1+\frac{b}{a}\right)\right)^2 + \left(\frac{b}{a}R_i\right)^2} \tag{1}$$

where the first quadratic term under the square root is the geometric resolution (R_g) and the second quadratic term is the effective intrinsic resolution [23]. When b/a is less than 1, a magnified image of the source object is projected onto the crystal surface. This makes the effective intrinsic resolution lower than the intrinsic resolution, which helps to improve the total resolution. Fig. 2(a) shows a plot of R_t, R_g, and $(b/a)R_i$ versus b/a for $d_e = 1.0$ mm and $R_i = 5.0$ mm, which correspond to the typical pinhole size used in small animal imaging and the typical intrinsic resolution of a clinical SPECT gamma camera respectively. For these conditions, it can be seen that the $(b/a)R_i$ term quickly becomes the limiting term for the total resolution as b/a increases. As mentioned previously, clinical SPECT gamma cameras can be used for small animal imaging but require large magnification factors to adequately image mice and rats. From Fig. 2(a) it can be seen that in order to achieve a total resolution of 1.5 mm with a clinical system, a magnification of 5x (or $(b/a) = 0.2$) must be used. This leads to large detector surface areas and volumes. In Fig. 2(b) d_e is again 1.0 mm but R_i has been reduced by an order of magnitude to 0.5 mm. It can be seen that the geometric resolution is now the limiting term for the total resolution, and that a magnification of only 2x (or $(b/a) = 0.5$) is needed to achieve a total resolution of 1.5 mm. This greatly reduces the detector surface area leading to a smaller detector volume, which is more suitable for small animal imaging.

B. Pinhole Sensitivity

With a very low intrinsic resolution as in Fig 2(b), the total resolution of the system can be further improved by reducing d_e. Fig. 2(c) shows a resolution plot for $d_e = 0.5$ mm and $R_i = 0.5$ mm. It can be seen that R_g is still the limiting term for the total resolution, but now a magnification of 2x (or $(b/a) = 0.5$) gives a total resolution of less than 1 mm. Although having submillimeter resolution is attractive, reducing d_e from 1.0 to 0.5 mm severely reduces the sensitivity (counts/second per source activity) of the system. The on-axis geometric efficiency for a pinhole is given by:

$$g = \frac{1}{2}\left(1 - \frac{1}{\sqrt{1+\left(\frac{d_e}{2b}\right)^2}}\right) \tag{2}$$

and represents the fraction of emitted photons that pass through d_e from an isotropic point source located a distance b from the pinhole. For $b \gg d_e$ the square root term in (2) can be binomially expanded to give the approximation:

$$g \approx \frac{{d_e}^2}{16b^2} \tag{3}$$

which is the expression more commonly seen in the literature [7], [17], [23]. When reducing d_e from 1.0 to 0.5 mm, g goes from 0.1% to 0.02% respectively (for $b = 10$ mm). Therefore simply reducing d_e by a factor of two reduces g, and thus the sensitivity, by a factor of five.

One method to increase the sensitivity of pinhole collimation is to simply surround the source object with multiple pinholes. The four main configurations for multiple pinholes are shown schematically in Fig. 3, where the first row is the number of pinholes per collimator, the second row is the pinhole configuration, and the third row represents the projected image onto the crystal surface when imaging a uniform planar source. These options include surrounding the source object with multiple single pinhole detectors (a), multiplexing several pinholes onto one photodetector such that there is no image overlap on the crystal surface (b), multiplexing with image overlap on the crystal surface (c), and using a coded aperture which has severe

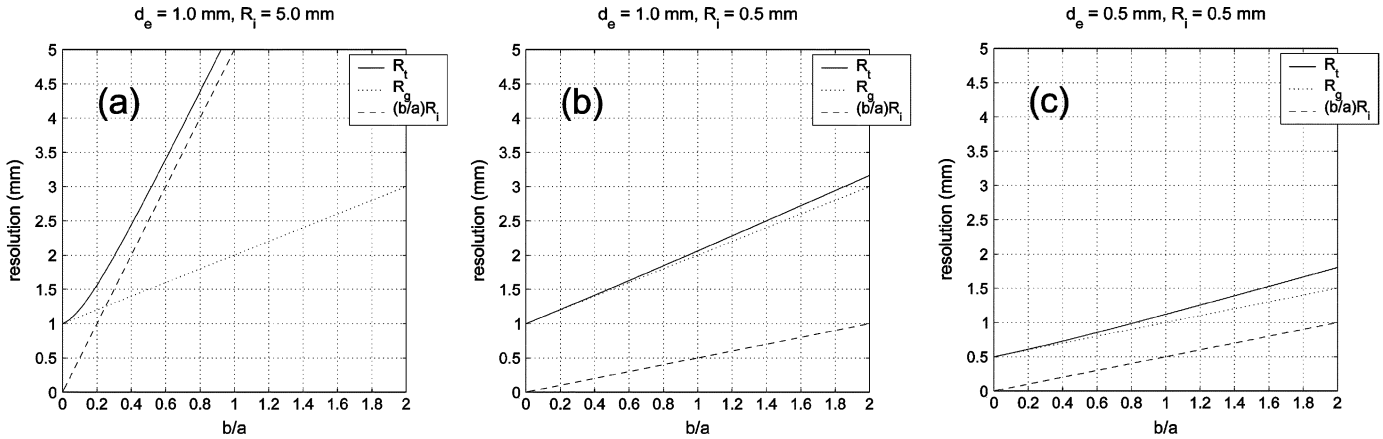

Fig. 2. Plot of R_t, R_g, and $(b/a)R_i$ versus b/a for (a) $d_e = 1.0$ mm and $R_i = 5.0$ mm, (b) $d_e = 1.0$ mm and $R_i = 0.5$ mm, and (c) $d_e = 0.5$ mm and $R_i = 0.5$ mm. $(b/a)R_i$ is the limiting term for (a), while R_g is the limiting term for (b) and (c).

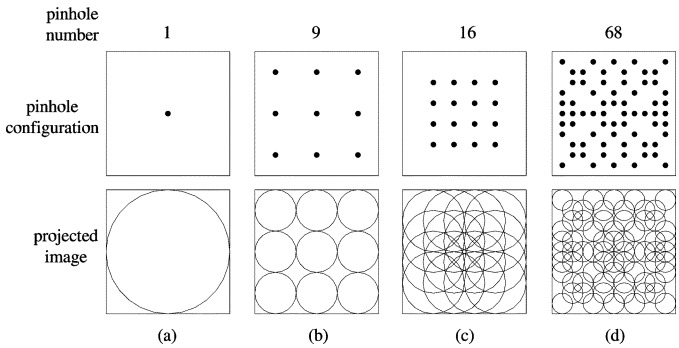

Fig. 3. Schematic showing the four main configurations for multiple pinhole collimation. The sensitivity per collimator increases when moving from left to right.

image overlap (d). Although the sensitivity increases when moving from left to right in Fig. 3, the reconstructed image quality degrades as pinhole projection overlap increases [25], [26]. For this project we intend to improve the sensitivity by multiplexing 9 pinholes onto a single EMCCD gamma camera in a non-overlapping manner and surrounding the source with a ring of up to 12 cameras for a total of over 100 pinholes.

C. EMCCD Sensitivity

The sensitivity of a gamma camera system can be further improved by using an EMCCD to detect the optical photons emerging from the scintillation crystal. EMCCDs have higher quantum efficiencies (up to 95% with back-illumination) and broader spectral responses (400 to 900 nm) when compared to PMTs. Also, intrinsic resolutions less than 100 μm have been shown for EMCCD based gamma cameras [27], [28]. The most important characteristic of an EMCCD is the improved low light level signal-to-noise ratio (SNR) when compared to conventional CCDs. This is achieved by the addition of a second serial register, known as the gain or multiplication register, to the CCD architecture as shown in Fig. 4. Electrons are first captured within the pixel potential wells of the image area, then the entire frame (for example 680 × 500 pixels) is parallel-transferred to the storage area. A single pixel row is then parallel-transferred from the storage area to the serial register. The pixel row in the serial register is then serial-transferred through the multiplication register to the charge-to-voltage output amplifier of the EMCCD. This is done for each row until the entire storage area has been read. The multiplication register differs from the normal serial register by the addition of a third gate known as the charge multiplication gate (CMG) [30]. By making the voltage of the CMG very high (up to 15 VDC) the electrons undergo impact ionization as they move through the multiplication register, which amplifies the electric signal. Although the gain per pixel step is very low (1.01 to 1.018) a multiplication register of 400 pixels in length can allow gains of over 1000× to be reached [31]. Multiplication of the signal in the charge domain before charge-to-voltage conversion effectively reduces the readout noise of the output amplifier to less than 1 electron/pixel. This eliminates the noise floor found in conventional CCDs making EMCCDs sensitive to single electrons.

The total signal noise of an EMCCD is given by:

$$\sigma_t = \sqrt{G^2F^2(P + D + S) + \sigma_r^2} \tag{4}$$

where G is the gain, F is the excess noise (Fano) factor due to the gain process in the multiplication register, and P, D, S, and σ_r are the mean signals (electron/pixel) due to the photon (shot), dark current, spurious charge, and read noises respectively [31], [32]. The dark current noise (D) and the spurious charge noise (S) can be reduced to negligible levels with cooling and proper clocking respectively [33]. Also, for a gain greater than $\approx 10\times$, F approaches $\sqrt{2}$ [34]. Under these conditions the SNR for a EMCCD reduces to:

$$\mathrm{SNR}_{\mathrm{EMCCD}} = \frac{GP}{\sigma_t} = \sqrt{\frac{P}{2}} \tag{5}$$

when $G \gg \sigma_r$. This can be compared to the SNR of a conventional CCD under similar condition given by:

$$\mathrm{SNR}_{\mathrm{CCD}} = \frac{P}{\sqrt{P + \sigma_r^2}} \tag{6}$$

A plot of $\mathrm{SNR}_{\mathrm{EMCCD}}$ and $\mathrm{SNR}_{\mathrm{CCD}}$ versus P is shown in Fig. 5 for a typical read noise ($\sigma_r = 25$ electrons/pixel). It can be seen that while the CCD has a SNR of 1 at 25 electrons/pixel, the EMCCD has a SNR that is 3.5 times higher.

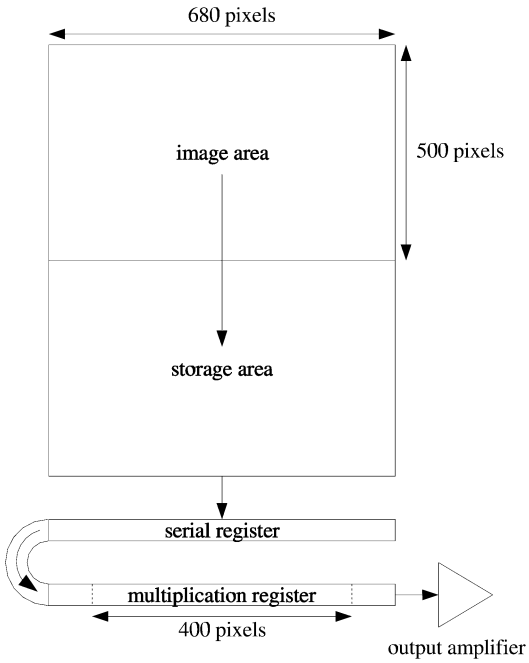

Fig. 4. Schematic showing the architecture of an EMCCD. The electrons are multiplied by impact ionization as they move through the multiplication register before charge-to-voltage conversion in the output amplifier.

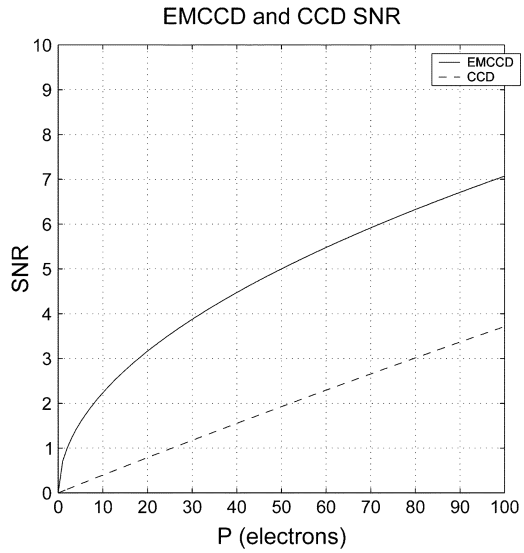

Fig. 5. Plot showing the EMCCD and CCD SNR as a function of electrons/pixel. The EMCCD SNR is much higher for low light level imaging.

D. Camera Prototype

A schematic of the prototype system is shown in Fig 6. The system consists of a PC with a FPGA card, an external electronics box, and the EMCCD camera assembly. The National Instruments PCI-7811R (Xilinx FPGA, 1 million gates, 40 MHz digital rate, 25 ns resolution) produces the clock pulse timing for the EMCCD. These pulses are sent to the driver board inside the external electronics box which converts the TTL pulses to the proper voltages needed to drive the EMCCD. The driving pulses are then sent through an R/C circuit located inside the camera housing for shaping before entering the EMCCD. The video signal from the EMCCD is first sent through a preamp and then through a video board. The video board uses correlated double sampling (CDS) of the video signal to help reduce

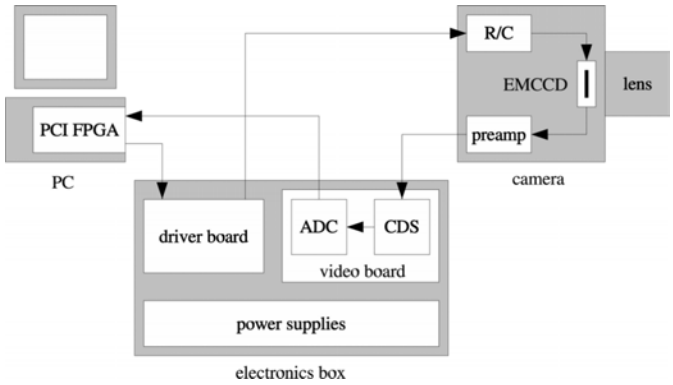

Fig. 6. Schematic showing the setup for the prototype EMCCD camera.

noise before digital conversion in a 16-bit ADC (Analog Devices AD976A, 200 kHz max rate). The digitized video signal is then sent back to the FPGA which uses a DMA FIFO across the PCI bus to store the data on the host computer which is running LabVIEW 8.0.

For the prototype camera we used the Texas Instruments Impactron™ TC253 EMCCD chip (TC253SPD-B0). This front-illuminated chip (35% quantum efficiency at 560 nm) has 7.4 μm square pixels (100% fill factor) in a 680 $\times$ 500, 1/3 inch format. The TC253 has a nominal read noise of 29 electrons/pixel RMS at video rate readout (12.5 MHz clock frequency). It also has low dark current generation ($\approx$0.1 electron/pixel/sec at -40°C) and a built in single stage Peltier element capable of cooling the chip down to -10°C. Fig. 7(a) shows a close up photo of the TC253. The TC253 is mounted onto an Aluminum cold-finger which sits on top of a four-stage Peltier element. Low thermal conductivity wires connect the TC253 to the R/C and preamp circuitry with all camera electronics being contained in the vacuum housing. Fig 7(b) shows an exploded view of the camera assembly showing the lens, shutter, vacuum window, EMCCD housing, and a choice of either air or liquid heat exchanger. A picture of the assembled camera is shown in Fig. 7(c).

III. Results

High quantum efficiency back-illuminated EMCCDs such as the e2v CCD97 currently cost between 6 k to 7 k USD. Off-the-shelf camera systems containing these EMCCDs such as the PhotonMAX 512B cost around 30 k USD. To increase the sensitivity of our preclinical SPECT system, we would like to surround the animal with a ring of multiple cameras. Therefore, in order to reduce the cost per camera to a reasonable level, we have opted to design and build our own. By using the low-cost front-illuminated TC253 EMCCD (500 USD), the PCI-7811R FPGA card with LabVIEW module (2 k USD), and custom built electronics (500 USD), the cost per camera is reduced by an order of magnitude to 3 k USD. Details of the camera system, followed by TC253 noise characterization, and initial light integration imaging results are presented next. Although the system has a gain of over 1000$\times$, low read and dark noises, and good intrinsic resolution, the relative high spurious charge generation and low quantum efficiency of the TC253 make it incapable of photon counting for both ^{99m}Tc and ^{125}I using monolithic CsI(Tl) crystals with lens coupling.

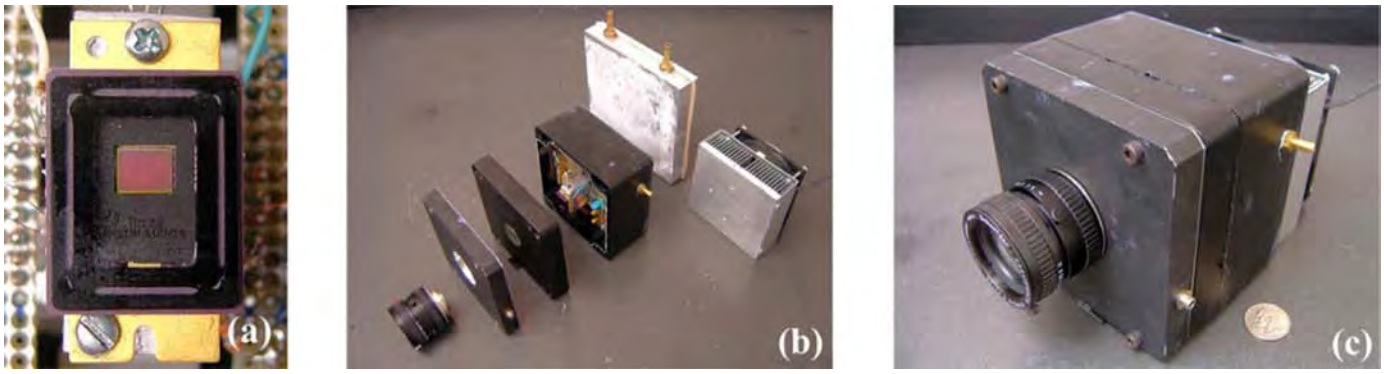

Fig. 7. (a) Photo showing the front face of the Texas Instruments Impactron™ TC253 EMCCD mounted to the Aluminum cold finger. The image area (680 × 500 pixels) measures 5.0 mm × 3.7 mm. (b) An exploded photo of the camera assembly. (c) The assembled camera with air heat exchanger.

A. EMCCD Characterization

Upon completing the prototype camera, we first characterized the EMCCD by measuring the gain, dark current accumulation rate, total read noise, and spurious charge generation to verify that they were within the specified operating range of the TC253. Methods and results for the measurements are described here. All measurements were taken at $-40°$C.

1) Gain: The gain versus positive charge multiplication gate voltage $(+\mathrm{CMG})$ of the TC253 was measured using lens coupling to image a controlled light source. The light source consisted of a 3 mm green LED embedded in a 10 mm × 15 mm Teflon cylinder to create a small diffuse uniform source that was viewed on end. With the EMCCD gain set to 1 ($+\mathrm{CMG} = 7.0$ V), the current to the LED was varied until a SNR of about 5 was achieved for an average of 1000, 33 msec exposures. The difference between the dark reference pixels and peak signal was measured using a line profile of the averaged image. This measurement was repeated as the $+\mathrm{CMG}$ voltage was increased, with the increase between the dark and peak pixels being taken as the gain. A plot of gain versus $+\mathrm{CMG}$ is shown in Fig. 8. It can be seen that the gain starts to increase past 11 V and rises to over 1000 at 14 V.

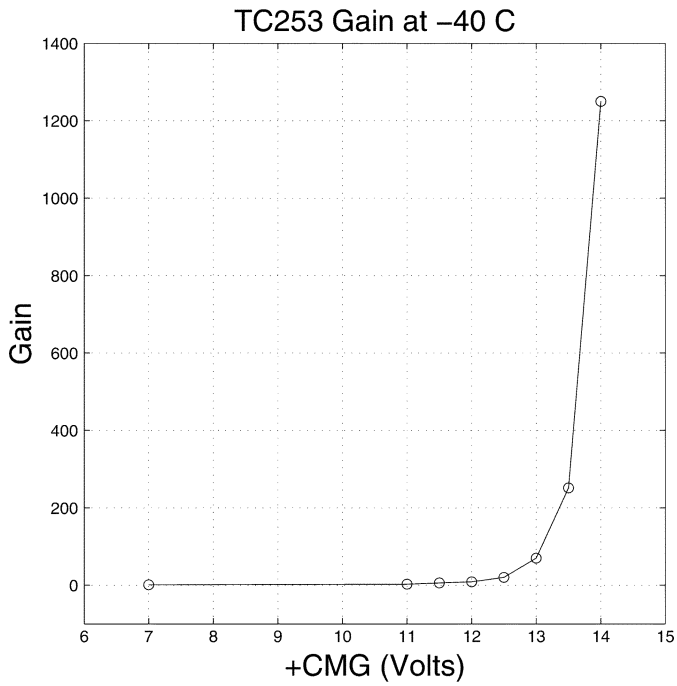

Fig. 8. Plot of EMCCD gain versus positive charge multiplication voltage $(+\mathrm{CMG})$ for the TC253. A gain of over $1000\times$ is reached at 14 V.

2) Dark Current: Dark current arises from thermal generation of electrons within the silicon lattice of the EMCCD. These electrons are captured by the pixel potential wells and contribute to the non-photon related signal noise [see (4)]. Dark current generation is proportional to exposure time, independent of the amount of light incident on the EMCCD, and can be significantly reduced by cooling [35]. The dark current accumulation rate for the TC253 was measured by taking N exposures at a fixed dark exposure time. The mean and standard deviation of the N exposures were then calculated for each pixel. The ensemble average of the pixel means over the active EMCCD area was taken as the dark current count (electrons/pixel), while the ensemble average of the pixel standard deviations was used to calculate the error $(\pm(\sigma_x/\sqrt{N}))$. This measurement was then repeated for several different dark exposure times. For these measurements, the gain was set to 1 and the EMCCD temperature was $-40°$C. A plot of exposure time versus dark current count is shown in Fig. 9. The fitted slope gives 0.14 electrons/pixel/second which agrees with the dark current rate given in the TC253 datasheet.

3) Read Noise: The main source of read noise in the system arises from the charge-to-voltage conversion in the EMCCD output amplifier. Assuming that the spurious charge has been reduced to a negligible level, then for a zero second dark exposure $(P = D = 0)$ at a gain of 1, (4) reduces to:

$$\sigma_t = \sqrt{\sigma_r^2} = \sigma_r \tag{7}$$

so that the total noise is equal to the total read noise. The read noise of the system was measured by taking 1000 zero second exposures at a gain of 1 and calculating the standard deviation for each pixel. The ensemble average of the pixel standard deviations over the active EMCCD area was then multiplied by the system video gain (0.57 electrons/ADU) to give a read noise of 18.2 electrons/pixel RMS. The measured read noise was lower than the read noise stated in the TC253 datasheet (29 electrons/pixel RMS) due to the 200 kHz maximum readout rate of the current ADC. Although fine for initial testing, a faster

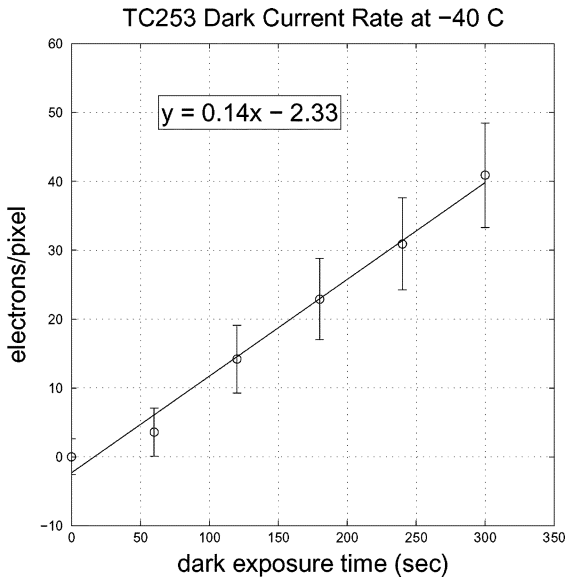

Fig. 9. Plot of dark current count (electrons/pixel) versus dark exposure time. The fitted slope gives the dark current accumulation rate for the EMCCD at $-40°$C.

ADC will be needed to achieve video rate readout (12.5 MHz). This will increase the readout noise which is proportional to the readout speed.

4) Spurious Charge: Along with dark current, non-photon related electrons known as spurious charge (or clock induced charge) can be generated during the readout of the EMCCD. Spurious charge arises from the rapid inversion of the clocking potentials and tends to increase with faster readout speeds and lower temperatures [35]. Methods to reduce spurious charge include using a slow parallel-transfer from the image area to the storage area, setting the rise and fall times of the clocking pulses to about 200 ns, and using the minimum clocking potentials necessary for efficient charge transfer [28], [33]. Of these three methods, the greatest observed reduction in spurious charge for the TC253 was seen by minimizing the clocking potentials [36].

Spurious charge generation as a function of $+\mathrm{CMG}$ was measured for the TC253 by taking 100 zero second dark exposures for a fixed $+\mathrm{CMG}$ voltage. The ensemble average of the standard deviations for each pixel was then calculated and taken as the total noise (σ_t). For a zero second dark exposure $(P = D = 0)$ (4) can be rewritten as:

$$S = \frac{\sigma_t^2 + \sigma_r^2}{F^2 G^2} \tag{8}$$

By using σ_t from before, σ_r and G from the previous read noise and gain measurements, and knowing that $F \rightarrow \sqrt{2}$ at high gain, the spurious charge generation was calculated to be 3 to 4 electrons/pixel at gains from $500\times$ to $1000\times$. This spurious charge generation could not be further reduced by the minimizing methods listed above and appears to be an inherent property of the TC253, largely caused by the use of virtual-phase electrode technology [22]. This spurious charge generation is therefore the true noise floor for the TC253 chip making it incapable of single photoelectron sensitivity.

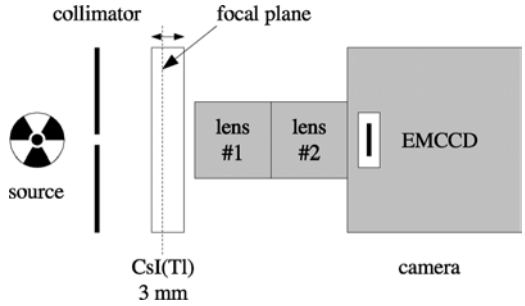

Fig. 10. Schematic of the EMCCD SPECT setup. Two lenses are used to improve the optical transfer of the scintillation light to the EMCCD. The lens focal plane can be moved through the crystal.

Consequences of this measurement are further discussed in Section IV. As a comparison, this same measurement was done with a high-quality commercially available EMCCD camera (Princeton Instruments/Acton PhotonMAX 512B with the e2v CCD97 EMCCD) which yielded a spurious charge generation of less than 0.01 electrons/pixel.

B. Intrinsic Resolution

A schematic of the lens-coupled SPECT setup is shown in Fig 10. Two 1-inch format lenses (Schneider Xenon 0.95/25) were coupled front-to-front in order to improve the optical transfer to the EMCCD. Both lenses had an f-stop of 0.95 with the front lens focus set to infinity and the rear lens focus being adjustable. A 3 mm thick monolithic CsI(Tl) crystal was then placed 5 to 10 mm in front of the lenses so that the shallow focal plane (less than 1 mm deep) could be moved through the crystal. The two coupled lenses image a field of view (FOV) on the crystal that is approximately the same size as the image area of the EMCCD (≈ 5 mm $\times$ 5 mm). When compared to a single lens imaging the same FOV, we found the optical transfer when using two lenses to be improved by a factor of two.

The intrinsic resolution (R_i) for the above setup was measured using a 30 μm slit Tungsten collimator and a $^{99m}\mathrm{Tc}$ source. The activity viewed by the slit was approximately 50 μCi (1.9 MBq). The line spread function for a 5 minute exposure with the gain set to $200\times$ was acquired. The acquired image and 1 mm wide line profile (taken perpendicular to the slit) are shown in Fig 11. Fitting the line spread function profile with a Gaussian distribution gave a FWHM of 110 μm which was taken as the intrinsic resolution.

C. SPECT Images

For SPECT imaging, the Tungsten slit collimator was replaced with a single pinhole Lead collimator. The pinhole diameter was 0.5 mm with an aperture angle of 90 degrees. A small glass capillary tube was filled with aqueous $^{99m}\mathrm{Tc}$ solution, mounted to a step motor, and placed in front of the pinhole. The 3 cm long capillary had an outer diameter of 1.5 mm, an inner diameter of 0.8 mm, and a linear activity of 10 μCi/mm (0.37 MBq/mm). Projection data were then taken as the phantom was rotated (20 projections, 18° step) with a 3 minute exposure time for each projection. The EMCCD gain was set to $1000\times$ at a temperature of $-50°$C. Fig. 12 shows a sample projection of

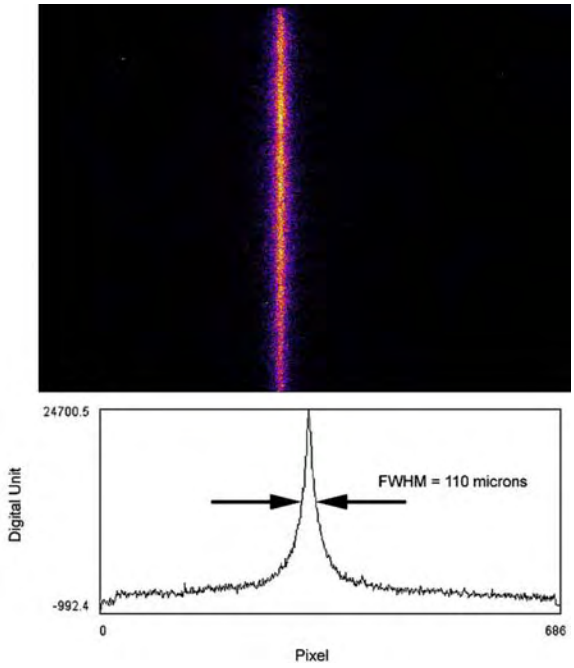

Fig. 11. Image and line profile produced by a 30 μm slit collimator and ^{99m}Tc source. The exposure time was 5 minutes with a gain of $200\times$.

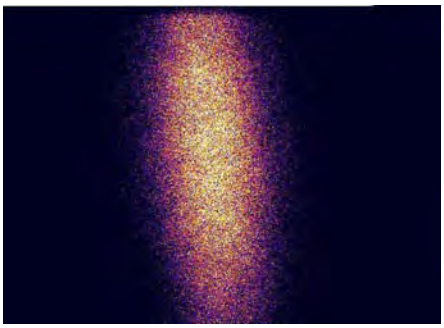

Fig. 12. Pinhole projection image of a ^{99m}Tc filled line phantom. The subject FOV measures 6.0 mm × 4.5 mm with an exposure time of 3 minutes.

the line source, with the subject FOV measuring 6.0 mm × 4.5 mm.

Image reconstruction was based on the Maximum Likelihood method (MLEM) [37] which was improved with the list-mode high resolution algorithm for system matrix modeling (MLSM) [38], [39]. A convolution procedure based on the discrete Fast Fourier Transform (FFT) was used for resolution modeling. If photon scattering is neglected, the blurring component of the matrices which account for the finite resolution effects can be represented as a set of shift-invariant kernels (details given in [39], [40]). Fig. 13(a) shows a transverse slice of the MLSM reconstruction for the line phantom. The total FOV (20 mm^3) was subdivided into 0.25 mm^3 voxels. Approximately 300 000 events were reconstructed into the voxel array. A Gaussian function (0.4 mm kernel) was used to model the resolution during the 10 iterations. The FWHM of the Gaussian fitted line profile in Fig. 13(b) measures 0.96 mm. The slight increase in the reconstructed diameter is due to the total resolution of the setup being limited by the geometric resolution (R_g) which was ≈1 mm.

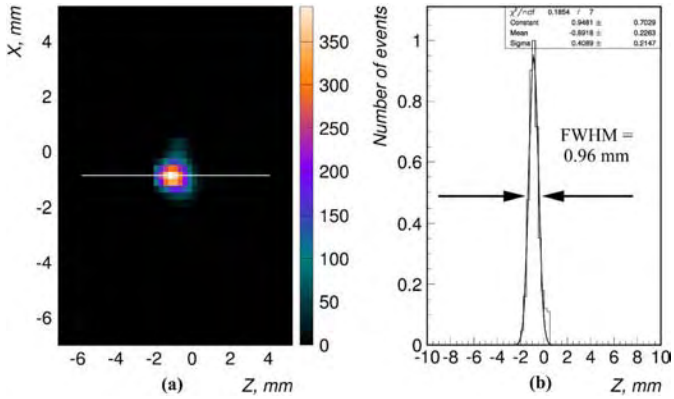

Fig. 13. SPECT reconstruction of the line source (a) with Gaussian fitted line profile (b).

IV. Conclusion and Discussion

A. Summary

A cost effective prototype EMCCD based gamma camera has been developed and evaluated for use in preclinical SPECT imaging. A four stage Peltier and liquid heat exchanger was used to cool the EMCCD down to $-50°$C. Dual f/0.95 lens coupling was used to image the scintillation light from a 3 mm thick monolithic CsI(Tl) crystal. A gain of over $1000\times$ was measured for the TC253 EMCCD. The dark current accumulation rate and read noise were within the specified operating range for a temperature of $-40°$C and readout rate of 200 kHz. A spurious charge generation of 3 to 4 electrons/pixel was measured at high gain values. This intrinsic spurious charge could not be further reduced using established minimizing techniques and represents the noise floor for the TC253. An intrinsic resolution of 110 μm FWHM was measured using a 30 μm slit collimator and ^{99m}Tc source. Single pinhole collimation was used to take SPECT images of a small ^{99m}Tc line phantom. The MLEM reconstructed source size was slightly larger than the true source size due to the geometric resolution of the setup.

B. Conclusion

Although the prototype EMCCD gamma camera was capable of SPECT imaging using light integration, it was unable to perform photon counting for ^{99m}Tc and ^{125}I with the current optical transfer method. This can be explained by estimating the number of electrons produced in the TC253 per CsI(Tl) scintillation event. The luminosity of CsI(Tl) is 54 photons/keV with a peak wavelength of 560 nm. Approximately 10% of these scintillation photons will escape the crystal via the non-internally reflected light cone [41]. Upper limits for dual lens optical coupling efficiency (with an object to image ratio of 1:1) have been estimated to be ≈5% [42], [43], and the quantum efficiency of the TC253 is 35% at 560 nm. This gives $(140 \times 54 \times 0.1 \times 0.05 \times 0.35) = 13$ electrons/event for ^{99m}Tc and $(27 \times 54 \times 0.1 \times 0.05 \times 0.35) = 3$ electrons/event for ^{125}I. When these signals are spread over a 3×3 pixel area they are easily lost within the 3 to 4 electrons/pixel spurious charge noise of the TC253. Single photoelectric events were observed using a higher energy ^{137}Cs (662 keV) source where the increased

number of scintillation photons results is more than 3 to 4 electrons/pixel/event. Also, when the same scintillation crystal and lens setup were used with the PhotonMAX 512B camera (e2v CCD97 EMCCD, 95% quantum efficiency at 560 nm) single photoelectric events were easily observed for both ^{99m}Tc and ^{125}I sources. These results are to be presented in a subsequent publication.

C. Further Work

One possible solution to allow photon counting with the TC253 is to improve the optical transfer of the scintillation photons to the EMCCD by using a micro-columnar CsI(Tl) crystal with a fiber-optic bundle instead of monolithic crystal with lens coupling. Fiber-optic coupling offers an order of magnitude improvement in the coupling efficiency (>50% with a 1:1 image to object ratio) compared to lens coupling [41]. This method of photon counting has been previously established [27], [28], [44] and would allow for energy windowing, a higher intrinsic resolution, and a larger crystal FOV to be observed. Another solution could be to change from the Texas Instruments TC253 to the TC247 EMCCD. The TC247 has a higher quantum efficiency than the TC253 (50% versus 35% at 560 nm) and does not appear to be noise limited by inherent spurious charge generation [45]. Although the TC247 has a larger pixel size than the TC253 (10 μm $\times$ 10 μm versus 7.4 μm $\times$ 7.4 μm) it does not have a 100% fill factor which could effect the sensitivity. These two options will be explored with the goal of making our EMCCD gamma camera capable of both photon counting and energy discrimination for ^{99m}Tc and ^{125}I sources.

D. Discussion

EMCCD images formed by counting individual photoelectric events within the scintillation crystal have improved intrinsic resolutions when compared to light integration images [27]. Although resolutions of less than 100 μm have been measured, it is not fully understood how to take advantage of this metric in preclinical SPECT imaging. For example, when using a 0.5 mm pinhole collimator with an intrinsic resolution of 100 μm, the total spatial resolution is still limited by the geometric resolution of the pinhole (see (1)). The total resolution can be improved by reducing the pinhole diameter, but this has negative effects on the sensitivity as previously shown. Fig. 14 shows a resolution plot for $R_i = d_e = 100$ μm. It can been seen that for $b/a = 1$ (no image magnification) a total resolution of about 225 μm is achieved. It can also be seen that a total resolution of less than 1 mm is still reached with $b/a = 5$, where the projected image on the crystal surface is *smaller* than the subject object. This means that for a subject FOV of 10 mm $\times$ 10 mm, only 2 mm $\times$ 2 mm is needed on the crystal surface. Therefore, one hundred 0.1 mm diameter pinholes could be multiplexed onto a 20 mm $\times$ 20 mm collimator with no image overlap on the crystal surface. Yet the combined sensitivity of these one hundred pinholes would be equivalent to a single 1.0 mm diameter pinhole. It is possible that micro-channel parallel hole [46], [47] or multiple slit [48] collimators might better use the high intrinsic resolution of an EMCCD based gamma camera to find a good balance between sensitivity and resolution in preclinical SPECT imaging. Also, a recent study indicates that advantages in both total resolution and system size can be achieved using EMCCD photodetectors [49].

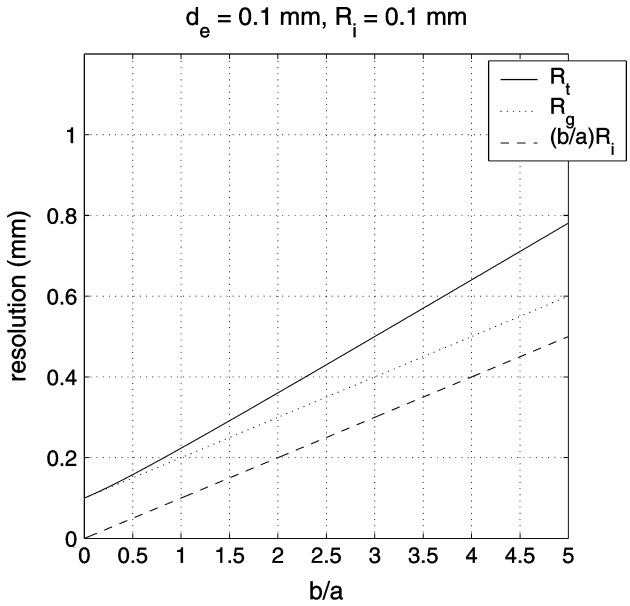

Fig. 14. Plot of R_t, R_g, and $(b/a)R_i$ versus b/a for $d_e = 0.1$ mm and $R_i = 0.1$ mm. It can be seen that a total resolution of less than 1.0 mm is still achieved at $b/a = 5$.

ACKNOWLEDGMENT

The authors would like to thank Dr. Padmakar Kulkarni, Billy Smith, and Trung Nguyen of the Division of Advanced Radiological Sciences at the University of Texas Southwestern Medical Center at Dallas, and Dr. Freek Beekman and Jan Heemskerk of the Physics of Molecular Imaging and Nuclear Medicine group at the University of Utrecht for their technical assistance with this work.

REFERENCES

[1] D. A. Weber, M. Ivanovic, D. Franceschi, S.-E. Strand, K. Erlandsson, M. Franceschi, H. L. Atkins, J. A. Coderre, H. Susskind, T. Button, and K. Ljunggren, "Pinhole SPECT: An approach to in vivo high resolution SPECT imaging in small laboratory animals," *J. Nucl. Med.*, vol. 35, pp. 342–348, Feb. 1994.

[2] S. R. Cherry, "In vivo molecular and genomic imaging: New challenges for imaging physics," *Phys. Med. Biol.*, vol. 49, pp. R13–R48, Jan. 2004.

[3] R. Weissleder and U. Mahmood, "Molecular imaging," *Radiol.*, vol. 219, pp. 316–333, May 2001.

[4] F. J. Beekman, D. P. McElroy, F. Berger, S. S. Gambhir, E. J. Hoffman, and S. R. Cherry, "Towards in vivo nuclear microscopy: Iodine-125 imaging in mice using micro-pinholes," *Eur. J. Nucl. Med.*, vol. 29, pp. 933–938, Jul. 2002.

[5] L. R. MacDonald, B. E. Patt, J. S. Iwanczyk, B. M. W. Tsui, Y. Wang, E. C. Frey, D. E. Wessell, P. D. Acton, and H. F. Kung, "Pinhole SPECT of mice using the lumaGEM gamma camera," *IEEE Trans. Nucl. Sci.*, vol. 48, no. 3, pt. 2, pp. 830–836, Jun. 2001.

[6] K. Ishizu, T. Mukai, Y. Yonekura, M. Pagani, T. Fujita, Y. Magata, S. Nishizawa, N. Tamaki, H. Shibasaki, and J. Konishi, "Ultra-high resolution SPECT system using four pinhole collimators for small animal studies," *J. Nucl. Med.*, vol. 36, pp. 2282–2206, Dec. 1995.

[7] D. P. McElroy, L. R. MacDonald, F. J. Beekman, Y. Wang, B. E. Patt, J. S. Iwanczyk, B. M. W. Tsui, and E. J. Hoffman, "Performance evaluation of A-SPECT: A high resolution desktop pinhole SPECT system for imaging small animals," *IEEE Trans. Nucl. Sci.*, vol. 49, no. 5, pt. 1, pp. 2139–2147, Oct. 2002.

[8] H. Kim, L. R. Furenlid, M. J. Crawford, D. W. Wilson, H. B. Barber, T. E. Peterson, W. C. J. Hunter, Z. L. Liu, J. M. Woolfenden, and H. H. Barrett, "SemiSPECT: A small-animal single-photon emission computed tomography (SPECT) imager based on eight cadmium zinc telluride (CZT) detector arrays," *Med. Phys.*, vol. 33, pp. 465–474, Feb. 2006.

[9] M. Singh and E. Mumcuoglu, "Design of a CZT based BreastSPECT system," *IEEE Trans. Nucl. Sci.*, vol. 45, no. 6, pp. 1158–1165, Jun. 1998.

[10] L. R. Furenlid, D. W. Wilson, Y. C. Chen, H. Kim, P. J. Pietraski, M. J. Crawford, and H. H. Barrett, "FastSPECT II: A second-generation high-resolution dynamic SPECT imager," *IEEE Trans. Nucl. Sci.*, vol. 51, no. 3, pp. 631–635, Jun. 2004.

[11] F. J. Beekman, A. P. Colijn, B. Vastenhouw, V. M. Wiegant, and M. A. F. M. Gerrits, "High-resolution emission tomography of small laboratory animals: Physics and gamma-astronomy meet molecular biology," *Nucl. Instrum. Methods A*, vol. 509, pp. 229–234, Aug. 2003.

[12] F. J. Beekman and B. Vastenhouw, "Design and simulation of a high-resolution stationary SPECT system for small animals," *Phys. Med. Biol.*, vol. 49, pp. 4579–4592, Sep. 2004.

[13] N. U. Schramm, G. Ebel, U. Engeland, T. Schurrat, M. Béhé, and T. M. Behr, "High-resolution SPECT using multipinhole collimation," *IEEE Trans. Nucl. Sci.*, vol. 50, no. 3, pp. 315–320, Jun. 2003.

[14] S. Staelens, K. Vunckx, J. De Beenhouwer, F. Beekman, Y. D'Asslelr, J. Nuyts, and I. Lemahieu, "GATE simulations for optimization of pinhole imaging," *Nucl. Instrum. Methods A*, vol. 569, pp. 359–363, Sep. 2006.

[15] R. Accorsi, F. Gasparini, and R. C. Lanza, "A coded aperture for high-resolution nuclear medicine planar imaging with a conventional Anger camera: experimental results," *IEEE Trans. Nucl. Sci.*, vol. 48, no. 6, pp. 2411–2417, Dec. 2001.

[16] S. R. Meikle, P. Kench, A. G. Weisenberger, R. Wojcik, M. F. Smith, S. Majewski, S. Eberl, R. R. Fulton, A. B. Rosenfeld, and M. J. Fulham, "A prototype coded aperture detector for small animal SPECT," *IEEE Trans. Nucl. Sci.*, vol. 49, no. 5, pt. 1, pp. 2167–2171, Oct. 2002.

[17] R. J. Jaszczak, J. Li, H. Wang, M. R. Zalutsky, and R. E. Coleman, "Pinhole collimation for ultra-high-resolution, small-field-of-view SPECT," *Phys. Med. Biol.*, vol. 39, pp. 425–437, Mar. 1994.

[18] F. J. Beekman, F. van der Have, B. Vastenhouw, A. J. A. van der Linden, P. P. van Rijk, J. P. H. Burbach, and M. P. Smidt, "U-SPECT-I: A novel system for submillimeter-resolution tomography with radiolabeled molecules in mice," *J. Nucl. Med.*, vol. 46, pp. 1194–1200, Jul. 2005.

[19] E. Richer, M. A. Lewis, B. Smith, X. Li, S. Seliounine, R. P. Mason, and P. P. Antich, , M. A. Kupinski and H. H. Barrett, Eds., "Comparison of CsI(Tl) and scintillating plastic in a multi-pinhole/CCD-based gamma camera for small-animal low-energy SPECT," in *Small Animal SPECT Imaging*, 1st ed. New York: Springer, 2005, pp. 189–194.

[20] J. Hynecek, "CCM-a new low-noise charge carrier multiplier suitable for detection of charge in small pixel CCD image sensors," *IEEE Trans. Electron Devices*, vol. 39, no. 8, pp. 1972–1975, Aug. 1992.

[21] J. Hynecek, "Impactron-a new solid state image intensifier," *IEEE Trans. Electron Devices*, vol. 48, no. 10, pp. 2238–2241, Oct. 2001.

[22] P. Jerram, P. Pool, R. Bell, D. Burt, S. Bowring, S. Spencer, M. Hazelwood, I. Moody, N. Catlett, and P. Heyes, "The L3CCD: Low light imaging without the need for an intensifier," in *Proc. SPIE*, 2001, vol. 4306, pp. 178–186.

[23] H. O. Anger, , G. J. Hine, Ed., "Radioisotope cameras," in *Instrumentation in Nuclear Medicine*, 1st ed. New York: Academic Press, 1967, vol. 1, pp. 485–553.

[24] H. O. Anger, "Scintillation camera," *Rev. Sci. Instr.*, vol. 29, pp. 27–33, Jan. 1958.

[25] K. Vunckx and J. Nuyts, "Effect of overlapping projections on reconstruction image quality in multiple pinhole SPECT," in *Proc. IEEE Nuclear Science Symp. Conf. Rec.*, San Diego, CA, 2006, pp. M11–412.

[26] S. P. Mok, Y. Wang, and B. M. W. Tsui, "Quantification of the multiplexing effect in multiple-pinhole small animal SPECT," in *Proc. IEEE Nuclear Science Symp. Conf. Rec.*, San Diego, CA, 2006, pp. M07–1.

[27] F. J. Beekman and G. A. de Vree, "Photon-counting versus an integrating CCD-based gamma camera: Important consequences for spatial resolution," *Phys. Med. Biol.*, vol. 50, pp. N109–N119, May 2005.

[28] G. A. de Vree, A. H. Westra, I. Moody, F. van der Have, K. M. Ligtvoet, and F. J. Beekman, "Photon-counting gamma camera based on an electron-multiplying CCD," *IEEE Trans. Nucl. Sci.*, vol. 52, no. 3, pt. 1, pp. 580–588, Jun. 2005.

[29] L. J. Meng, "An intensified EMCCD camera for low energy gamma ray imaging application," *IEEE Trans. Nucl. Sci.*, vol. 53, no. 4, pt. 2, pp. 2376–2384, Aug. 2006.

[30] J. Hynecek and T. Nishiwaki, "Excess noise and other important characteristics of low light level imaging using charge multiplying CCDs," *IEEE Trans. Electron Devices*, vol. 50, no. 1, pp. 239–245, Jan. 2003.

[31] On-Chip Multiplication Gain Roper Scientific Inc., Tucson, AZ, Tech. Note 14, 2003, Corporate Publication.

[32] The Use of Multiplication Gain in L3Vision™ Electron Multiplying CCD Sensors e2V Technologies Limited, Essex, U.K., Low-Light Tech. Note 2, Jul. 2003, Corporate Publ..

[33] Dark Signal and Clock-Induced Charge in L3Vision™ CCD Sensors e2V Technologies Limited, Essex, U.K., Low-Light Tech. Note 4, Jul. 2004, Corporate Publ..

[34] M. S. Robbins and B. J. Hadwen, "The noise performance of electron multiplying charge-coupled devices," *IEEE Trans. Electron Devices*, vol. 50, no. 5, pp. 1227–1232, May 2003.

[35] J. R. Janesick, *Scientific Charge-Coupled Devices.*. Bellingham, WA: SPIE, 2001, pp. 605–654.

[36] Designer's Guide for the TC253SPD/TX253SPD Impactron CCD Texas Instruments Inc., Dallas, TX, USA, Appl. Note, Mar. 2003, Corporate Publ..

[37] L. A. Shepp and Y. Vardi, "Maximum likelihood reconstruction for emission tomography," *IEEE Trans. Med. Imag.*, vol. 49, pp. 113–122, Oct. 1982.

[38] A. J. Reader, S. Ally, F. Bakatselos, R. Manavaki, R. J. Walledge, A. P. Jeavons, P. J. Julyan, S. Zhao, D. L. Hastings, and J. Zweit, "One-pass list-mode EM algorithm for high resolution 3-D PET image reconstruction into large arrays," *IEEE Trans. Nucl. Sci.*, vol. 49, no. 3, pt. 1, pp. 693–699, Jun. 2002.

[39] P. Antich, R. Parkey, S. Seliounine, N. Slavine, E. Tsyganov, and A. Zinchenko, "Application of expectation maximization algorithms for image resolution improvement in a small animal PET system," *IEEE Trans. Nucl. Sci.*, vol. 52, no. 3, pt. 1, pp. 684–690, Jun. 2005.

[40] E. Tsyganov, J. Anderson, G. Arbique, A. Constantinescu, M. Jennewein, P. V. Kulkarni, R. P. Mason, R. W. McColl, O. K. Oz, R. W. Parkey, E. Richer, F. Rosch, S. Y. Seliounine, N. V. Slavine, S. C. Srivastava, P. E. Thorpe, A. I. Zinchenko, and P. P. Antich, "UTSW small animal positron emission imager," *IEEE Trans. Nucl. Sci.*, vol. 53, no. 5, pt. 1, pp. 243–254, Oct. 2006.

[41] S. M. Gruner, M. W. Tate, and E. F. Eikenberry, "Charge-coupled device area x-ray detectors," *Rev. Sci. Instrum.*, vol. 73, pp. 2815–2842, Aug. 2002.

[42] S. J. Taylor, H. H. Barrett, and K. Zinn, "Small animal SPECT using a lens-coupled CCD camera," presented at the Academy of Molecular Imaging Conf., Orlando, FL, Mar. 2004.

[43] H. Liu, A. Karellas, L. J. Harris, and C. J. D'Orsi, "Methods to calculate the lens efficiency in optically coupled CCD x-ray imaging systems," *Med. Phys.*, vol. 21, pp. 1193–1195, July 1994.

[44] V. V. Nagarkar, I. Shestakova, V. Gaysinskiy, B. Singh, B. W. Miller, and H. B. Barber, "Fast X-ray/γ-ray imaging using electron multiplying CCD-based detector," *Nucl. Instrum. Methods A*, vol. 563, pp. 45–48, Feb. 2006.

[45] J. Hynecek, 2005, personal correspondence.

[46] G. A. Kastis, L. R. Furenlid, D. W. Wilson, T. E. Peterson, H. B. Barber, and H. H. Barrett, "Compact CT/SPECT small-animal imaging system," *IEEE Trans. Nucl. Sci.*, vol. 51, no. 1, pt. 1, pp. 63–67, Feb. 2004.

[47] E. L. Bradley, J. Celle, S. Majewski, V. Popov, J. Qian, M. S. Saha, M. F. Smith, A. G. Weisenberger, and R. E. Welsh, "A compact gamma camera for biological imaging," *IEEE Trans. Nucl. Sci.*, vol. 53, no. 1, pt. 1, pp. 59–65, Feb. 2006.

[48] Q. Huang and G. S. L. Zeng, "An analytical algorithm for skew-slit imaging geometry with nonuniform attenuation correction," *Med. Phys.*, vol. 33, pp. 997–1004, Apr. 2006.

[49] M. C. M. Rentmeester, F. van der Have, and F. J. Beekman, "Optimizing multiple-pinhole SPECT geometries using an analytical model," *Phys. Med. Biol.*, vol. 52, pp. 2567–2581, Apr. 2006.

Scatter Correction for Low-Energy Small Animal SPECT using Optical Surface Topography in a Dual Modality Imaging System

Matthew A. Lewis, Nikolai V. Slavine, Todd Soesbe,
Edmond Richer, Peter P. Antich
Advanced Radiological Sciences
UT Southwestern Medical Center at Dallas

10 March 2006
2nd Bi-Annual Workshop on Small-Animal SPECT

Supported in part by DoD BCRP W81XWH-04-1-0551

Dual Optical/SPECT Imaging

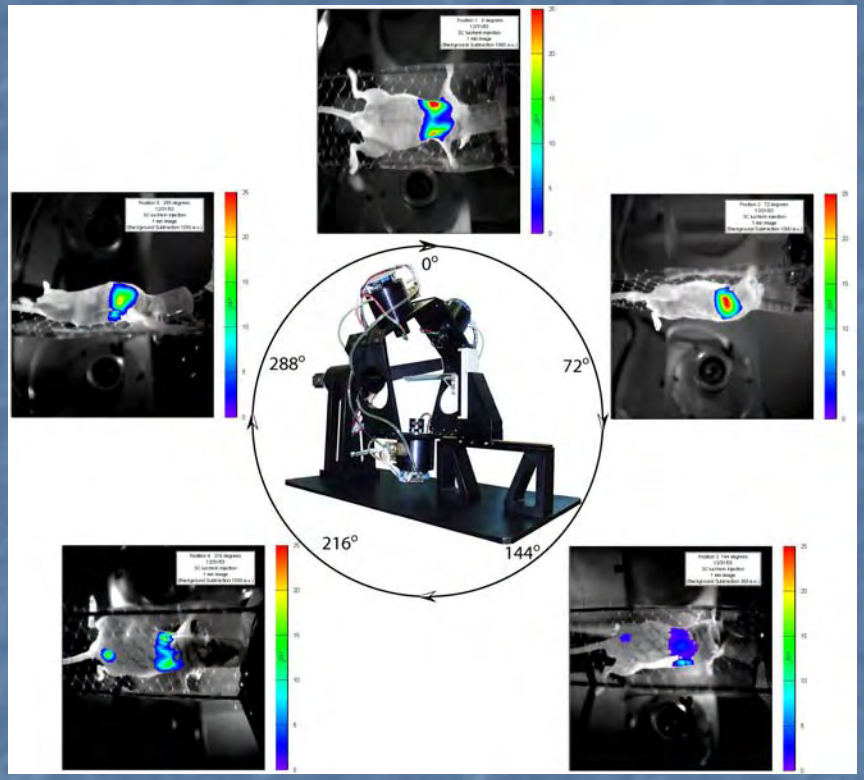

- sensitive back-illuminated CCD cameras used for bioluminescence imaging (BLI)
- with addition of scintillator+collimator, CCD-based gamma camera (emCCDs for photon counting)

I-125 Photons

mode	energy (keV)	photons per 100 decays	relative proportion (%)
$XK\alpha_1$	27.4726	74.0	50.6
$XK\alpha_2$	27.202	39.7	27.2
$XK'\beta_1$	30.9446 30.996 31.223 31.241	21.4	14.5
$XK'\beta_2$	31.7008 31.774 31.8116	4.59	3.1
γ	35.4919	6.67	4.6

Table 1: Photon Emissions

- 130-140 photons greater than 27 keV per 100 disintegrations.
- Are they usable?

Iodine-125 and Scatter

- ‘isosbestic’ point for Compton vs. P.E. in H2O at 28.2 keV – if dimensions of object are consistent with mean free path, then detected photons will have most likely scattered only once.
- ‘isosbestic’ point for Compton vs. coherent in H2O at 13 keV.
- energy loss through incoherent scattering < %5, so energy discrimination becomes problematic.

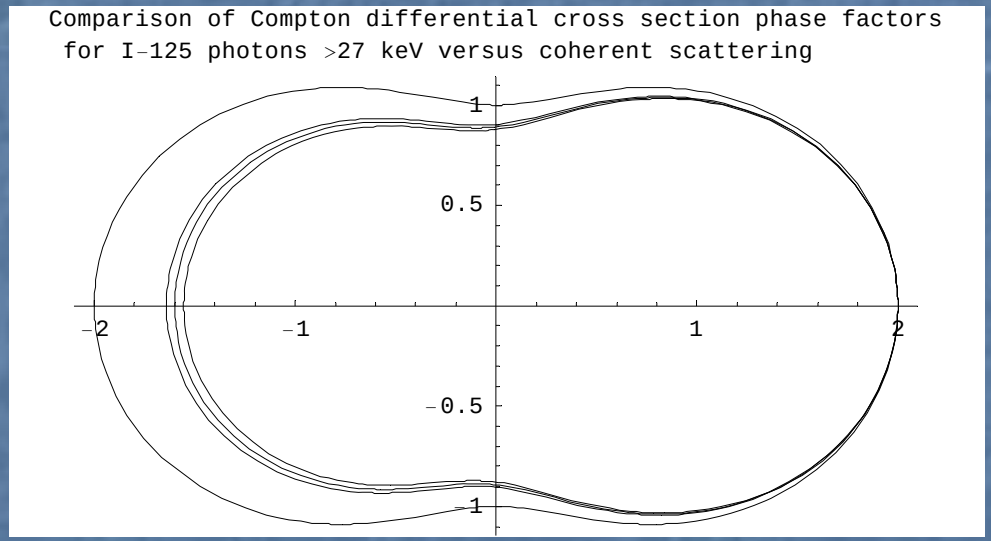

• Below 30 keV, Compton scatter is asymptotically approaching properties of coherent scattering.

I-125 and scatter

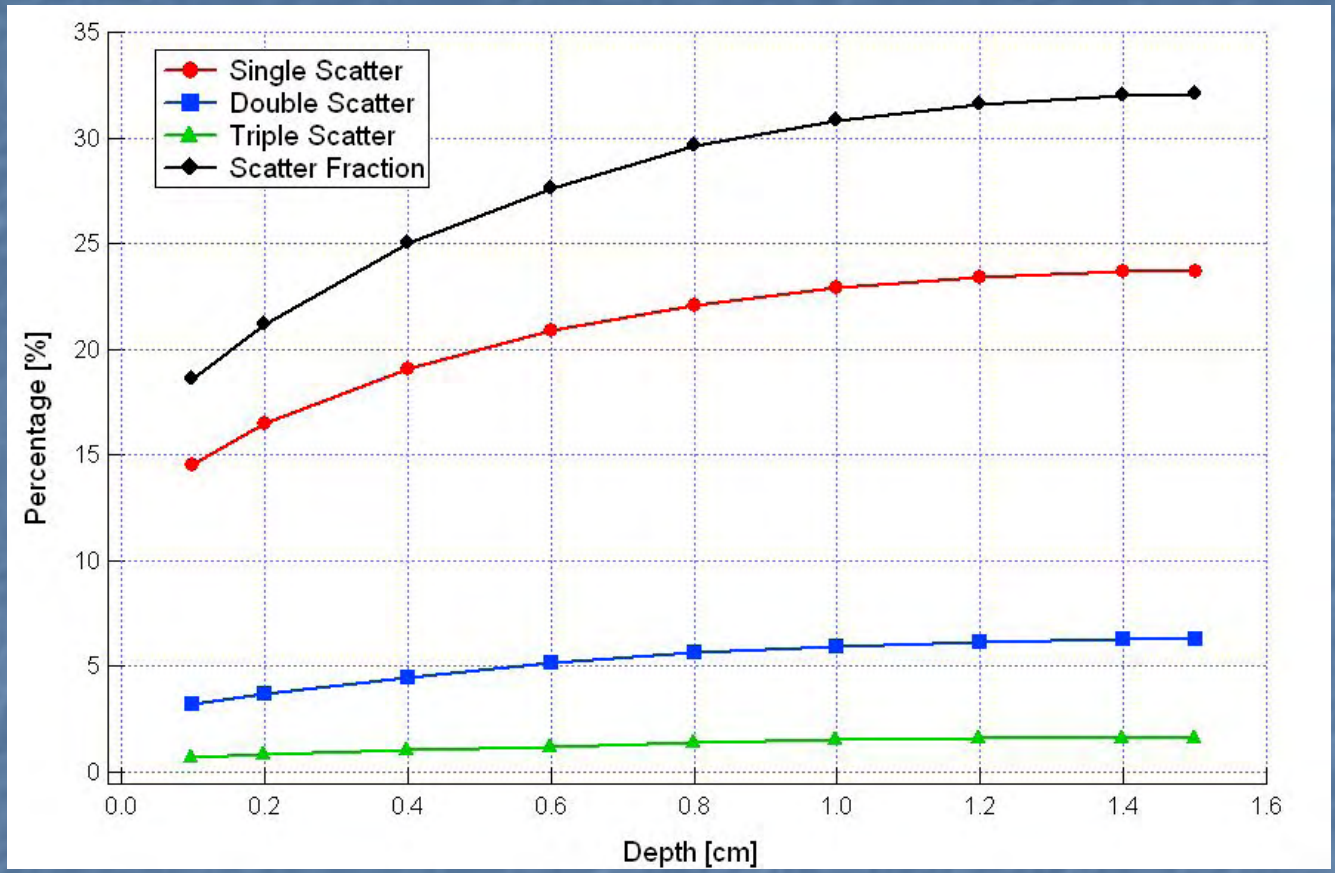

- Single scatter four times more likely than double scatter.
- Nine times more likely for sources in mouse head.
- Compton scatter three times more likely than coherent scattering.

Image Reconstruction

Bioluminescence tomography

Surface topography generation

Place projection data on boundary

Image reconstruction

Slavine et al. “Iterative reconstruction method for light emitting sources based on the diffusion equation.” Med. Phys. 33(1), 61-8, 2006.

SPECT

Projection/list mode data

Image reconstruction

Attenuation correction

Image Reconstruction

Bioluminescence tomography

Surface topography generation

Place projection data on boundary

Image reconstruction

Slavine et al. “Iterative reconstruction method for light emitting sources based on the diffusion equation.” Med. Phys. 33(1), 61-8, 2006.

Attenuation model

SPECT

Projection/list mode data

Image reconstruction

Attenuation correction

Image Reconstruction

Bioluminescence tomography

Surface topography generation

Place projection data on boundary

Image reconstruction

Slavine et al. “Iterative reconstruction method for light emitting sources based on the diffusion equation.” Med. Phys. 33(1), 61-8, 2006.

Scatter model

SPECT

Projection/list mode data

Image reconstruction

Attenuation correction

Surface Topography

- photogrammetry/stereography – parallax.
- fringe projection profilometry – using grid of parallel lines and phase unwrapping/Fourier transform, phase map produced and converted to depth map (Xenogen – Structured Light Analysis)
- EM reconstruction of the surface of last scattering (Slavine et al. “Iterative reconstruction method for light emitting sources based on the diffusion equation.” Med. Phys. 33(1), 61-8, 2006).

Binary volume mask

- Convert surface topography to 3D array masking animal volume.
- May required morphometric ‘cleaning’ in sparsely covered regions of surface.

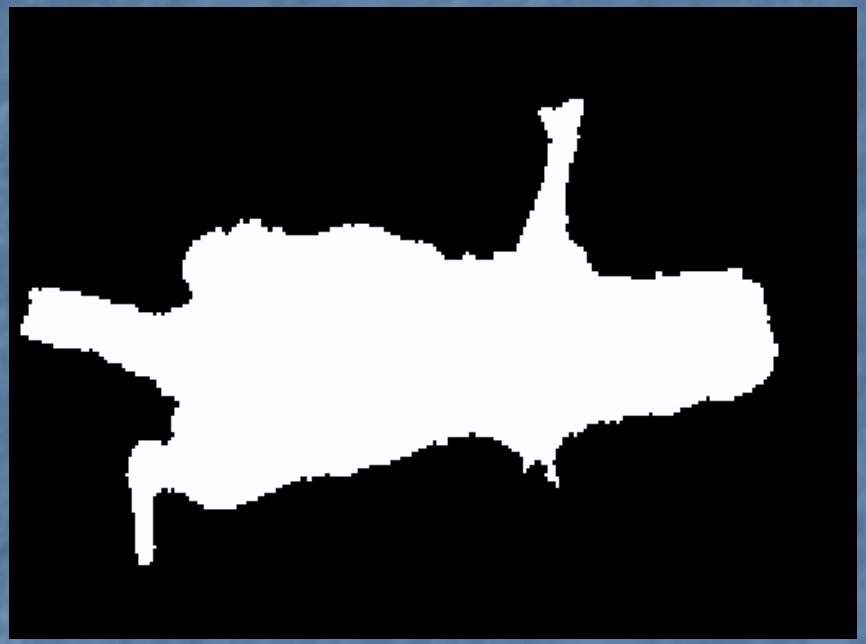

Forward modeling for scatter correction

- Assume homogeneous media.
- Produce PSF/LSF for deconvolution of projection data.
- Or generate LUT for scatter correction during iterative recontruction.
- Generally slow... hours-day for billions of events.
- But perhaps only 10 million events needed (Beekman et al.)
- Prototype on Rocks 4.0 8 Opteron cluster and migrate to resources at Texas Advanced Computing Center (www.tacc.utexas.edu)

MCNPX

- Monte Carlo N-Particle eXtended v2.5f
- supports both MPI and PVM.
- notoriously slow for voxelized phantoms/models (Du et al. IEEE Trans Nuc Sci. 49(3),2002).
- 1^{st} and 2^{nd} order surfaces defined with positive/negative senses.
- $O(n^3)$ surface checks for localization.
- Most computational complexity goes into tracking which cell photon is in.
- Simulate only animal (not detectors) and generate data on unit cylinder. Will use pre-calculated angular response functions for collimation.

```
MODE P SDEF ERG=D1 POS=0 0 0.4 DIR=1 VEC=1 0 0
c define I-125 source with all emission > 3 keV
SI1 L 0.0041325 0.027202 0.0274726 0.03110115 0.03176213 0.0354919
SP1 D 0.092512 0.246492 0.459456 0.131628 0.028499 0.041413
```

Reducing geometric complexity

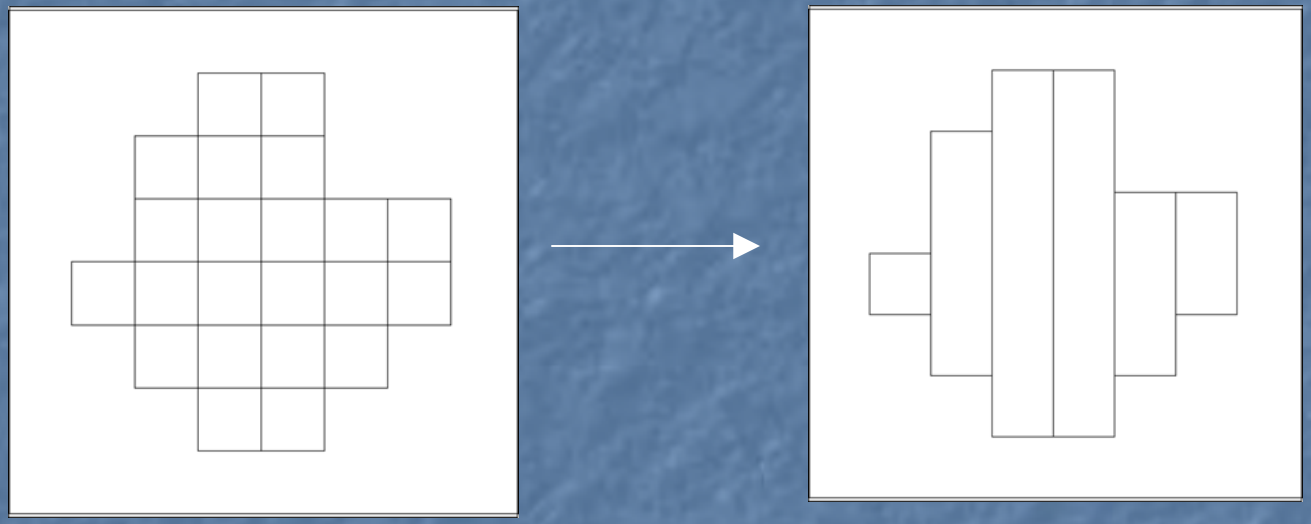

- BVMtoINP Perl script converts binary volume mask to geometry input for MCNPX.
- Naïve approach merges rows of homogeneous voxels in each transaxial slice.
- Reduces $O(n^3)$ to $O(n^2)$.

Validation

- Compare 1 surface cylinder to voxelized cylinder of water with planar reduction (r=h=15 mm, n = 60).

	1 surface	n^2 surfaces
unscattered	76.50%	76.60%
single scatter	19.00%	18.90%
double scatter	3.70%	3.70%
higher order scatter	0.68%	0.65%
time (seconds)	26	2060

Further geometric reduction

- Need to partition a hole-free rectilinear polygon using rectangles.
- Ohtsuki algorithm for finding a minimal non-overlapping cover (MNC) - T. Ohtsuki. “Minimum Dissection of Rectilinear Regions.” Proceeding of the 1982 IEEE Symposium on Circuits and Systems, pp.1210-13.
- $O(n^{5/2})$ algorithm for preconditioning geometry.
- Better 2D algorithms exist for polygons with minimal concavity.

Ohtsuki algorithm

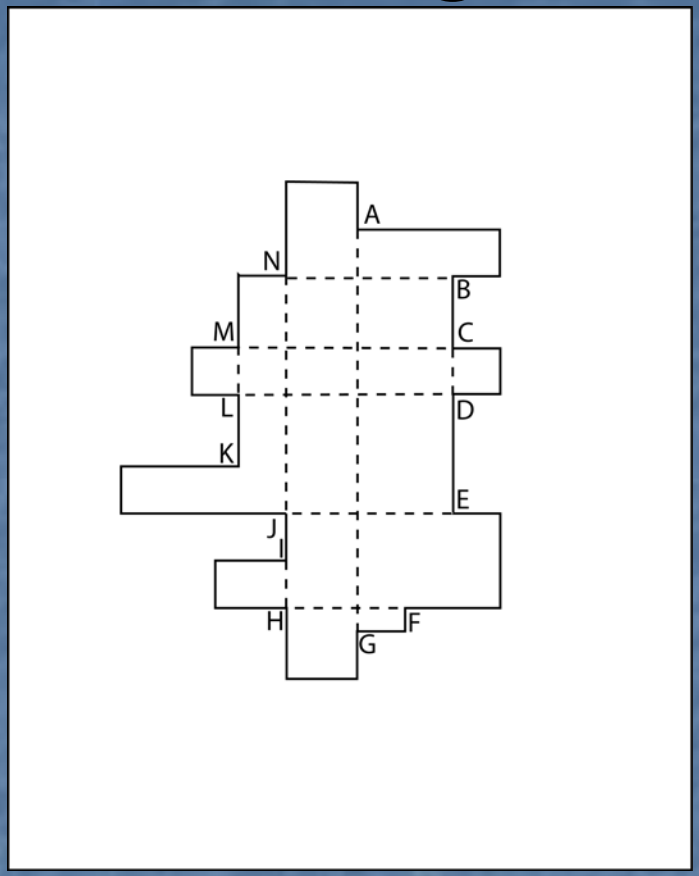

- Find all cohorizontal and covertical chords between convex vertices.

Ohtsuki algorithm

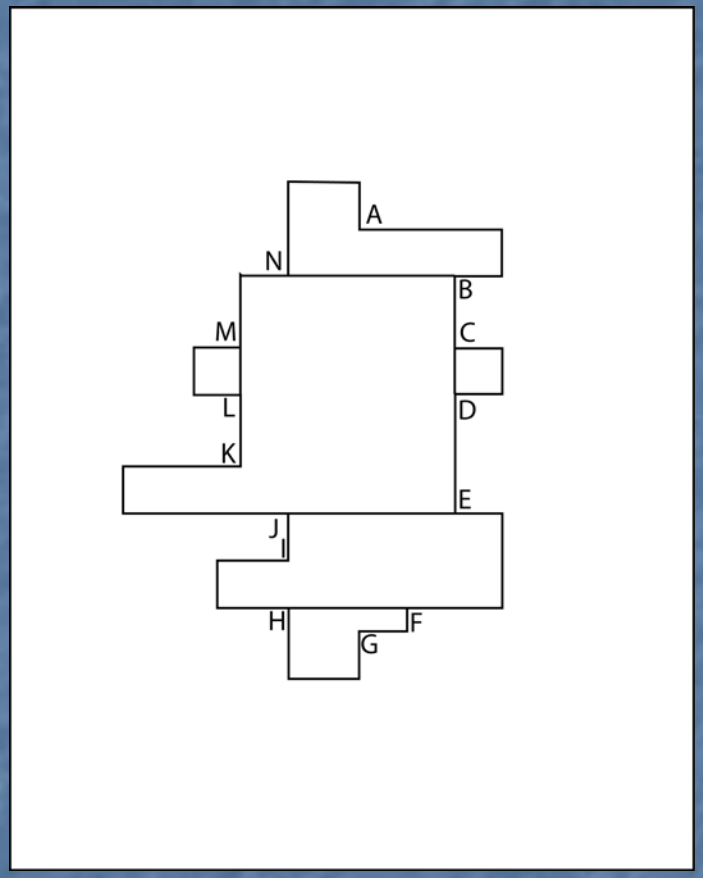

- Find largest independent set of chords (use algorithm for finding maximum independent vertex set for bipartite graph).

Ohtsuki algorithm

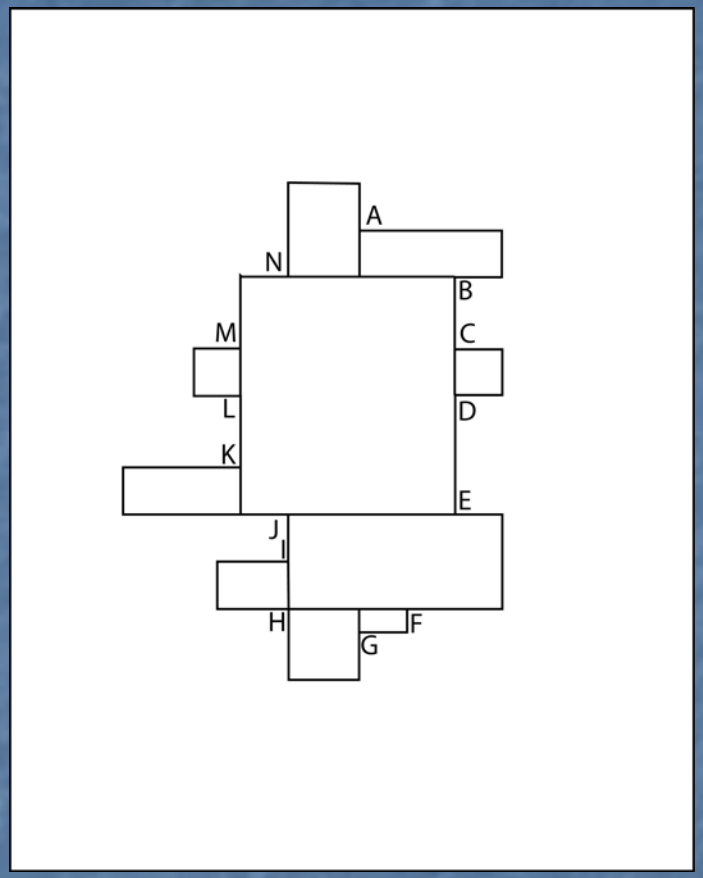

- For all unused convex vertices, draw maximum length vertical line to a chord.

Results

- Consider a binary volume mask with 20 slices x 2088 pixels.
- Merge naively on a planar basis to produce 20 x 70 MCNP geometric elements – 104 second runtime.
- Apply Oshtuki algorithm to further reduce to 20 x 10 MCNP geometric elements – 26 second runtime.

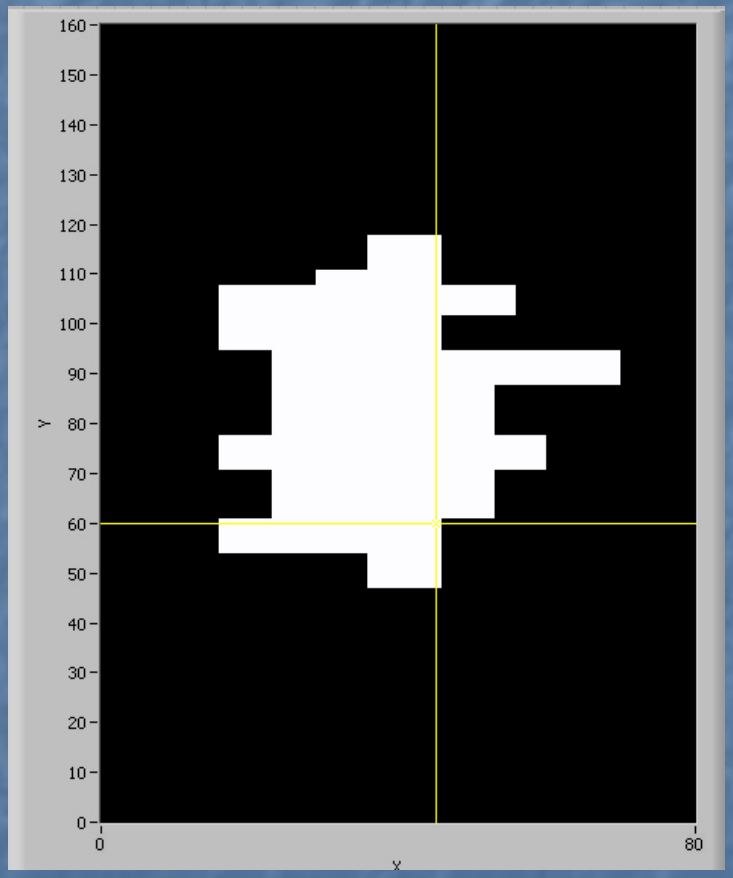

Future improvements

- 3D geometry reductions.
- Piercings of binary volume mask using hexahedrons.
- One large rectangular box for majority of animal body.
- Finer surface detail.
- Integrate with MCNP LATTICE cards for improved performance.

Extra stuff

- bipartite graph
- embedding SPECT MC in diffuse optical MC

Bipartite Graph of Chords

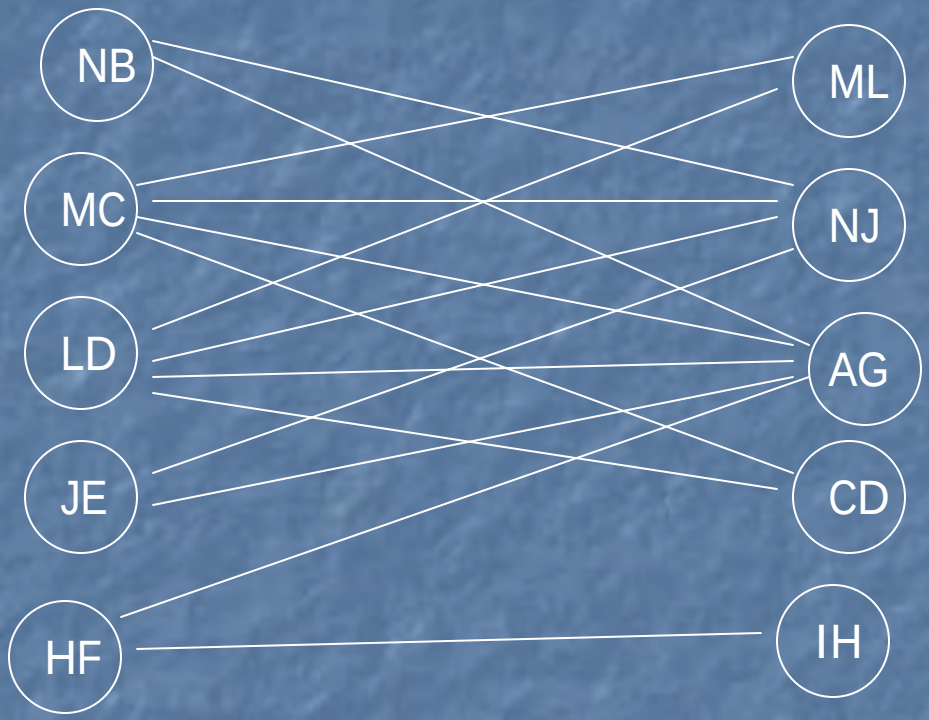

- H + V = MM + MIVS
- Hopcroft-Karp bipartite matching, Python Cookbook, David Eppstein, UC Irvine, 2002.

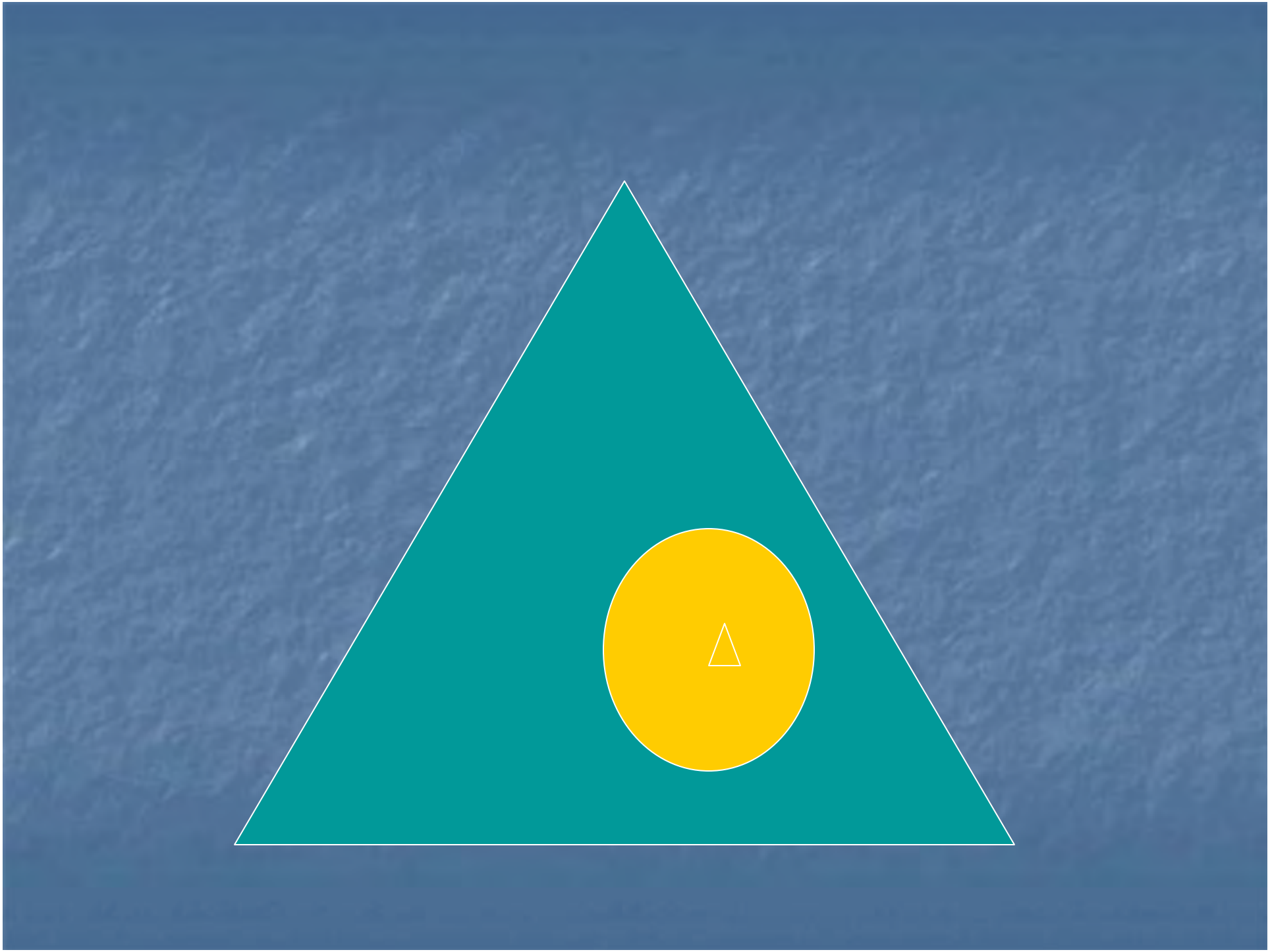

Construction, calibration and evaluation of a tissue phantom with reproducible optical properties for investigations in light emission tomography

Nikolai V Slavine, Todd C Soesbe, *Student Member, IEEE*, Edmond Richer, Matthew A Lewis, *Member, IEEE*, Peter P Antich, *Senior Member, IEEE*

Abstract— **We describe in details the materials and methods used to construct, calibrate and evaluate tissue phantoms and light sources; we describe the method for acquiring the data and present quantitative results for light intensity reconstruction using the reproducible phantom's optical properties as *a priori* information. We consider a tissue phantom imaging with optical properties which match those for typical mouse tissues, as a useful part of light diffusion studies in heterogeneous biological media in order to obtain important parameters for any reconstruction technique. Solid tissue phantoms are particularly useful for the study of light-tissue interaction and are still an active area of investigation.**

I. INTRODUCTION

Bioluminescence imaging (BLI) is used to observe non-invasively and in real time the presence or activation of specific biological process at the molecular level [1]-[4]. With a multicamera BLI device capable of tomographic studies [5]-[9], the 3D spatial distribution and temporal dynamics of luciferase expressing cells within the animal can be measured in great detail [10]. Since the scattering and absorption of light are dependent upon the amount of tissue between source and detector, knowledge of source depth would improve methods to determine localization and size estimation of cell populations [8], [11]. The goal of BLI volumetric tumor experiments is to perform quantitative cells studies where intensity is a function of number of light-emitting cells [7], [12]. Since the intensity of light emitted from luciferase cells depends on both the type of injection and the time from injection to imaging [7], it appears necessary to account for this variability, and a *BLI* tomography system with multiple cameras can account for this time course.

The main objective of phantom tests is to quantify the reconstruction capabilities of the tomographic device for sources at different tissue depths. We note that there are only a few recent publications [13]-[16] that use a mathematical heterogeneous phantom as a realistic media model for bioluminescence tomography. Improved techniques in diffuse luminescent tomography were provided by Xenogen Corp. [17]. The factors that affect BLI quantization are resolution, light absorption, scattering, and interaction at major interfaces. The reasonable reconstructed spatial resolution FWHM (*Full-Width at Half-Maximum*) which can be achieved for the deepest source depends on the approach of light transport used in the context of heterogeneous media. The solution uniqueness for BLI [18] can be strengthened by incorporation of *a priori* information [13], [14], [19] and by using an appropriate simplified model of light transport in turbid media: bioluminescence photon scattering predominates over absorption in mouse tissue; steady-state diffusion equation [13]; partial current boundary condition for a semi-infinite space [17]; an initial order approximation to the photon fluence [19]; the fluence rate data represented by a linear operator in terms of the internal source [14] or source function expressed by a linear combination of solid balls in known quantity and position and where each ball's total energy can be estimated [18]. With such a model the study of light source intensity and localization inside the phantom media [1], [18]-[22] and studies with open small animal organs [23] can help us assess and improve reconstruction algorithms for BLI. This significant problem has been identified in several publications [13], [14], [19], [24] and applies to all optical tomographic reconstruction techniques. Solid tissue phantoms are particularly useful for the study of light-tissue interaction and are still an active area of investigation [19], [21], [25]-[27].

II. PHANTOM CONSTRUCTION

We fabricated our phantoms and light sources following procedures from published articles [28]-[31], but here we would like to provide important missing details on its construction and especially a novel method for phantom calibration procedure. The phantom material was a mixture of distilled water, agarose (*Sigma A0169*) and 20% of Intralipid (*IL*). By changing the concentration of *IL* from 0.25% to 2.0% the value of the reduced scattering coefficient μ_s' can be varied from 2.5 cm^{-1} to 15 cm^{-1} without any significant change to the absorption coefficient μ_a (for evaluation of optical properties we used the method of Cubeddu et al [30]). These reduced scattering coefficients match those of typical mouse tissues [1]. The light is emitted

Manuscript received September, 7 2007. This work was supported in part by the NIH/National Cancer Inst. U24 CA126608-SAIRP [37] and the U.S. Department of Defense CDMRP BCRP Award Number W81XWH-04-1-0551. All Authors are with the Division of Advanced Radiological Sciences at the University of Texas Southwestern Medical Center at Dallas, 5323 Harry Hines Blvd, Dallas, TX, 75390, USA

(e-mail:nikolai.slavine@utsouthwestern.edu)

978-1-4244-1626-4/07/$25.00 ©2007 IEEE.

from the tapered end of the optical fiber 1 mm in size which was threaded through the needle (see Fig.1).

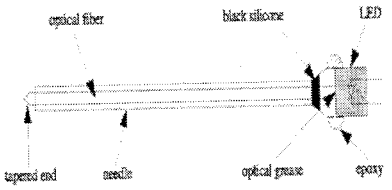

Figure 1. Schematic of the needle assembly. The optical fiber is threaded through the needle and held in place with black silicone. A high-intensity light emission diode is coupled to one end of the fiber using optical grease and epoxy. Light is emitted from the tapered end of the fiber which resides inside the phantom

The peak wavelength of the light source tuned at about 580 nm matches that of the firefly Luciferase [31] in vivo spectrum, which extends to 680 nm. The source is isotropic and reproducible within the phantom. Single and multiple light sources are possible. A single *CCD* camera was used to take multiple planar images of the rotated phantom. A sketch of the phantom is shown in Fig.2. The phantom had a circular aluminum base through which an 18 gauge hypodermic needle was inserted. The tip of the needle was ground flat so that it was perpendicular to the needle axis. There were five different radial positions for the needle ranging from the center (0.0 mm) to just below the surface (10.16 mm), with a step size of 2.54 mm. A 1.0 mm diameter optical fiber (*Bicron BCF-10*) was threaded through the needle, both ends of the fiber being highly polished. The fiber was held in place by a small amount of black silicone at the needle base. A high intensity light emitting diode was cut, polished, then optically coupled (*Dow Corning Q2-3067* optical grease) to the end of the fiber that extends out of the phantom.

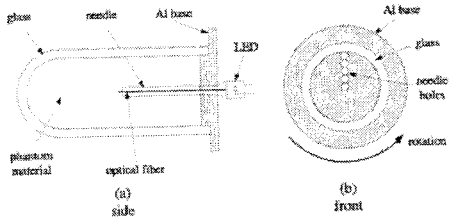

Figure2. The side view (a) shows the aluminum base, hypodermic needle with optical fiber and light emission diode, and glass enclosure. The front view (b) shows the five different radial positions for the needle, and the direction of rotation.

III. PHANTOM CALIBRATION AND EVALUATION

After we have built the phantom, we must provide a calibration procedure. For this purpose tomographic data were taken for phantom without material to find corrections (space shifting) for any geometrical positions of the sources and the light intensity was recorded. These geometrical corrections we used for 3D reconstruction of sources with unknown location in a turbid medium-filled phantom. The measured intensities were used to confirm estimates determined after balancing the internal and external intensities on the phantom boundary by using diffusion equations [19]. Our 3D image reconstruction technique for interior sources at phantom calibration tests is based on the widely used iterative algorithm - Maximum Likelihood Expectation Maximization method (ML) [32] which permits reconstruct location and intensity with an excellent resolution of any light sources emitted without phantom material (see TABLE 1 and Fig.3).

TABLE I
Reconstructed intensity, source positions and FWHM for X, Y and Z profiles for phantom calibration tests. All corrections included.

Actual (mm)	**Reconstructed**	FWHM			**Intensity** phot/sec
		X	Y	Z	
	Single source phantoms				
0.00	-0.08	0.89	0.91	0.90	1440×10^7
2.54	2.58	0.91	0.93	0.92	1440×10^7
5.08	5.03	0.86	0.89	0.88	1440×10^7
7.62	7.60	0.89	0.92	0.91	1440×10^7
10.16	10.01	0.91	0.93	0.92	1440×10^7
	Dual source phantoms				
0.00	0.08	1.01	1.03	1.02	6125×10^6
2.54	2.64	0.97	1.01	0.99	9602×10^6
7.62	7.70	0.96	1.04	0.98	8748×10^6
10.16	9.98	0.97	1.02	0.99	11930×10^6
0.00	0.07	1.05	1.09	1.06	7633×10^6
10.16	10.03	1.05	1.08	1.08	11060×10^6

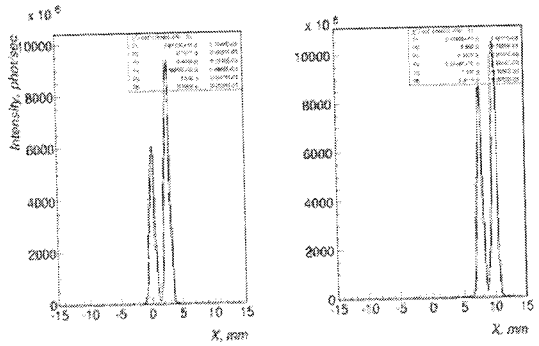

Figure 3. X profiles after of 3D ML reconstruction for dual source phantoms for separation 2.54 mm, Voxel size is 0.5 mm in this calibration test. Space correction included.

After the phantom was calibrated, the imaging procedure and reconstruction algorithms were verified using a light source ~ 1 mm in diameter with phantom media both using single and dual source configurations.

Our algorithm is based on 3D surface reconstruction, on an initial order approximation to the photon fluence and on an iterative deblurring method for the photon fluence to obtain a final result. A detail description of the algorithm for source reconstruction inside the tissue follows (see [19] and references therein):

1. In order to estimate the source location we backproject our phantom's experimental data into the volume discretized into $N_x \times N_y \times N_z$ voxels. In this step we obtain estimations for X, Y and Z coordinates of all light sources in the reconstructed volume. We calculate the intensity of reflection on boundary for each voxel j, and subtract its contribution from the transmitted part of intensity recorded by the detector. The diffusion equation is used to determine the balance intensities for internal sources N_s for the surface element in a single voxel.

2.For each voxel j we determine an initial order approximation for the photon fluence φ_j^0, which contains all diffuse light information:

$$\varphi_j^0 \cong \frac{1}{\sum_{i=1}^{I} x_{ij} p_i^t} \sum_{i=1}^{I} x_{ij} p_i^0 \sum_{s=1}^{s=N_s} S_o^{'} \exp(-\mu_{eff} r_{js}) / r_{js}$$

where $\mu_{eff} = (\mu_a / D)^{1/2}$. The initial photon fluence φ_j^0 depends upon x_{ij} the path length of line i through voxel j, intensities in *CCD*s from source in media p_i^t, intensity estimates p_i^0 and optical properties of the media, D is the diffusion coefficient and μ_a is the absorption coefficient.

3. After correcting all voxels we subsequently apply the *iterative Deblurring Expectation Maximization method* to obtain a final reconstruction result φ_j^{k+1} :

$$\varphi_j^{k+1} = \varphi_j^k \left(\frac{\varphi_j^0}{\varphi_j^k \otimes \rho} \right) \otimes \rho$$

where $\otimes$ denotes convolution procedure .Parameter ρ is the deblurring kernel (for example Gaussian function, but other forms will be used if needed), k - number of iterations.

After reconstruction the values of FWHM obtained from the Gaussian fit are taken as reconstructed source sizes and are in a good agreement with physical dimensions (see Table II).

TABLE II
Reconstructed source positions and FWHM for X, Y and Z profiles for Intralipid phantom tests.

Actual X (mm)	X (mm)	**Reconstructed** FWHM X	Y	Z
Single source phantom				
0.0	0.098	1.15	1.18	1.16
2.54	2.64	1.18	1.21	1.20
5.08	5.06	1.19	1.22	1.20
7.62	7.52	1.04	1.09	1.08
10.16	9.98	1.20	1.24	1.19
Dual source phantom				
0.0	-0.25	1.32	1.38	1.33
10.16	10.27	1.17	1.22	1.18

IV. CONCLUSION

The reconstruction of three-dimensionally distributed sources is the main goal of tomographic *BLI* studies and an important part of medical physics research [12]-[14], [34]. There are many difficulties in obtaining information about the irregular surfaces or optical properties of heterogeneous objects in the interior of an animal's body or phantom. In this case, BLI reconstruction could be strengthened by incorporation of *a priori* information on the animal anatomy and tissue properties [13], [19] and may shed light on this extremely difficult inverse problem [18], [33]. As a first step in this direction we recently tested a 3D reconstruction method [19] for light diffusion in tissue phantoms and heterogeneous mouse-shaped phantom. Reconstruction results in homogeneous media and a heterogeneous mouse-shaped phantom, and tumor size quantification studies all demonstrate the utility of this method with different surface topographies. This reconstruction method can be also useful for recently provided 3D tumor shape [35] and location [36] reconstruction from 2D bioluminescence images.

These tissue phantoms can be used to advance our goal of quantitative cells studies where detected light intensity is depends on the number of cells. We consider a tissue phantom imaging with optical properties, which match those for typical mouse tissues, as a useful part of light diffusion studies in heterogeneous biological media in order to get important parameters for any reconstruction technique [13]-[22], [24].

We will improve this phantom and add a few heterogeneities to continue light transport studies through turbid media to better understand real processes in small animal bioluminescence imaging.

REFERENCES

[1] B.W. Rice, M.D. Cable, M.B. Nelson, "In vivo imaging of light-emitting probes", J.Biomed. Opt. vol. **6**, pp. 432-440, 2001.

[2] S. Bhaumik, S.S.Gambir, "Optical imaging of Ranilla luciferase reporter gene expression in living mice", Proc. Nat. Acad. Sci, vol. **99**, pp. 377-382, 2002.

[3] T.F. Massound, S.S. Gambhir, "Molecular Imaging in living subjects: Seeing fundamental biological processes in a new light", Genes and Development vol. **17**, 545-580, 2003.

[4] Ge Wang, W.Cong, K.Durairaj, X.Qian, H.Shen, P.Sinn, E.Hoffman, G.McLennan, M.Henry, "*In vivo* mouse studies with bioluminescence tomography", Optic Express, vol. **14**(17), pp. 7801-7809, 2006.

[5] R. Blasberg, "In vivo molecular-genetic imaging: multi-modality nuclear and optical combinations", Nucl. Med.Biol. vol. **30**, pp. 879-888, 2003.

[6] G. Alexandrakis, F.R. Rannou, A. Chatziioannou, "Tomographic bioluminescence image by the use of a combined optical-PET (OPET) System: a computer simulation feasibility study", Phys. Med. Biol., vol. **50**, pp. 4225-4241, 2005.

[7] Z. Paroo, R.A. Bollinger, D.A. Braasch, E. Richer, D.R. Corey, P.P. Antich, R.P. Mason, "Validating Bioluminescence Imaging as a High-Throughput, Quantitative Modality for Assessing Tumor Burden", Molec. Imaging vol. **3**, pp. 1-8, 2004.

[8] E. Richer, N. Slavine, M. Lewis, E.Tsyganov, G.Gellert, Z. Dikmen, V. Bhagwandin, J.Shay, R.P. Mason, P.P. Antich, " Three Dimensional Light Emission Tomography using multiple rotating CCD Cameras", J. Molec. Imaging, vol. **3**(3), pp. 229, 2004.

[9] Z.G. Dikmen, G. Gellert, P. Dogan, R. Mason, P. Antich, E. Richer, W.E. Wright, J.W. Shay, "A New Diagnostic System in Cancer Research: Bioluminescent Imaging", Turk. J. Medical Sci. vol. **35**, pp. 65-70, 2005.

[10] V. Ntziachristos, J.Ripoll, L.Wang, R. Weissleder, "Looking and Listening to light: the evolution of whole-body photonic imaging", Nat. Biotech. vol. **23**, pp. 313-320, 2005.

[11] S.H. Thorne, C.H. Contag, "Using In Vivo Bioluminescence Imaging to Shed Light on Cancer Biology", Proc. IEEE, vol. **93**, pp. 750-762, 2005.

[12] J.M. Park, S.S. Gambhir, "Multimodality Radionuclide, Fluorescence, and Bioluminescence Small Animal Imaging", Proc. IEEE, vol. **93**, pp. 771-783, 2005.

[13] Ge Wang ,W.Cong, Yi Lu, W.Han, D.Kumar, X.Qian, H.Shen, M.Jiang, T.Zhou, J.Cheng, J.Tian, Y.Lv, H.Li, J.Luo, "Recent Development in Bioluminescence Tomography", 3d IEEE Inter. Symp. on Biomedical Imaging: from Macro to Nano, Arlington, pp. 678-681, 2006.

[14] H. Dehghani, S. Davis, et al "Spectrally resolved bioluminescence optical tomography" Optics Letters vol. **31**(3), pp. 365-367, 2006.

[15] W.Cong, Ge Wang, D.Kumar, Y.Lu, M. Liang, L.Wang, E.Hoffman, G. McLennan, P. McCray, J. Zabner, A.Cong, "Practical reconstruction method for bioluminescence topography", Optic Express, vol. **13**(18), pp. 6756-6771, 2005.

[16] A.X.Cong, Ge Wang, "Multispectral Bioluminescence Topography: Methodology and Simulation", Intern. J. Biomedical Imaging, pp. 1-7, 2006.

[17] C. Kuo, Heng Xu, B. Rice, "Improved Techniques in Diffuse Luminescent Tomography on Whole Animal Meshes", Soc. Molec. Imaging, 5th Ann. Meetig, Hawaii, USA, 2006.

[18] Ge Wang, Yi Li, Ming Jiang, "Uniqueness theorems in bioluminescence tomography", Medical Physics, vol. **31**, pp. 2289-2299, 2004.

[19] N.V. Slavine, M.L. Lewis, E.Richer, P.P. Antich , "Iterative reconstruction method for light emitting sources based on diffusion equation", Medical Physics, vol. **33**(1), pp. 61-68, 2006.

[20] S.R. Arridge, M. Dehghani, M. Schweiger, E. Okada, "The finite element method for the propagation of light in scattering media: A direct method for domains with nonscatering regions", Medical Physics, vol. **27**, pp. 252-264, 2000.

[21] Xuejun Gu, Qizhi Zhang, L. Larcom, H. Jiang, "Three-Dimensional bioluminescence tomography with model-based reconstruction", Optics Express vol. **12**, pp. 3996-4000, 2004.

[22] W.Cong, K.Durairaj, L.V.Wang, Ge Wang, "A Born-type approximation method for bioluminescence tomography", Medical Physics, vol. **33(3),** pp. 679-686, 2006.

[23] B. Bhagwandin, A. Harper, A.W.Beck, R.P.Mason , E.Richer, P.P.Antich , E.Tsyganov, M.A.Lewis, N.V.Slavine, J.B.Fleming, W.E.Wright, R.A.Brekken, J.W.Shay, "Detection of Pancreatic Cancer *In Vivo* using Light Emission Tomography", proc. 13th Conf. of the Intern. Society of Differentiation, Honolulu, 2004.

[24] T. Dierkes, D.Grosenick, K.T.Moesta, M.Moller, P.M. Schlag, H.Rinneberg, S. Arridge, "Reconstruction of optical properties of phantom and breast lesion in vivo from paraxial scanning data", Phys. Med. Biol., vol. **50**, pp. 2519-2542, 2005.

[25] A.H. Hielscher, A.D. Klose, J. Beuthan, "Evolution strategies for optical tomographic characterization of homogeneous media", Optic Express, vol. **7**(13),pp. 507-518, 2000.

[26] S. Li, W.Driessen, S.Sullivan, H.Jiang,"Bioluminescence tomography based on phantoms with different concentrations of bioluminescent cancer cells", J.Opt.A: Pure Appl.Opt, vol. **8,** pp. 743-746, 2006.

[27] D.C. Comsa,T.J. Farrell, M.S. Patterson, " Quantification of bioluminescence images of point source objects using diffusion theory models", Phys.Med. Biol.,vol. **51**, pp. 3733-3746, 2006.

[28] Firbank, D.T. Delpy, "An improved design for a stable and reproducible phantom material for use in near-infrared spectroscopy and imaging", Phys.Med.Biol. vol. **40**, pp. 955-961,1995.

[29] M U. Sukowski, F. Schubert, D. Grosenick, H. Rinneberg, "Preparation of solid phantoms with defined scattering and absorption properties for optical tomography", Phys.Med. Biol. vol. **41,** pp. 1821-1844, 1996.

[30] R. Cubeddu, A. Pifferi, P. Taroni, A. Torricelli, G. Valentini, "A solid tissue phantom for photon migration studies", Phys. Med. Biol., vol. **42**, pp. 1971-1979, 1997.

[31] Robert A.Larossa, "Bioluminescence Methods and Protocols (Methods in Molecular Biology)", Humana Press Inc, 1998.

[32] L.A. Shepp, V. Vardi, "Maximum Likelihood Reconstruction for emission tomography", IEEE, Trans. Med. Imaging vol. **1**, pp. 113-122, 1982.

[33] W.Han, W. Cong, Ge Wang, "Mathematical theory and numerical analysis of bioluminescence tomography", Inverse Problems, vol. **22**, pp. 1659-1675, 2006.

[34] Ge Wang, Haiou Shen, Wenxiang Cong, "Temperature-modulated bioluminescence tomography", Optic Express, vol. **14**(17), pp. 7852-7871, 2006.

[35] J.Huang, X.Huang, et. al. "3D tumor shape reconstruction from 2D bioluminescence images", IEEE Inter. Sym. Biomed. Imaging, Arlington, Virginia, USA, 2006.

[36] X.Huang, D.N. Metaxas, et. al., "Recovering 3D tumor location from 2D bioluminescence images and registration with CT images", Multimodal Biomedical Imaging, SPIE 2006.

[37] Mason R., UT Southwestern In Vivo Cancer Cellular and Imaging Program, http://cip.swmed.edu/SW-SAIRP Radiology UT Southwestern Medical Center at Dallas, 2007.